University of East Anglia

Biomechanical and physiological investigations in the IBMPFD animal model

Doctor of Philosophy
Thesis, May 2016

Louise Cully

Supervisors:
Dr Giles Watts
Professor Ulrike Mayer
Dr Penny Powell

Norwich Medical School, Health Policy
and Practice, University of East Anglia

Table of contents

Abstract

Inclusion body myopathy associated with Paget's disease of bone and frontotemporal dementia (IBMPFD; OMIM 167320) is an autosomal dominant inherited multisystem disorder caused by mutations in the *valosin-containing protein* (VCP) gene. Knock-in mice expressing the common human p.R155H VCP mutation develop a progressive myopathy with ubiquitin-positive inclusion bodies, accumulation of abnormally shaped mitochondria in skeletal muscle and focal bone degradation reminiscent of Paget's disease of bone. To further assess the physiological effects of this mutation in muscle, we compared the *in vitro* contractile properties of the *extensor digitorum longus* (EDL) (fast-twitch muscle) and soleus (slow-twitch muscle) from mice heterozygous for the p.R155H mutation in VCP and wild-type mice. Our results showed that fast-twitch muscle fibres isolated from $VCP^{R155H/+}$ mutant mice ~12-15 months old not only fatigued faster and to a greater extent, but also recovered significantly slower and to a lesser degree than those of age-matched wild-type mice. Thereafter, the muscles seem to recover and by the time the mice were 27 months old, there was no difference in the fatigue resistance of mutant and wild type mice. These results suggest that VCP may be necessary for maintenance of glycolytic capacity in mouse fast-twitch muscle fibres at 12-15 months only. Investigation of oxidative capacity in 12 and 14 month old $VCP^{R155H/+}$ mice revealed significantly lower mitochondrial enzyme activity (citrate synthase) in $VCP^{R155H/+}$ mice at 14 months; concomitant with the reduction in fast-twitch fibre fatigue tolerance. Primary fibroblast cells isolated from our $VCP^{R155H/+}$ mouse model showed reduced ability of mitochondrial networks to fragment when exposed to oxidative stress, indicating that intact VCP is required for the successful maintenance of mitochondrial network dynamics and quality control.

Figure List

Chapter 4

Supplementary data

Table List

Abbreviations

ALP	Alkaline phosphatase
ALS	Amytrophic lateral sclerosis
ATP	Adenosine triphosphate
CCCP	Carbonyl cyanide m-chlorophenylhydrazone
CK	Creatine phosphokinase
cM	centiMorgan
CrP	Creatine phosphate
DMEM	Dulbecco's Modified Eagles Medium
DPD	Deoxypyridinoline
EDL	*Extensor digitorum longus*
ERAD	Endoplasmic reticulum-associated degradation
FBS	Foetal bovine serum
FTD	Frontotemporal dementia
FTLD-U	Frontotemporal lobar degeneration with ubiquitinated inclusions
GFP	Green Fluorescent Protein
IBMPFD	Inclusion body myopathy associated with Paget's disease of bone and frontotemporal dementia
IMM	Inner mitochondrial membrane
kDa	kiloDalton
LC3	Microtubule-associated protein (MAP) Light Chain 3
LGMD	Limb girdle muscular dystrophy
Mcl1	Myeloid cell leukemia 1
Mfn2	Mitofusin 2
MHC	Myosin heavy chain
Nbr1	Neighbour of Brca1
OMM	Outer mitochondrial membrane
PBS	Phosphate buffered saline
PDB	Paget's Disease of Bone

PYD	Pyridinoline
TDP-43	TAR DNA –binding protein 43
UBX	Ubiquitin regulatory X domain
UPS	Ubiquitin-proteasome system
VCP	Valosin containing protein

Acknowledgements

Introduction

1.1 Inclusion body myopathy associated with Paget's disease of bone and frontotemporal dementia

Inclusion body myopathy (IBM) associated with Paget's disease of bone (PDB) and frontotemporal dementia (FTD), hereafter referred to as IBMPFD, is an autosomal-dominantly inherited multi-system disorder (OMIM 167320) that results in premature death in patients. The disease is characterised by three pathological phenotypes of varying penetrance – progressive adult-onset proximal and distal myopathy; early-onset PDB and premature neurodegenerative FTD.

Despite its characterisation as a multi-system disorder, the phenotype is variable in how it manifests (both within affected families and between families), where the muscle weakness or myopathy is the most common symptom seen in 90% of affected individuals (Kimonis *et al.*, 2008). Disabling weakness is observed at approximately 45 years of age in 90% of patients, and 47% of patients develop osteolytic lesions congruent with PDB at a similar age. 37% of patients present with premature FTD at a mean onset of 54 years of age, manifested by prominent behavioural and language dysfunction (Weihl *et al.*, 2009). Figure 1.1 summarises the relative pathologic penetrance of each symptom of IBMPFD.
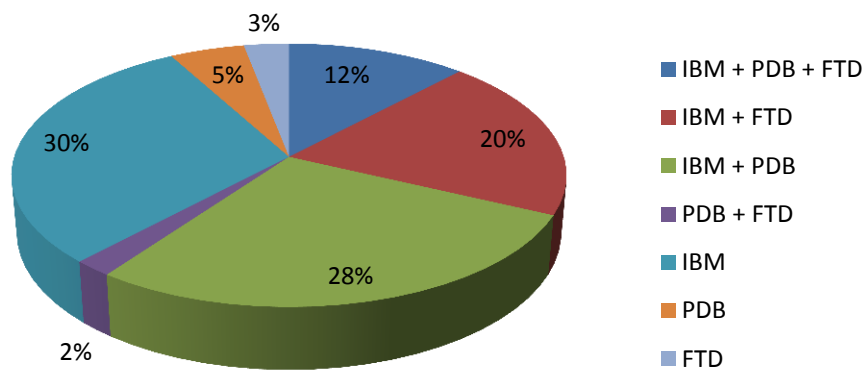
Figure 1.1 Varying symptomatic presentation in affected individuals. IBM: inclusion body myopathy; PDB: Paget's disease of bone; FTD: frontotemporal dementia (Data adapted from Pagon *et al.*, 2011)

The familial concurrence of neuromuscular disorder and Paget's disease of bone was originally observed in the mid-20th century, when Caughey (1957) described three brothers suffering from *"dystrophia myotonica"*, two of whom also suffered from Paget's disease. The diagnoses were based on the presentation of typical physiological features of *dystrophia myotonica*; neck and limb muscle hypertrophy lacking a proportional increase in muscle strength, mechanical myotonia of the tongue, general muscular stiffness and an inability to relax ones grip. In the two individuals suffering from Paget's disease, histological analysis revealed the disorganised mosaic pattern of the trabecular bone typical of the disease (Caughey, 1957).

Patients were diagnosed with IBMPFD if they presented with two or more of the clinical symptoms; however this classification preceded the discovery of the causal genetic mutation. In patients, the diagnosis of IBM is based on skeletal muscle histology, serum creatine phosphokinase (CK) concentration and electromyogram. Paget's disease of bone diagnosis is based on serum alkaline phosphatase (ALP) concentration, pyridinoline (PYD) and deoxypyridinoline (DPD) concentration in the urine, and radiographic or radionuclide scintigraphic scanning of the skeleton. The diagnosis of frontotemporal dementia is based on extensive neuropsychological assessments.

Each of the three pathophysiological symptoms may present in isolation, however the concurrence of both a limb-girdle muscular dystrophic (LGMD) and Pagetic phenotype was described by Kimonis and colleagues to be a genetically distinct disorder in 2000, with the researchers finding both symptoms present in eight out of eleven family members (Kimonis *et al.*, 2000). Bone X-rays revealed coarse trabeculation, sclerotic or hardened areas and thickening of the cortical regions of the pelvis, spine, skull and shoulder. Myopathic degeneration presents as adult-onset distal and proximal muscle weakness, with the hip and shoulder girdle muscle groups being initially involved. Winging of the scapula may be observed in some cases (Dec *et al.*, 2014). IBMPFD patients display an abnormal, waddling gait and are unable to raise the arms due to the effects of the disease on the hip and shoulder girdle muscles. Clinically, normal neural conduction, myopathic electromyogram and a generalized reduction in tendon reflexes is noted (Kimonis *et al.*, 2008). The disease progresses to "wheelchair confinement, quadriparesis, bedfastness, respiratory failure, cardiac failure and death in the 40s-60s" (Kimonis *et al.*, 2000). Chronic respiratory failure due to muscle weakness is the primary cause of death in IBMPFD patients, as well as in other myopathic conditions (Selva-O'Callaghan *et al.*, 2000).

Variable pathological features are seen in skeletal muscle biopsies of IBMPFD patients. Light microscopy reveals nonspecific changes in muscle biopsies; such as fibre size variability, predominance of type I fibres, and both fibre atrophy and hypertrophy. Fibres may contain single or numerous vacuoles. Rimmed vacuoles and VCP- and ubiquitin-positive inclusion bodies are seen in muscle fibres, which are characteristic of IBM. As the disease progresses, extensive degeneration of the muscle occurs, with associated fatty replacement of muscle tissue in severe cases (Hübbers *et al.*, 2007).

Paget's disease of bone is a chronic focal bone disorder which presents in approximately 45% of IBMPFD patients. The disease is suspected in individuals with bony tenderness, spine or hip pain, pathologic fractures and long- or cranial-bone deformity. Hearing loss may also occur as a result of compression of the vestibulocochlear nerve caused by calvarial bone overgrowth. Serum ALP concentration is elevated (Pagon *et al.*, 2011). The primary pathology manifests as increased resorption and deposition of highly disorganised and poor quality bone, which increases susceptibility to fracture. The imbalanced bone turnover rate is due to the increased bone resorbing capacity of osteoclasts in localised areas. Histological investigations reveal abnormally large, multinucleated osteoclasts with nuclear inclusions (Kimonis *et al.*, 2008; Nalbandian *et al.*, 2011). The mean age of onset of PDB in IBMPFD patients is 45 years.

The early symptoms of FTD include dyscalculia, dysnomia, paraphasic errors and comprehension deficits, with relative preservation of memory. Later stages are characterised by loss of speech, alexia, agraphia and deficient auditory comprehension (Nalbandian *et al.*, 2011). The preservation of memory serves to discriminate between FTD and Alzheimer's disease (Kovach *et al.*, 2001; Kimonis *et al.*, 2008; Nalbandian *et al.*, 2011; Pagon *et al.*, 2011). In addition, FTD patients display cerebral atrophy in the frontal and anterior temporal lobes, rather than the posterior temporal, hippocampal and parietal atrophy typical of Alzheimer's disease (Forman *et al.*, 2006; Kimonis *et al.*, 2008). Histologically, patients with IBMPFD-associated FTD display a novel pattern of ubiquitin pathology which is distinct from other variants of frontotemporal lobar degeneration with ubiquitin-positive inclusions (FTLD-U). Specifically, abundant intranuclear ubiquitin-positive inclusions, and dystrophic neurites are seen, primarily in the neocortex (Forman *et al.*, 2006).

A genome-wide screen of four unrelated IBMPFD families in the U.S revealed linkage to chromosome 9, and IBMPFD was found to localise to a 1.08-6.46 cM critical

interval on chromosome 9p13.3-12 (Kovach *et al.*, 2008). Further investigations using a candidate-gene approach uncovered six heterozygous missense mutations in the *valosin containing protein*, or *VCP* gene in 13 families with IBMPFD linked to chromosome 9, thus identifying an underlying genetic cause of IBMPFD (Watts *et al.*, 2004). To date, over 21 mutations in the VCP gene have been identified (Meyer and Weihl, 2014). These mutations are listed in Table 1.1. Pathogenic variants in the *VCP* gene have been identified in the majority of families with IBMPFD that link to chromosome 9p, yet several families have been identified that meet the diagnostic criteria for IBMPFD who do not harbour an identifiable pathological variant of *VCP* and have not shown linkage to chromosome 9.21.2, suggestive of genetic heterogeneity in IBMPFD (Waggoner *et al.*, 2002). Since the identification of the VCP mutation common to the majority of families with IBMPFD, studies have indicated that up to 10% of VCP-confirmed IBMPFD patients had previously been diagnosed with amyotrophic lateral sclerosis (ALS; Johnson *et al.*, 2010, Kimonis *et al.*, 2008), a neurodegenerative disease which manifests as upper and lower motor neuron dysfunction and leads to rapidly progressive paralysis and respiratory failure. Ubiquitin-positive inclusions and pathological TAR DNA-binding protein (TDP-43) aggregates are seen in the motor neurons, similar to those seen in the skeletal muscle and brain tissue of IBMPFD patients (Weihl *et al.*, 2008). Studies have broadened the spectrum of the IBMPFD phenotype to include motor neuron degeneration, and it is postulated that mutations in VCP may account for 1-2% of familial ALS (Johnson *et al.*, 2010).

Since the discovery of VCP mutations in IBMPFD patients, much research has been conducted to elucidate the molecular pathways involved in the progression of the disease. Unfortunately, at present, there are no known cures or treatments for the disorder (Chan *et al.*, 2012).

Table 1.1 *VCP mutations identified in patients with IBMPFD.* Mutations have been predominantly identified within the CDC48 N-terminal domain, the N-D1 Linker region (L1) and D1 ATPase domain (outside of the catalytic domain).

	Amino acid	Base change (ORF)	Exon	Domain	No. of families
1	I27V	79A>G	2	N terminus	1
2	R93C	277C>T	3	N terminus	4
3	R95G	283C>G	3	N terminus	2
4	R95C	283C>T	3	N terminus	1
5	P137L	410C>T	4	N terminus	1
6	R155C	463C>T	5	N terminus	5
7	R155H	464G>A	5	N terminus	8
8	R155P	464G>C	5	N terminus	1
9	R155S	463C>A	5	N terminus	1
10	R155L	N/A	5	N terminus	2
11	G157R	469G>C	5	N terminus	1
12	G156S	466G>A	5	N terminus	1
13	R159H	476G>A	5	N terminus	2
14	R159C	476G>A	5	N terminus	2
15	R191Q	572G>A	5	Linker 1	1
16	L198W	593T>G	6	Linker 1	2
17	I206F	828A>T	6	Linker 1	1
18	A232E	695C>A	6	L1-D1 Junction	1
19	T262A	784A>G	7	AAA D1	1
20	N387H	1159A>C	10	AAA D1	1
21	A439S	1351G>T	11	Linker 2	1

1.2 VCP structure

Valosin-containing protein, or VCP (p97 in mice, TER94 in *Drosophila melanogaster* and CDC48 in *Saccharomyces cerevisiae*) is a 97-kDa, highly conserved member of the type II AAA+ (ATPase associated with diverse cellular activities) ATPase family (Ju and Weihl, 2010). Proteins in the AAA+ ATPase superfamily typically assume hexameric conformation in the cytosol and harness the energy from ATP hydrolysis to perform macromolecular remodelling. VCP is found in all cells in the body, comprising 1% of the total cellular protein in yeast (Yamanaka *et al.*, 2011). The protein was first isolated from pig intestine in 1987 (Koller and Brownstein, 1987).

In a similar manner to other AAA+ protein family members, VCP operates as an enzymatic motor, using the energy from ATP hydrolysis to perform mechanical work in the cell, by binding co-factors and substrates and remodelling its confirmation to unfold or extract target substrates. Each VCP monomer consists of an N-terminal domain, two highly conserved central ATPase domains, D1 and D2, and a C-terminal region. The N-domain and D1 domain are joined by a flexible linker region, L1, while the D1 and D2 domains are connected by a second linker region, L2 (Wang *et al.*, 2003). The ATPase domains comprise Walker A and B domains, which serve to bind and hydrolyse ATP. The globular N-terminal domain, shown to be the least conserved region in the AAA+ family of proteins, is believed to be the determining factor in target-binding specificity, and mediates the binding of both adaptor proteins and ubiquitinated protein substrates (Wang *et al.*, 2004).

The distinct cellular functions of VCP are tightly regulated by a diverse number of cofactors. Two classes of cofactors can be distinguished - substrate-recruiting cofactors serve as adaptor proteins for substrates, and dictate their binding to VCP. In contrast, substrate-processing cofactors control the ubiquitylation state of substrates following their recruitment to VCP (Böhm *et al.*, 2011). For example, the N domain is known to facilitate the heterotrimeric complex formation of VCP with two adaptor proteins; ubiquitin fusion degradation 1 (Ufd1) and nuclear protein localization 4 (Npl4) (Pye *et al.*, 2007). It has been proposed that the VCP-Ufd1-Npl4 complex recognizes and extracts ubiquitinated substrates from either the endoplasmic reticulum (ER) lumen or ER membrane, and shuttles them to the cytoplasm for proteosomal degradation (Ye *et al.*, 2001; Ju and Weihl (Review) 2010). VCP is known to bind directly to substrates and cofactors which contain the ubiquitin regulatory X domain (UBX) (Dreveny *et al.*, 2004(ii)); however this domain is not a prerequisite for VCP interaction and binding. Table 1.2 comprises a non-exhaustive list of VCP-interacting proteins and their functions.

Table 1.2 *Classification of VCP interacting proteins based on structural or general functional characteristics*

Structural/functional criteria	VCP interacting protein	Function
Ubiquitin regulatory X (UBX) domain	Ubx2	Links VCP to ERAD
	p47	Essential for VCP-mediated post-mitotic Golgi reassembly
	VCIP135	Involved in VCP/p47-mediated membrane fusion
	Cui3p	Required for normal proteolysis and sporulation in yeast cells
	Cui2p	Required for normal proteolysis and sporulation in yeast cells
	Cui1p	Required for normal proteolysis and sporulation in yeast cells
DNA/RNA repair	WRN	VCP/WRN complex translocates from nucleolus upon DNA damage
	TB-RBP	Implicated in DNA recombination and repair events
	DUF	DNA unwinding factor, involved in DNA replication
	BRCA1	Participates in DNA repair, transcription and transcription-coupled DNA repair
Protein degradation	Ubiquitin	Small regulatory protein which targets substrates for degradation
	Ufd2	Substrate-processing cofactor of VCP involved in multi-ubiquitination
	Ufd3	Substrate-processing cofactor of VCP involved in multi-ubiquitination
	Proteasome	Degradation of ubiquitinated substrates
	Ufd1-Npl4	Retrotranslocation of poly-Ub peptides from the ER to the cytosol; spindle disassembly
Mitosis	Ase1	Spindle disassembly processes during mitosis-to-interphase transition
	Cdc5/Plx1	Spindle disassembly processes during mitosis-to-interphase transition
Membrane traffic	SVIP	Potential involvement in membrane trafficking
	SYT I, II	Membrane trafficking; SYT I required for Ca^{2+} triggering of exocytosis
	Clathrin	Receptor-mediated endocytosis and Golgi sorting
Others	EMeg32	Glucosamine-6-phosphate acetyltransferase; localises with VCP at Golgi
	Ex-polyQ	Expanded polyglutamine repeats
	Ataxin-3	VCP binds via ex-polyQ region of ataxin-3; proteasome-associated factor involved in Ub-protein degradation
	HDAC6	Nucleo-cytoplasmic shuttling, Ub-binding protein; deacetylates lysine residues

VCP exists as a homohexamer in the cell (Figure 1.2; Pye *et al.*, 2006; Mori-Konya *et al.*, 2009). The association of ATP with the D1 domain drives the formation of stable VCP homohexamers, whereas the D2 domain is largely responsible for ATP hydrolysis (Halawani *et al.*, 2008; Ju *et al.*, 2010). Cryo-electron microscopy and crystallography studies showed that the D1 and D2 ATPase domains of the VCP hexamer form two stacked rings surrounding a central channel or pore (DeLa Barre and Brunger, 2003; Pye *et al.*, 2006). It is unclear at present whether remodelling of substrates by VCP involves their complete or partial insertion through this central channel (Meyer and Weihl, 2014).
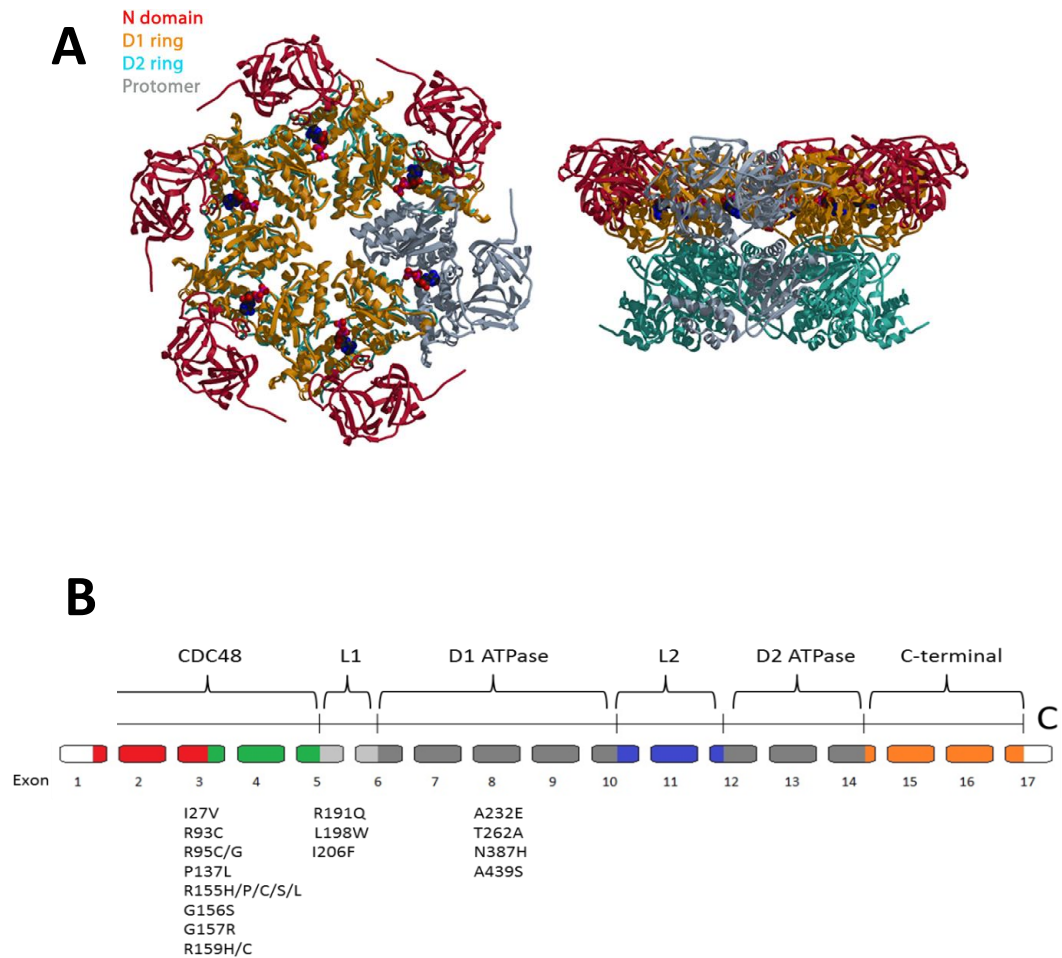
Figure 1.2. **Schematic representation of protein and domain structure of VCP.** (A) The single VCP protomer is coloured grey, the N domain is depicted in red, and the D1 and D2 ATPase domains are orange and cyan, respectively (From Pye *et al.*, 2006). The D1 and D2 ATPase domains of the VCP hexamer form two stacked rings surrounding a central channel or pore. (B) The CDC48 region, located in the N-terminal domain, has been identified as a mutation 'hotspot'. The L1 linker region, which connects the N domain to the D1 ATPase domain, is also susceptible to missense mutations. Mutations of the arginine residue at codon 155 comprise the most encountered mutation in IBMPFD patients.

The conformation of the N-domain and linker region with respect to the D1 and D2 regions relates directly to the ATPase activity of VCP (Niwa *et al.,* 2012). The N-terminal domain is positioned on the periphery of the D1 ring and the two are connected by a flexible 20 amino acid L1 linker region. This flexible linker region allows the hexamer to adopt one of two possible conformations, either coplanar or flexible (Figure 1.3). Hydrolysis of ATP by the D2 domain is thought to be the primary driving force by which the domain conformation of VCP is rearranged. This rearrangement results in the structural remodelling of specific target substrates. During the ATPase cycle, ATPase activity is supressed when the coplanar conformation is adopted between the N-domain and the D1 domain (Figure 1.3). However, when the N-domain is released from the D1 plane, D2-mediated ATP hydrolysis is possible and ATPase activity is increased. Studies have reported increased ATPase activity of disease-associated VCP mutants, with a 3-fold increase in ATP hydrolysis by VCP-R155P and VCP-A232E observed (Halawani *et al.*, 2009).
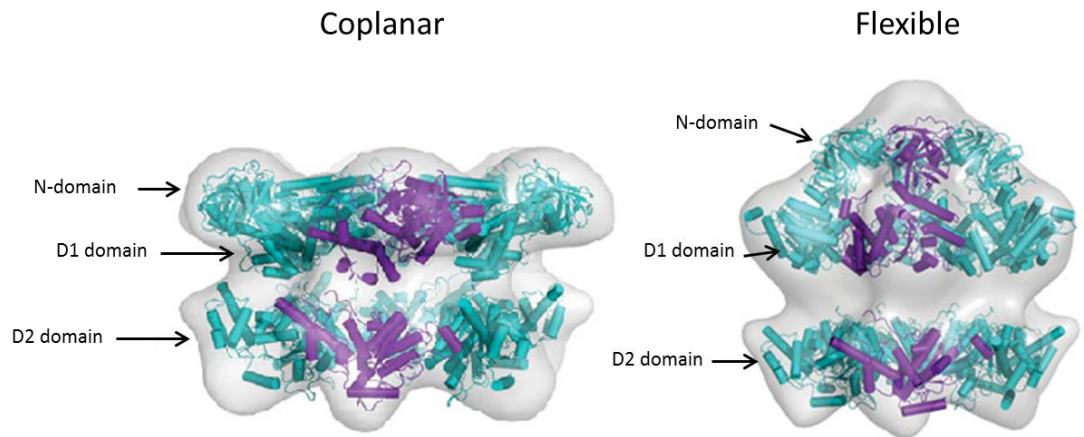
Figure 1.3. Structural model of VCP N-domain flexibility. During the ATPase cycle, VCP has the ability to adopt two conformations. When the N-domains are coplanar with the D1 ring, ATP hydrolysis is prevented. However, when the flexible conformation is adopted, ATP hydrolysis is facilitated by the compact ring formation of the D2 domains. The A232E mutation in the L1-D1 junction, is suggested to have a destabilizing effect on the N and D1-domain interaction due to steric hindrance, thus preventing the N and D1-domains assuming the coplanar conformation. Only two of the six monomers in the hexamer are shown for clarity (From Yeung *et al.*, 2014).

Of note, familial studies have shown that, while R155H is the most common mutation in IBMPFD patients, the base change mutation of alanine to glutamic acid (A232E, codon replacement of G<u>C</u>A with G<u>A</u>A) at amino acid position 232 in VCP results in a more severe pathological presentation, specifically a more aggressive myopathy and earlier onset of Paget's disease (Watts *et al.*, 2004). Interestingly, the A232E mutation was suggested to have a destabilizing effect on the N and D1-domain interaction due to steric hindrance, thus preventing the N and D1-domains assuming the coplanar conformation, which resulted in increased ATP hydrolysis by VCP (Niwa *et al.*, 2012).

1.3 VCP functions

Many cellular activities require the involvement of VCP, both as a chaperone protein and also in molecular complex formation. These activities include ER-associated degradation, nuclear envelope reformation, post-mitotic Golgi reassembly, cell cycle control and membrane fusion (Rabinovich *et al.*, 2002; Rabouille *et al.*, 1998; Alzayady *et al.*, 2005; Fröhlich *et al.*, 1991). These functions are at least partially regulated by the ubiquitin-proteasome system (UPS), in which VCP, acting as a molecular segregase, binds both poly-ubiquitinated proteins and ubiquitin-interacting proteins in order to facilitate their delivery to and subsequent degradation by the 26S proteasome (Pye *et al.*, 2007; Halawani *et al.*, 2009; Ju and Weihl, 2010).

In addition to the relatively well categorised role of VCP in the shuttling of cargo for proteasomal degradation, studies of IBMPFD patient tissue suggest the possible involvement of VCP in autophagy (Vesa *et al.*, 2009; Ju *et al.*, 2010; Tresse *et al.*, 2010). VCP interacts with misfolded aggregated proteins and structurally alters them in order to unfold or extract them, thus allowing them to be trafficked to either a proteasomal or autophagic fate (Bug and Meyer, 2010; Ju and Weihl, 2010). The term autophagy, from the Greek words 'phagy' (eat) and 'auto' (self), describes the evolutionarily conserved, homeostatic pathway by which cytoplasmic components are sequestered into a double-membrane vesicle, the autophagosome, which fuses with the lysosome to facilitate the degradation of its cargo by hydrolases (Figure 1.4). The process is generally activated during times of nutrient starvation, in order to catabolise non-essential macromolecules, however, it has also been associated with physiological and pathological pathways, such as development, cellular differentiation, stress, infection, cancer and neurodegenerative disorders (Mizushima and Levine, 2010; Codogno *et al.*, 2012). The resulting micronutrients and molecules are redirected to locations/processes where their requirement is immediate and vital for cellular survival.

In addition to this protective function, 'quality control' autophagy describes the basal autophagic pathways by which long-lived/misfolded proteins or dysfunctional organelles are shuttled to the autophagosome. These pathways may be further categorized based on the autophagic substrates involved, for example macroautophagy (degradation of cytoplasmic material, Figure 1.4), ribophagy (ribosomes) and mitophagy (mitochondria) (Bug *et al.*, 2012).
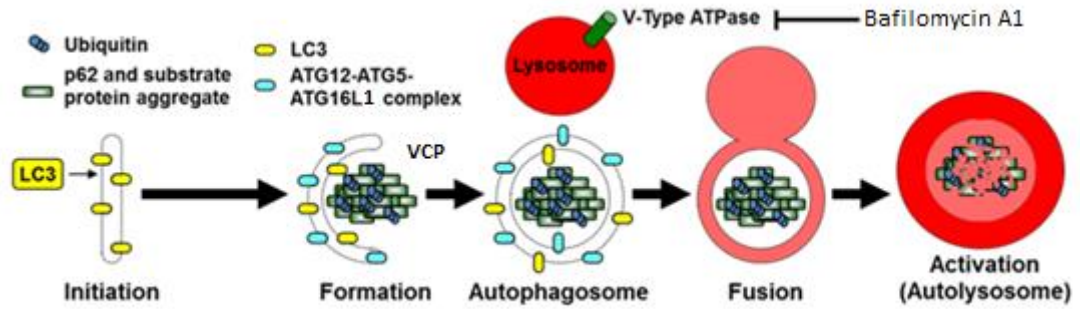
Figure 1.4 Schematic diagram of macroautophagic degradation. Under autophagy-inducing conditions, initiation of autophagy involves the formation of the phagophore (a membranous cistern-like structure) facilitated by the recruitment of an autophagy-related protein complex (ATG12-ATG5-ATG16L1) and LC3. Expansion of the phagophore allows engulfment of cytosolic components, including long-lived and dysfunctional organelles, protein aggregates and foreign organisms (viruses and bacteria). The autophagosome is formed when the expanding phagophore closes to form the typical double-membrane vesicular structure. The fusion of lysosomes with autophagosomes allows the entry of hydrolytic enzymes which then degrade the cargo, providing basic metabolites for use in the cell. VCP is believed to be involved in aggregation of autophagic protein cargo and autophagosome maturation, as the presence of VCP mutation results in the accumulation of immature autophagosomes.

Selective autophagic adaptor proteins, such as p62 and neighbour of Brca1 (Nbr1), recognize and form complexes with the ubiquitinated proteins/organelles that have been selected for degradation (Johansen and Lamark, 2011). Once the substrate-adaptor protein complex associates with LC3-II - the autophagosomal membrane-bound, lipidated form of the autophagic marker LC3 - the cargo is incorporated into the autophagic vesicle. The autophagosome then fuses with the lysosome and the engulfed content is degraded by lysosomal proteases and hydrolases (Weidberg *et al.*, 2011). LC3-II lipidation and accumulation in cells is generally used as a measure of autophagic flux, with an increase in the ratio of LC3-I to LC3-II conversion indicative of an upregulation of autophagy (Mizushima and Levine, 2010).

It was discovered that, under steady-state growth conditions, LC3-II and p62 levels were higher in mutant myoblasts obtained from IBMPFD patients than wild-type VCP controls, indicating a possible augmentation in the rate of autophagic turnover (Tresse *et al.*, 2010). Further analysis showed that the increase in intracellular autophagic marker proteins was accompanied by an accumulation of immature autophagosomes. Small interfering (si)RNA knock-down of VCP, or the expression of the dominant-negative ATPase deficient mutant, VCP^{E578Q}, showed similar increases in LC3-II, p62 and immature autophagosome accumulation (Ju *et al.*, 2009). However, these autophagosomes failed to localise with lysosomes. This finding suggested an impairment of autophagosome-lysosome fusion and subsequent autophagic substrate degradation in IBMPFD patients, an effect that has been replicated *in vitro* (Tresse *et al.*, 2010).

1.4 Mouse models of IBMPFD

In patients, the VCP mutation is expressed in an autosomal dominant manner, resulting in ubiquitous expression of mutated VCP protein. Heterozygous VCP$^{+/-}$ mice lacking one functional allele were found to be indistinguishable from wild-type littermates (Müller *et al.*, 2007). Histological analysis of muscle tissue from the VCP$^{+/-}$ mouse revealed irregularities in muscle fibre size and organization, increases in endomysial connective tissue and the presence of small, linear, basophilic 'rimmed cracks', resembling the pathology in IBMPFD patients. In order to examine the effects of mutated VCP-R155H expression in muscle tissue specifically, Weihl and colleagues (2007) generated a transgenic overexpression mouse model, which expressed the VCP-R155H allele under a skeletal muscle-specific creatine kinase promoter. These mice displayed progressive muscle weakness beginning at around six months of age, recapitulating, at least in part, the myopathy associated with IBMPFD. Mice homozygous for the R155H mutation exhibit accelerated pathology and typically die between post-natal days 14-21, due to severe muscle, spinal cord and cardiac pathology (Nalbandian *et al.*, 2012). Indeed, in our lab, we found that homozygous VCP$^{R155H/R155H}$ mice were extremely difficult to generate. Heterozygous knock-in expression of VCP$^{R155H/+}$ in the mouse model results in a slower onset of disease pathology at approximately 6-9 months of age, thus enabling researchers to examine the cumulative age-dependent functional and pathological effects of VCP mutation in the adult and aged animal (Badadani *et al.*, 2010; Nalbandian *et al.*, 2013a).

Cytoplasmic and nuclear accumulation of proteinaceous inclusions is seen in myofibrils of the VCP$^{R155H/+}$ mouse – a hallmark of the human disease (Weihl *et al.*, 2007). VCP$^{R155H/+}$ mice gain mass at the same rate as wild-type littermates as they age. From approximately six months of age onwards, however, progressive muscle weakness was observed in the forelimbs of the mutant mice, as determined by a grip strength test. Rotarod testing, involving timed running on a horizontal rotating rod, was also implemented in order to assess motor coordination, endurance and fatigue, with results also showing reduced performance in mutant mice.

The VCP$^{R155H/+}$ mouse is of particular importance as a tool of research, as the substitution of the arginine residue with a histidine moiety (base pair change of C<u>G</u>C to C<u>A</u>C) at the amino acid position 155 is the most encountered VCP mutation linked to IBMPFD (Watts *et al.*, 2004). Both human and murine VCP comprises 806 amino acids, with the homologues differing by a single amino acid residue at the 684 position (Müller *et al.*,

1999). Numerous studies have explored the molecular spectrum of pathological phenotypes in the VCP$^{R155H/+}$ mouse model, in attempts to elucidate the possible cellular pathways that may be disrupted by VCP mutations.

An interesting feature of the disorder, observed by Badadani and colleagues (2010), was the presence of abnormal, swollen mitochondria in cryosections of quadriceps muscle obtained from aged knock-in VCP$^{R155H/+}$ mice (Badadani *et al.*, 2010). This may suggest a possible detrimental effect of VCP mutation on the energy metabolism of skeletal muscle. In recent years, the role of VCP in mitochondrial maintenance in cells has been investigated in depth. In 2006, researchers investigated mitochondrial function in a yeast model in which Cdc48, the VCP homolog in yeast, was mutated (Braun *et al.*, 2006). Ultrastructural analysis of wild-type Cdc48 and Cdc48^{S565G} yeast cells revealed abnormally large mitochondria in the mutant strain. Increased levels of cytosolic cytochrome *c* were observed in the Cdc48^{S565G} cells, suggesting a possible decrease in mitochondrial membrane integrity in the mutant cells. The respiratory capacity of the Cdc48^{S565G} cells was also compromised. A differential plating assay showed that the mutant cells were unable to proliferate on a lactate-rich medium, indicating an inability of these cells to utilise mitochondrial lactate oxidation to provide energy (Braun *et al.*, 2006). The potential effects of mutant VCP expression on mitochondrial integrity and dynamics therefore warrant further investigation, as a reduction in the capacity of the mitochondrial network to generate the ATP could have profound effects on the survival of the cell. To that end, one of our primary aims was to investigate the effects of VCP$^{R155H/+}$ expression on normal cellular function, specifically on the ability of skeletal muscle cells to contract and produce force.

1.5 Mitochondria - dynamics and degradation

Mitochondria are complex organelles, which form an interconnected tubular network under homeostatic conditions in the cell. This dynamic morphology is derived primarily from cyclical fission and fusion events between individual mitochondria and those in the network. The outer mitochondrial membrane (OMM) envelops the inner mitochondrial membrane (IMM) which contains the mitochondrial DNA in a protein-rich matrix. The IMM comprises numerous invaginations, or cristae, due to its large surface area, when compared to the OMM. These cristae are joined to the boundary intermembrane space (IMS) via thin tubular junctions. The highly flexible IMM and cristae undergo morphological changes when exposed to alterations in matrix volume and/or cellular metabolic state. Metabolic and apoptotic pathways are regulated, in part, by the mixing of biomolecular contents between the intra-cristae and IMS. The metabolic state of the mitochondrion itself also influences the conformation of the network (Heath-Engel and Shore, 2006).

The primary function of the mitochondrial network is to generate ATP. For this to occur, a proton gradient must be established between the membranous spaces inside the mitochondrion. The electron transport chain (ETC), comprised of a series of IMM protein complexes, shuttles electrons from electron donors to electron acceptors, via redox reactions. These reactions are coupled with the transfer of protons across the IMM to the IMS, which creates an electrochemical gradient. The gradient is used by the F_0F_1 ATP synthase complex to generate ATP via oxidative phosphorylation, as the chemiosmotic flow of H^+ ions into the mitochondrial matrix from the IMS facilitates the phosphorylation of ADP by F_0F_1 ATP synthase.

Mitochondrial fusion helps to mitigate stress encountered by isolated mitochondria, by allowing the potentially damaging contents of the dysfunctional organelle to dissipate into the combined matrix of the mitochondrial network. Indeed, in cultured fibroblasts, the green fluorescent protein contained in a single mitochondrion was redistributed throughout the entire mitochondrial network in one hour, as a result of rapid fusion/fission events (Youle and van der Bliek, 2012). Fission events are required for the generation of new mitochondria, but also function in homeostatic 'quality control', by facilitating the extraction of terminally dysfunctional mitochondria from the network, thus preserving the integrity of the network (Heath-Engel and Shore, 2006).

In mammalian cells, fusion and fission of mitochondria is facilitated by large guanosine triphosphatases (GTPases) from the dynamin family (collectively referred to as dynamin-related proteins, or DRPs), whose actions fuse and divide both the IMM and OMM (Ding *et al.*, 2012). DRPs constitute a specialized subfamily of GTPases, which act as molecular motors to drive membrane remodelling (Escobar-Henriques and Anton, 2013). Mitofusins (Mfn) 1 and 2 are constitutively-expressed, OMM transmembrane GTPase proteins, which mediate the initial GTP-dependent mitochondrial docking/tethering events, when two mitochondrial tips or tubules are in close proximity to each other. Optic atrophy protein 1 (OPA1) is a key mediator of IMM fusion. Knock-out of Mfn1, or Mfn2, or OPA1 is embryonic-lethal (Chen et al., 2003; Davies et al., 2007). When Mfn2 is depleted after placental formation, mice exhibit impaired cerebral development, with a third of offspring dying at post-natal day 1 (Chen *et al.*, 2007; Escobar-Henriques and Anton, 2013). Mice depleted of Mfn1 after placental formation are normal, indicating that only after this developmental stage, Mfn1, and not Mfn2, is dispensable (Chen *et al.*, 2007). Mouse embryonic fibroblasts which lack both Mfn1 and Mfn2 or OPA1 (Chen *et al.*, 2005) exhibit impaired mitochondrial membrane potential and respiratory capacity, highlighting the vital nature of mitochondrial fission and fusion for normal cellular and organism development and function.

The turnover of Mfn1 and Mfn2 is mediated by the ubiquitin/proteasome system (UPS). In cell culture studies, proteasomal inhibition by MG132 was shown to stabilize both Mfn1 and Mfn2 and prevent their degradation. The reversible mitochondrial uncoupler, carbonyl cyanide m-chlorophenylhydrazone (CCCP), is routinely used to investigate mitochondrial dynamics. CCCP is a protonophore, and as such, causes rapid depolarization and fragmentation of mitochondria, by dissolving into the mitochondrial membrane and increasing its ionic permeability, specifically its permeability to H^+. Exposure to this compound was shown to stimulate Parkin-dependent autophagic degradation of mitochondrial fusion proteins (Tanaka *et al.*, 2010). PTEN (phosphatase and tensin homolog)-induced putative kinase 1, or PINK1, is an IMM-localised kinase involved in the initiation of mitophagy. Under homeostatic conditions, PINK1 is cyclically produced and cleaved, with the cleavage product being proteolytically degraded. When mitochondrial membrane potential is lost, PINK1 becomes stabilised and accumulates on the OMM. This acts as a signal to Parkin (Ashrafi *et al.*, 2013). Parkin, a cytosolic E3-ubiquitin ligase encoded by the *PARK2* gene, has been shown to translocate to functionally-impaired mitochondria. Upon translocation, the E3-ubiquitin ligase activity of Parkin increases,

which results in the increased ubiquitination of mitochondrial substrates, such as Mfn1, Mfn2 and VDAC1 (voltage-dependent anion-selective channel protein 1; Tanaka *et al.*, 2010; Narendra *et al.*, 2008). It has been suggested that both Parkin and PINK1 are involved in a common pathway which governs mitochondrial function and morphology, with PINK1 located upstream of Parkin. Interestingly, this pathway was negatively affected by the expression of an ATPase-deficient VCP mutant, VCP[E305Q/E578Q] (Tanaka *et al.*, 2010). The E305Q mutation in the D1 domain and the E578Q mutation in the D2 domain result in a catalytically-dead VCP, however this double mutation is not seen clinically (Dalal *et al.*, 2004; Tresse *et al.*, 2010, Watts *et al.* 2004). When HeLa cells transiently expressing the dominant negative ATPase-deficient VCP[E305Q/E578Q] mutant were treated with CCCP, Mfn1 ubiquitination increased, yet its degradation via the PINK1-Parkin-mediated pathway was predominantly prevented (Tanaka *et al.*, 2010), suggesting a key role of intact VCP in this pathway (Figure 1.5).

Most of the reported cellular roles of VCP involve recognition of and binding to (poly)ubiquitinated proteins, and either their segregation from associated binding partners or extraction from multiprotein complexes or membranes. It is possible therefore, that VCP may be acting as a segregase to remove these ubiquitinated mitochondrial proteins from the OMM, and that pathogenic VCP mutations impact on this function by preventing correct substrate binding, as evidenced by the build-up of ubiquitinated mitochondrial proteins (Tanaka *et al.*, 2010).
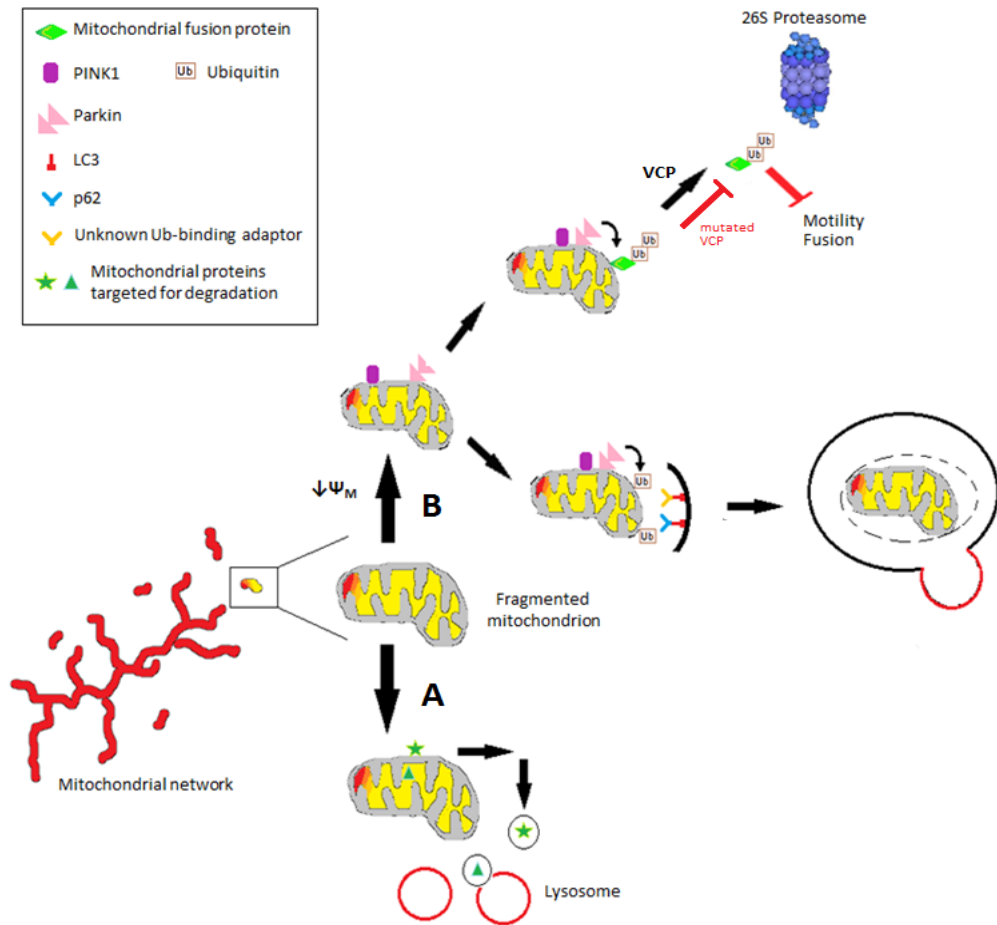
Figure 1.5. **Major pathways of mitochondrial quality control.** (A) Dysfunctional mitochondrial proteins are selectively degraded via vesicular transport from the mitochondria to the lysosome. (B) When the mitochondrial membrane potential (Ψ_M) is lost in a single mitochondrion, they are selectively removed from the network by the degradation of OMM fusion proteins, facilitated, in part, by VCP as part of the UPS. PINK1 becomes stabilised on the OMM upon dissipation of Ψ_M, and recruits cytosolic Parkin. Parkin-mediated hyper-ubiquitination of the OMM is recognised by p62 and other possible unidentified Ub-binding adaptors, which may be involved in the recruitment of the damaged mitochondria to the isolation membrane. This activity occurs through the interaction of these adaptors with LC3, an autophagosomal protein localised to the pre-autophagosomal membrane (Adapted from Ashrafi *et al.*, 2013).

As the list of molecular functions of VCP continues to lengthen, it has become more important to clearly define the pathways in which cellular dysfunction occurs when mutated VCP is expressed. *In vitro* studies have provided further evidence of the role of VCP in mitochondrial maintenance. Using a *Drosophila* model of VCP mutation, Kim and colleagues (2013) demonstrated that VCP recruitment to damaged mitochondria required Parkin-mediated ubiquitination of OMM proteins. As in the VCP$^{R155H/+}$ mouse model, severely abnormal mitochondrial swelling and disorganisation (mitochondrial megaconia and pleioconia) were noted in the muscle tissue of VCP mutant flies. Indeed, VCP was shown to be essential in the degradation of mitochondrial membrane proteins and the clearance of dysfunctional mitochondria, as siRNA-mediated knock-down of VCP prevented the proteasomal degradation of Mfn1 and Mfn2 in HeLa cells stably expressing Parkin. This function of VCP was shown to be impaired when pathogenic VCP mutants were transiently overexpressed in the model, specifically the catalytically-dead VCP mutant, VCP$^{E305Q/E578Q}$, or the clinically relevant VCP^{A232E} mutant (Kim *et al.*, 2013).

Further studies have identified the significance of functionally intact VCP in mitochondrial membrane protein homeostasis. Xu and colleagues (2011) showed that VCP is integrally involved in the extraction of ubiquitinated Mfn1, Mfn2 and Mcl1, an OMM-associated anti-apoptotic protein, from the OMM, thus enabling their degradation by the proteasome. Again, this extraction process was inhibited when the ATPase activity of the protein was ablated, as evidenced by a build-up of ubiquitinated Mcl1. Of note, these experiments were conducted in HeLa cells, which do not endogenously express Parkin (Xu *et al.*, 2011, Matsuda *et al.*, 2010). This may provide evidence for a Parkin-independent role of VCP in mitochondrial maintenance. These observations are important in light of the pathogenesis of IBMPFD, as the tissues affected by the disease, such as skeletal muscle, do not express high levels of the Parkin protein. For this reason, the mechanism by which VCP mutation affects mitochondrial maintenance, in tissues with low Parkin expression (such as muscle), warrants further investigation, as it is in these tissues that the pathology presents in patients.

The observation of abnormal, swollen mitochondria in VCP disease models prompted researchers to investigate the potential effects of VCP mutation on mitochondrial membrane potential. Human fibroblasts isolated from patients carrying three different mutations in VCP; R155H, R155C and R191Q; showed decreased mitochondrial membrane potential. Membrane potential-dependent mitochondrial uptake of tetramethylrhodamine methyl (TMRM) was reduced in these cells (Bartolome *et al.*,

2013). The authors also reported significantly increased oxygen consumption in VCP-mutated primary fibroblasts, compared with wild-type controls, however, ATP production was significantly decreased. These observations indicate that expression of a VCP mutant results in the uncoupling of oxidative phosphorylation and ATP generation.

Based on these studies, it is clear that our VCP$^{R155H/+}$ knock-in mouse model could serve to further investigate potential effects of VCP mutation on mitochondrial maintenance and quality control. We focused our investigations on skeletal muscle tissue, to examine possible effects of VCP mutation on the ability of mitochondria to generate ATP for prolonged muscle contractile activity. Progressive muscle weakness is a symptom seen in both IBMPFD patients and knock-in VCP$^{R155H/+}$ mutant mice, with respiratory failure due to muscle weakness being the main cause of death in patients. Forelimb muscle strength of wild-type and VCP$^{R155H/+}$ mice has been compared, using grip strength testing (Nalbandian et al., 2012). Mouse forelimbs consist of muscles made up of numerous fibre types, therefore any differences in strength or contractile force seen in grip strength tests cannot be attributed to a specific muscle fibre type. Indeed, to our knowledge, fibre type-specific effects of VCP mutation on striated muscle function have not yet been investigated, therefore it important that the biomechanical and functional effects of VCP mutation are investigated in muscles composed of different fibre types.

One of the hallmark methods of mammalian skeletal muscle classification is based on myosin heavy chain (MHC) isoform expression. The main fibre types found in skeletal muscle are type I, IIA, IIX and IIB, and while all four MHC isoforms are found in rodent skeletal muscle, the MHC IIB isoform is not present in human muscle (Smerdu et al., 1994, Schiaffino et al., 2011, Westerblad et al.,, 2010). The rate of cross-bridge cycling, and thus the maximal shortening velocity, is determined by the MHC isoform expressed in a given muscle cell, with the slowest being type I, type IIA being classified as intermediate and IIX/B being the fastest (Westerblad et al., 2010). Faster MHC isoforms consume ATP at a higher rate than the slower subtype, therefore fibre type classification based on this parameter is relevant in the context of fatigue.

Fast/type II and slow/type I muscles differ in both mitochondrial content and the metabolic pathways used to generate ATP. The hydrolysis of ATP to ADP and inorganic phosphate (P_i) is the mechanism by which energy for all cellular functions, including skeletal muscle contractile activity, is derived. Skeletal muscle exhibits the unique ability to rapidly increase its energy consumption when switching from a resting state to one of high

contractile activity. In order to efficiently meet these dynamic energy demands, skeletal muscle has evolved mechanisms by which ATP can be resynthesized quickly (Schiaffino *et al.*, 2011). Fast and slow muscles rely on different ATP-generating pathways - glycolysis and oxidative phosphorylation, respectively. Oxidative mitochondrial processes generate nearly all of the ATP required for slow muscle contraction, while fast-twitch muscles primarily utilise anaerobic glycolytic processes for rapid ATP generation, which limits the duration of contractile activation due to the dependency upon intramuscular glycogen stores (Allen *et al.*, 2008). One of the main determinants of fatigue resistance in skeletal muscle is mitochondrial content, and therefore oxidative capacity.

1.6 Aims and objectives:

1.6.1 Aim 1:

We hypothesise that the fatigue tolerance of the $VCP^{R155H/+}$ knock-in mouse muscle will be deficient when compared with WT controls. To test this hypothesis, we will characterise the biomechanical properties of different muscle fibre types in aged $VCP^{R155H/+}$ and WT mice. We will subject fast- and slow-twitch muscle fibre bundles, isolated from age-matched WT and $VCP^{R155H/+}$ mice, to an electrophysiological protocol, where contractile characteristics, specific force and fatigue tolerance will be assessed. This will further broaden our understanding of myopathic dysfunction in the IBMPFD disease model, as we will investigate the functional effects of $VCP^{R155H/+}$ in two different muscle types, the fast-twitch *extensor digitorum longus* (EDL) and the slow-twitch soleus, two muscles comprised of different fibre types.

1.6.2 Aim 2:

Based on the observations of Badadani and colleagues, we hypothesise that mitochondrial degradation may be affected by $VCP^{R155H/+}$ mutation. If the mutation does affect mitochondrial maintenance, the expression profiles of skeletal muscle fibre types may have adapted to utilise a different metabolic pathway for ATP generation. Therefore, we will examine the relative abundance of fibre types by immunostaining cryosections of muscle, to determine whether the expression of mutated VCP affects the distribution of different fibre types in skeletal muscle. We will also determine mitochondrial enzyme activity in $VCP^{R155H/+}$ and WT age-matched muscle, to gain insight into the effect of $VCP^{R155H/+}$ expression on mitochondrial respiratory activity.

1.6.3 Aim 3:

Studies have demonstrated that VCP is required for the successful degradation of mitochondrial fusion proteins. We hypothesise that due to the presence of dysfunctional VCP in cells, the mitochondrial networks will not respond normally to exogenous stresses. Using tissues from our $VCP^{R155H/+}$ mouse model, we will isolate and culture primary cells. We will examine the effects of oxidative stress on mitochondrial morphology, specifically on the ability of the network to effectively change its conformation, to adapt to such exogenous stresses. In addition, we will look at mitochondrial content in skeletal muscle, to determine whether $VCP^{R155H/+}$ expression affects overall mitochondrial density in this tissue.

Chapter 2

Materials and Methods

2.1 VCP$^{R155H/+}$ mouse model

The heterozygous VCP$^{R155H/+}$ mutant mice used for protein analysis and muscle mechanic experiments were generated by Badadani and colleagues (2010). Using a FRT-flanked Neomycin (Neo) cassette insertion, cultured 129/SvEv embryonic stem cells were modified to express the pathological VCP$^{R155H/+}$ mutation, and injected into 129/SvEv blastocysts. The blastocysts were implanted in pseudopregnant females, and the chimeric offspring produced were mated with 129/SvEv mice, resulting in the F1 mutant generation. VCP$^{R155H/+}$ mutant mice were back-crossed with mice of the C57BL/6 strain over six times, resulting in mice that retained >98% genetic homology with the C57BL/6 strain.

2.1.1 Genotyping of VCP mice

A polymerase chain reaction (PCR) protocol was used to determine the mouse genotypes. For this, an ear punch or tail tip was taken from each mouse and placed in a sterile Eppendorf tube. The tissue was then digested using the HotSHOT alkaline lysis method (Truett *et al.*, 2000). Briefly, 75µl of alkaline lysis reagent (25mM NaOH, 0.2mM disodium EDTA in ddH$_2$O, pH 12) was added to the tissue sample and was heated to 95°C for 30-60 minutes. The tissue sample was checked at 30 minutes and the tubes agitated in order to estimate the degree of lysis. Once lysed, the tissue sample was cooled to 4°C and 75µl of neutralisation buffer (40mM Tris-HCl in ddH2O, pH 5) was added. The samples were centrifuged at 775g for 3 minutes and the supernatant transferred to another sterile Eppendorf tube. The region encoding VCP in the genomic DNA template was amplified using 'mus-vcp-genot-F' and 'mus-vcp-genot-R' primers (sequences of these primers detailed in Table 2.1 and the PCR running conditions are listed in Table 2.2).

To confirm the genotype, PCR products were digested with either restriction enzymes MspI (cuts WT allele) or NcoI (cuts mutant allele) restriction enzymes for 3 hours at 37°C. Fragments were separated on a 1% agarose gel at 120V for 1hour (Fig. S.1, supplementary data).

Table 2.1 List of oligonucleotides used

Primers	Sequence
mus-gen-2F	5' - TGGAAGGCATCACTGGCAATCTCT
mus-gen-2R	5' - TTAAGGCCATCCAATCTCCAAAAGTA

Table 2.2 PCR running conditions

PCR step	Tm	Time	Cycles
Initial denaturation	94°C	2 minutes	1
• Denaturation	94°C	30 seconds	35
• Annealing	60°C	30 seconds	
• Extension	72°C	1.5 minutes	
Incubation	72°C	5 minutes	1
Cycle completion	4°C	∞	1

2.2 *Ex vivo* skeletal muscle biomechanics

2.2.1 Muscle fibre bundle isolation

All animals used in biomechanics experiments were euthanized by cervical dislocation according to the Animals (Scientific Procedures) Act 1986, UK and all the experiments conformed to the local animal welfare committee guidelines. Hind limbs were removed and the EDL and soleus muscles were isolated and excised. Once excised, the muscles were gently stretched and pinned in place using surgical steel pins in a bath of Ringer's solution containing 109mM NaCl, 5mM KCl, 1mM MgCl2, 4mM CaCl2, 24mM NaHCO3, 1mM NaHPO4, 10mM sodium pyruvate plus 200 mg/l foetal bovine serum (FBS). The majority of muscle fibres were then dissected away leaving approximately 6-10 intact muscle fibre bundles. The cross-sectional diameter (in μm) was recorded twice and averaged in order to calculate the specific force produced in each contraction.

2.2.2 Muscle fibre fatigue protocol

The muscle fibre bundles were mounted horizontally in a stainless steel chamber between a force transducer and a motor using aluminium T clips attached to tendon. The chamber was constantly perfused with Ringer's solution prepared as previously described and chamber was thermostatically maintained at 20°C using a thermocouple device. The sarcomere length (SL) was adjusted to give maximum tetanic tension (L_0) using laser diffraction (SL ~ 2.5μm) (He-Ne laser; Laser Lines Ltd, Oxon, UK).

Fibre bundles were given 10-20 minutes to equilibrate in the chamber before the beginning of the fatigue protocol (FP). Maximum twitch and tetanic contractions were elicited as a control at a non-fatiguing stimulation rate of once every ninety seconds, and the rate was increased to once every nine seconds for EDL and once every four seconds for soleus during the FP. In fast-twitch fibre bundles, tetanic contractions were produced by applying the electrical stimulus at a frequency of 120 Hz for a duration of 100-150 milliseconds, while in slow-twitch fibre bundles, a stimulation frequency of 30-40 Hz for 500 milliseconds was required. Due to the fatigue-resistant nature of slow muscle fibres, a higher stimulation rate was used in the slow muscle fibre FP. The contraction stimulation rate was returned to once every ninety seconds when 65-75 contraction recordings had been made. Contractions were elicited at this rate for 10-15 minutes to allow the fibres to recover from the FP. Recovery was classified as a return to ≥90% P_0 (control tension) within 10-15 minutes. The force produced by the muscle fibre bundle and the temperature (from

the thermocouple) signals were collected via a CED 1401Micro laboratory interface using Signal 2.11 software (Cambridge Electronic Design Ltd, Cambridge, UK) and stored in a computer. The amplitude of the twitch and tetanus (in mN) was determined using the Signal 3.1 software.

2.3 Mitochondrial respiration in skeletal muscle

2.3.1 Citrate synthase assay

Buffers and reagents required for the assay were prepared as described in the product technical data sheet. Whole EDL muscles, which had been previously snap frozen in liquid nitrogen and stored at -80°, were homogenised using a TissueLyser LT homogeniser (Qiagen). All eppendorf tubes and homogenisation tungsten beads were precooled using dry ice. For the tissue preparation, Cellytic MT Cell Lysis Reagent (Sigma) supplemented with HALT^{TM} Protease Inhibitor Cocktail (1:100 dilution, Sigma) was used in a ratio of 1 gram of tissue per 20mls of reagent. Each EDL was weighed and the appropriate volume of lysis reagent was calculated and added to a precooled eppendorf tube containing the EDL and a 5mm tungsten bead. The tissue was then homogenised at 50 Hz for 8-10 minutes. Next, the lysate was centrifuged at 14,000 RPM for 10 minutes and the supernatant collected into a fresh eppendorf tube, with 5µl aliquoted separately for BCA protein concentration analysis.

For the CS assay, an Omega (Model) spectrophotometric plate reader was set at 412nm on a kinetic program, with absorbance being measured at 10 second intervals for 90 second period. The assay solutions were warmed to 25°C before starting the reaction and aliquoted into the plate as per Table 2.3.

Table 2.3 Reaction scheme for citrate synthase assay in 96-well plate

Description	Sample	1× Assay Buffer	30 mM Acetyl CoA Solution	10 mM DTNB Solution	10 mM OAA Solution Last to be added
CelLytic M Sample*	x (2-8 μl)	186 – x μl	2 μl	2 μl	10 μl
Citrate Synthase (positive control) Diluted Solution	x (1-2 μl)	186 – x μl	2 μl	2 μl	10 μl

Initially, the absorbance of the reaction mixture was recorded for 90 seconds to measure baseline reaction, endogenous levels of thiol or deacetylase activity. 10μl of 10mM OAA solution was added to each well using a multichannel pipette in order to initiate the reaction in each well simultaneously. The plate was shaken gently for 10 seconds before the absorbance was recorded, again, once every 10 seconds for a total of 90 seconds, to measure total CS activity. The absorbance values (A_{412}) were plotted against time for each reaction, and the change in absorbance (ΔA_{412})/minute in the linear range of the plot was measured for endogenous activity and then for total activity (following the addition of 10mM OAA). The net CS activity was calculated by subtracting the (ΔA_{412})/minute of the endogenous activity from the (ΔA_{412})/minute of the total activity of the sample. Citrate synthase activity (mmole/ml/min) then was calculated using the following equation:

$$\{(\Delta A412)/min \times V(ml) \times dil\} / \varepsilon^{mM} \times L(cm) \times V_{enz}(ml)$$

Where: (ΔA_{412})/minute - net CS activity

V(ml) – the reaction volume (0.2ml in 96 well plate)

dil - the dilution factor of the original sample

ε^{mM} - the extinction coefficient of TNB (13.6 at 412nm)

L(cm) – the pathlength for absorbance measurement (0.552cm for 96 well plate)

V_{enz}(ml) – the volume of the enzyme sample in ml

The change in absorbance ($\Delta A412$)/min was plotted for each sample (with duplicate experimental sample data being averaged at the final stages of the calculations) and the CS enzyme activity in EDL muscles from three WT mice was compared with that of three VCP$^{R155H/+}$ mice using a two-tailed independent t-test to determine statistical differences. Despite n=3 for WT and VCP$^{R155H/+}$ fast-twitch muscle samples from Group 3, a t-test is considered a valid test to compare the means of two groups if the effect size is expected to be large (de Winter, 2013).

2.4 Protein expression in WT and VCP$^{R155H/+}$ knock-in mice

EDL muscle samples from WT and age-matched VCP$^{R155H/+}$ knock in mice were snap frozen in liquid N$_2$ and the total protein extracted using T-PER Tissue Protein Extraction Reagent (Thermo Scientific #78510) supplemented with HALT^{TM} Protease Inhibitor Cocktail. Western blot analysis and the Odyssey Infrared Imaging System (Licor) were used to assess any differences in protein expression between the groups.

2.4.1 Western blotting

Cells were lysed using M-PER Mammalian Protein Extraction Reagent (MPER) supplemented with Halt^{TM} Protease Inhibitor Cocktail. Total protein concentration was determined by BCA assay (BCA Protein Assay Kit; Thermo Scientific Pierce, 23227) according to the manufacturers' guidelines. For the SDS-PAGE, pre-cast 4-12% Bis-Tris (Novex, NP0335BOX) or 3-8% Tris-Acetate gels were used. Cell lysates were denatured by heating for 10 minutes at 70°C and then loaded into lanes at a volume equivalent to 15-20µg/ml. Gels were run at 120 V constant for 1 hour. Proteins were then transferred onto nitrocellulose membranes using the XCell II Blot Module (Invitrogen, EI9051). Filter pads, Wattman filter paper, NC membrane and the gel were assembled into a 'sandwich', ensuring the gel was closest to the cathode component of the module. Proteins in the gel were transferred to the nitrocellulose membrane at 30 V constant for 1 hour.

The membrane was then washed in 1xPBS for 1 minute to remove residual transfer buffer followed by 1 hour in Odyssey Blocking Buffer (Licor) supplemented with 0.01% Tween. The membrane was then incubated with primary antibodies (Table 2.4) in blocking buffer for 1 hour at room temperature, or overnight at 4°C. Following 4 x 5 minute 1xTBST washes, the membrane was incubated with secondary antibodies (Table 2.6) diluted in blocking buffer for 1 hour. Finally, the membrane was washed as per previous and analysed using the Odyssey Infrared Imaging System (Licor).

2.5 Molecular Biology Methods

2.5.1 Mammalian Cell Culture

Mouse embryonic fibroblasts (MEFs) were seeded in T75 flasks (Corning) at $2x10^5$ and cultured in Dulbecco's Modified Eagles Medium (DMEM) with GlutaMAX^{TM} (Invitrogen) supplemented with 10% HyClone heat-inactivated FBS (heated to 56°C for 30 minutes) and 0.5units/ml Penicillin and 50μg/ml Streptomycin solution (complete growth medium).

Cells were propagated in a humidified incubator at 37°C with 5% CO_2 until approximately 85-95% confluency was achieved, at which point cells were either passaged or subjected to a transfection protocol.

2.5.2 Isolation and culture of primary murine skin-derived fibroblasts

Young mice (aged <6 months; n=3 for both WT and VCP$^{R155H/+}$) were used for these experiments. Animals were sacrificed by cervical dislocation, and the abdomen of each mouse was sterilised with ethanol and the fur removed using a sterile razor blade. A skin biopsy of approximately 1.5cm^2 was removed and dipped briefly in 70% ethanol, then in PBS. The biopsy was cut into smaller pieces in a petri dish using a sterile scalpel. In a 6-well plate, 3-4 smaller pieces of the biopsy were placed (skin side up) in each well and allowed 10 minutes to dry in a 37°C incubator, to ensure the pieces adhered to the plate. 0.5ml of complete DMEM was added to each well and the plate was left for 3 days in a 37°C incubator with 5% CO_2. After 3 days, fibroblast cells were observed proliferating outwards from the skin patch. At this stage, another 0.5mls complete DMEM was added to provide nutrients. After a further 2 days, the skin patches were removed and the media replaced completely. The fibroblasts were cultured until sufficient numbers were achieved for mitochondrial dynamics/further experiments to be carried out.

2.5.3 Preparation of Luria-Bertani (LB) Medium

In order to make 1 litre of Luria-Bertani or LB medium, 10g Bacto-tryptone, 5g Bacto-yeast extract and 10g of NaCl were dissolved in 900mls ddH$_2$O in a sterile 1 litre storage bottle. When the additives were thoroughly dissolved, the pH was adjusted to 7.0 by adding concentrated NaOH drop-wise and the volume was then made up to 1 litre by adding ddH$_2$O. The solution was then sterilised by autoclaving at 120°C for 20 minutes. The medium was then allowed to cool and was stored at 4°C for no more than 3 months, at which point fresh medium was prepared. Antibiotics were freshly added to aliquots of LB medium as required.

2.5.4 Isolation of plasmid DNA from bacterial cell culture

Following 18-24 hours incubation at 37°C, Falcon tubes containing 10mls LB broth supplemented with either 50mg/ml ampicillin or 50-100mg/ml kanamycin inoculated with DH5α *Escherichia Coli* (*E. Coli*) bacteria were centrifuged at 9000 rpm for 10 minutes at 4°C. The LB broth was aspirated off, with care taken not to disturb the bacterial pellet. A QIAprep Spin Miniprep Kit (QIAGEN, #27104) was used to isolate and purify the plasmid DNA according to the manufacturers' protocol. Once the plasmid had been eluted in nuclease-free water, the DNA concentration was determined using an ultraviolet light spectrophotometer (NanoDrop ND-1000, Labtech).

2.5.5 Transfection

MEFs were plated in a 12-well plate containing a sterile glass cover slip. The complete growth medium was removed and replaced by antibiotic-free DMEM supplemented with 10% heat-inactivated FCS for a minimum of four hours prior to transfection in order to allow the highest transfection efficacy possible. Plasmids purchased were EGFP-tagged WT-VCP and EGFP-tagged VCP^{R155H} (plasmid maps of constructs in Supplementary data). The cells were transiently transfected with a complex of 1.6µg plasmid DNA and Lipofectamine 2000 transfection reagent (Invitrogen, #11668) in Opti-MEM^{TM} with GlutaMAX^{TM} (Invitrogen) according to the manufacturer's protocol. The cells were incubated for 24 hours at 37°C in order for protein biosynthesis to occur.

2.5.6 Immunostaining of transfected cells

Following the incubation period, the medium was aspirated from each well and the cells washed twice with warm PBS. A solution of 200nM MitoTracker^{TM} CMXRos (Molecular Probes, M-7512) was made using antibiotic-free DMEM^{TM} and cells were incubated at 37°C in this solution in the dark for 30 minutes. The MitoTracker^{TM} CMXRos solution was then aspirated off and the cells washed in warm antibiotic-free DMEM^{TM} for 5 minutes, followed by two PBS washes. Cells were then fixed in a 3.7–4% PFA solution for 20 minutes and washed several times using PBS. Cells were incubated with blocking buffer (PBS supplemented with 5% FCS and 0.01% Triton X) for 45 minutes at room temperature to block non-specific antibody binding. The cells were then incubated for either 1 hour at room temperature (RT) or overnight at 4°C on a shaking plate with primary antibodies (listed in Table 2.3) diluted in blocking buffer according to the product guidelines. Then cells were subjected to 4x5 minute washes with PBS-T (PBS with 0.1% Tween 20) and the secondary antibodies (listed in Table 2.4), also diluted in blocking buffer, were then added for 1 hour incubation at RT. Following 4xPBS-T washes, cover slips were mounted onto slides using approximately 20μL Vectashield with DAPI (Vector Laboratories). Immunofluorescence imaging was carried out using a Zeiss Imager M2 microscope with a CCD camera for fluorescence acquisition and images were processed using Axiovision Software (Version 4.8).

Table 2.4 *List of primary antibodies used for immunofluorescence*

Antibody	Company/code	Reactivity	Concentration	Dilution
Anti-VCP	BD TL/612183	Mouse	250µg/ml	1/1000
Anti-VCP	Cell Signal/2648	Rabbit	9µg/ml	1/1000
Anti-TOMM20	Sigma/HPA011562	Mouse	0.04mg/ml	1/1000
Anti-TOMM20	Sigma/HPA011562	Rabbit	0.04mg/ml	1/1000
Anti-actin	Sigma/A3853	Mouse	1.8mg/ml	1/3300
Anti-Parkin	Abcam/15954	Rabbit	1mg/ml	1/1000
Anti-Mfn2	Sigma/M6319	Rabbit	~1mg/ml	1/1000
Anti-MHCIIA	Novacastra	Mouse	Not available	1/5
Anti-MHCIIB	Novacastra	Mouse	Not available	1/5
Anti-Nidogen-1	In-house (Mayer lab)	Rabbit	Serum	1/2000
Anti-COX-IV	Abcam/ab14744	Rabbit	0.04mg/ml	1/1000
Anti-MHCf	Novacastra	Mouse	Not available	1/10
Anti-MHCs	Novacastra	Mouse	Not available	1/10

Table 2.5 *List of secondary antibodies used for immunofluorescence*

Antibody	Company/Code	Reactivity	Concentration	Dilution
Chicken Alexa Fluor 594	Mol Prob /A-21201	Mouse	2 mg/ml	1/1000
Chicken Alexa Fluor 594	Mol Prob/A-21442	Rabbit	2 mg/ml	1/1000
Chicken Alexa Fluor 488	Mol Prob/A-21200	Mouse	2 mg/ml	1/1000
Chicken Alexa Fluor 488	Mol Prob/A-21441	Rabbit	2 mg/ml	1/1000
Goat Alexa Fluor 350	Mol Prob/A-11045	Mouse	2 mg/ml	1/1000

Table 2.6 *List of secondary antibodies used for Western blotting (Odyssey Infrared Imaging System compatible)*

Antibody	Company/code	Reactivity	Concentration	Dilution
Goat anti-rabbit IRDye 680LT	Licor/926-32221	Rabbit	0.5mg/ml	1/10000
Goat anti-mouse IRDye 680LT	Licor/926-32220	Mouse	0.5mg/ml	1/10000
Goat anti-rabbit IRDye 800CW	Licor/926-32211	Rabbit	0.5mg/ml	1/10000
Goat anti-mouse IRDye 800CW	Licor/926-32210	Mouse	0.5mg/ml	1/10000

2.5.7 Immunostaining of mouse hind limb cryosections

After mice were sacrificed via CO_2 inhalation, hind limbs were removed at mid-femur level and frozen in isopentane cooled with liquid nitrogen. The limbs were stored at -80°C until further use. For sectioning, the limbs were mounted vertically onto a cryostat chuck using OCT medium. 10µm thin cryosections were cut from the limbs and placed onto polylysine coated microscope slides. Slides were stored at -20°C for a maximum of 3 days before immunostaining. Sections were rehydrated in PBS for 10 minutes. They were then fixed with 1% PFA in PBS for 10 minutes at RT in a humidity chamber. Three washes of PBS + 0.1% Tween-20 (PBS-T) for 5 minutes were performed.

Slides were permeabilized in methanol at -20°C for 8 minutes and then washed three times in PBS-T for 5 minutes. Non-specific binding was blocked using 5% FCS in PBS-T for 90 minutes at 37°C in a humidity chamber. Sections were then briefly rinsed with PBS-T. 1° and 2° antibodies were prepared by centrifuging at 13,000rpm for 5 minutes before use, then diluting in 2% FCS in PBS-T according to optimum working concentration (Table 2.4 and 2.5). Sections were incubated with 1° antibodies for 1 hour at 37°C in a humidity chamber. Sections were washed three times in PBS-T for 5 minutes at RT, and then incubated with 2° antibodies for 1 hour at RT in a humidity chamber.

After 2° antibody incubation, slides were washed twice with PBS-T for 5 minutes, followed by one 5 minute wash in PBS. Sections were then mounted with gelvatol (in-house) and stored in the dark at 4°C to set, until further analysis. The sections were labelled according to the mouse identification number they were taken from, therefore the investigators were blinded to the genotype until after the images had been analysed.

2.6 Data analysis

Data was analysed using a two-way ANOVA with Tukey post-hoc analysis, an unpaired student's t-test or a Mann-Whitney test of ranks. Significance was recorded when the resulting p-value was ≤0.05. A two-way ANOVA, also called two-factor ANOVA, determines how a response is affected by two factors, for example, genotype and stress condition. The unpaired t-test compares the means of two unmatched groups and the Mann-Whitney test of ranks is a nonparametric test comparing the distributions of two unmatched groups.

Chapter 3: Expression of VCP$^{R155H/+}$ decreases fatigue tolerance and increases post-fatigue recovery time in a fibre type-specific manner

3.1 Introduction

Mammalian skeletal muscle is a highly heterogeneous tissue. Its diversity stems from the numerous fibre types it is comprised of, which are metabolically suited to a wide range of functional requirements. During exercise, ATP is utilised by three different ATPases in skeletal muscle for contraction to occur. The sodium/potassium (Na$^+$/K$^+$)-ATPase pumps sodium ions out of and potassium into the muscle fibre following an action potential. ATP is also used by the myosin ATPase to generate mechanical force during cross-bridge cycling. The calcium (Ca^{2+}) ATPase is responsible for pumping cytosolic calcium back into the sarcoplasmic reticulum to facilitate muscle relaxation. Each of these ATPases, contributes 10, 60 and , 30% of total skeletal muscle ATP use, respectively (Homsher, 1987). Fast-twitch muscle fibres rely primarily on glycolysis to rapidly generate ATP for contraction, with longer term energy production facilitated by oxidative phosphorylation in the mitochondria (Schiaffino and Reggiani, 2011). If mitochondria in fast-twitch fibres are dysfunctional, the reduced capacity of the mitochondrial network to produce ATP for long term contractile activity would negatively affect the ability of fast fibres to resist fatigue.

We therefore hypothesised that possible pathogenic effects of VCP$^{R155H/+}$ mutation on skeletal muscle fatigue tolerance would be seen to a greater extent in fast-twitch glycolytic fibres as they contain fewer mitochondria, therefore rely more heavily on a fully functioning mitochondrial network for ATP generation for longer-term contractile activity. To that end, slow-twitch fibres would not be affected to the same degree by the VCP$^{R155H/+}$ mutation as they have a higher mitochondrial content, therefore the proposed detrimental effects of mitochondrial dysfunction on fatigue tolerance would be diluted into the larger mitochondrial network.

We conducted biomechanical experiments to examine the contractile properties of isolated muscle fibre bundles from the *soleus* and *extensor digitorum longus* (EDL) muscles. The myopathic effects of VCP mutation in IBMPFD patients have been well documented, however to our knowledge, fibre type specificity has not yet been investigated. In order to assess the functional consequences of mutated VCP expression, we conducted muscle mechanics experiments on fast- and slow-twitch muscle fibre bundles excised from age-matched VCP$^{R155H/+}$ mutant and wild type (WT) mice. We compared the rate and extent of force decline in fibre bundles during a fatiguing protocol. Fatigue is defined as the reversible decline in contractile force associated with continuous activity of muscle (Allen *et al.*, 2008). In order to determine whether the effects of VCP mutation, if any, were fibre type-specific, we used muscle fibre bundles dissected from the EDL and soleus. Skeletal muscle is a highly metabolically heterogeneous tissue (Pette, 1985), therefore it was important to select muscles which were classified as predominantly fast- or slow-twitch. The EDL muscle consists of MHC type IID/X (approx. 30%) and IIB (approx. 66%) fibres making this a glycolytic or fast-twitch muscle (Augusto *et al.*, 2004), which is metabolically suited to short bursts of rapid contractile activity and susceptible to fatigue. Therefore, a degree of fatigue in the EDL muscle fibre bundles was predicted upon exposure to a fatigue protocol. The soleus is a mixed muscle that is comprised mainly of oxidative fibres with fibre types I (approx. 40 %) and IIA (approx. 55%) present (Augusto *et al.*, 2004), thus making it more fatigue-resistant compared with the EDL.

3.2 Results

As the pathophysiological effects of VCP mutation are age-dependent, we chose to investigate potential biomechanical alterations in a cohort of animals divided into four age groups, as outlined in Table 3.1. Our preliminary muscle mechanics data indicated that, in accordance with the known age-dependent development of myopathy in IBMPFD, decrements in force production were observed in fast-twitch muscle fibre bundles from $VCP^{R155H/+}$ animals aged 350 days onwards. For this reason, we chose two age groups which were quite close together (Groups 2 and 3), in order to pinpoint the age at which the changes were seen to occur. We also chose an age range considered extremely aged (Group 4) in the context of the C57BL/6 mouse lifespan, as the average lifespan of this strain ranges from 827±14.4 days in males and 818±21.0 days in females (Goodrick *et al.*, 1975). We tested at least four fast and four slow muscle fibre bundles from each age-group in order to generate a comprehensive picture of the anticipated myopathic alterations. The data from the muscle mechanic experiments were compared statistically using an ANOVA and the results are represented graphically (Figures 3.1(A-E)-3.4(A-E)).

Table 3.1. Age groups of mice used in experiments.

Group	Age (days)	Age (months approx)
1	168 – 199	5.5 – 6.5
2	350 – 390	11.5 – 12.8
3	401 – 451	13.2 – 14.8
4	806 – 840	26.5 – 27.6

3.2.1. Neither fast- nor slow-twitch muscle specific force is affected by VCP[R155H/+] expression in any age group

We devised a minimal fatigue protocol (FP) in which muscle fibre bundles were initially allowed to equilibrate in the test chamber whilst being stimulated maximally for a pulse train of 100ms every 90 seconds pre-FP. For the FP, we elicited maximal isometric contractions at a rate of 1 stimulus every 9 seconds for fast-twitch fibre bundles and 1 every 4 seconds for slow-twitch bundles, for a total of 60 contractions. The stimulation rate was returned to 1 every 90 seconds for a period of 12-15 minutes to allow fibre bundles to recover to pre-FP force production (P_0). The rate and degree of fatigue was assessed using Signal 3.1 software.

Absolute specific force (as calculated by dividing the force produced, in mN, by the fibre bundle's cross-sectional area in μm^2) was recorded at specified contractions during the fatigue protocol and the collated data from at least four WT and VCP[R155H/+] fibre bundles in each age group were averaged (Figure 3.1 and 3.2). No significant differences were observed in absolute specific force between WT and VCP[R155H/+] fast- and slow-twitch fibres in any age group (Figures 3.1 and 3.2, respectively).
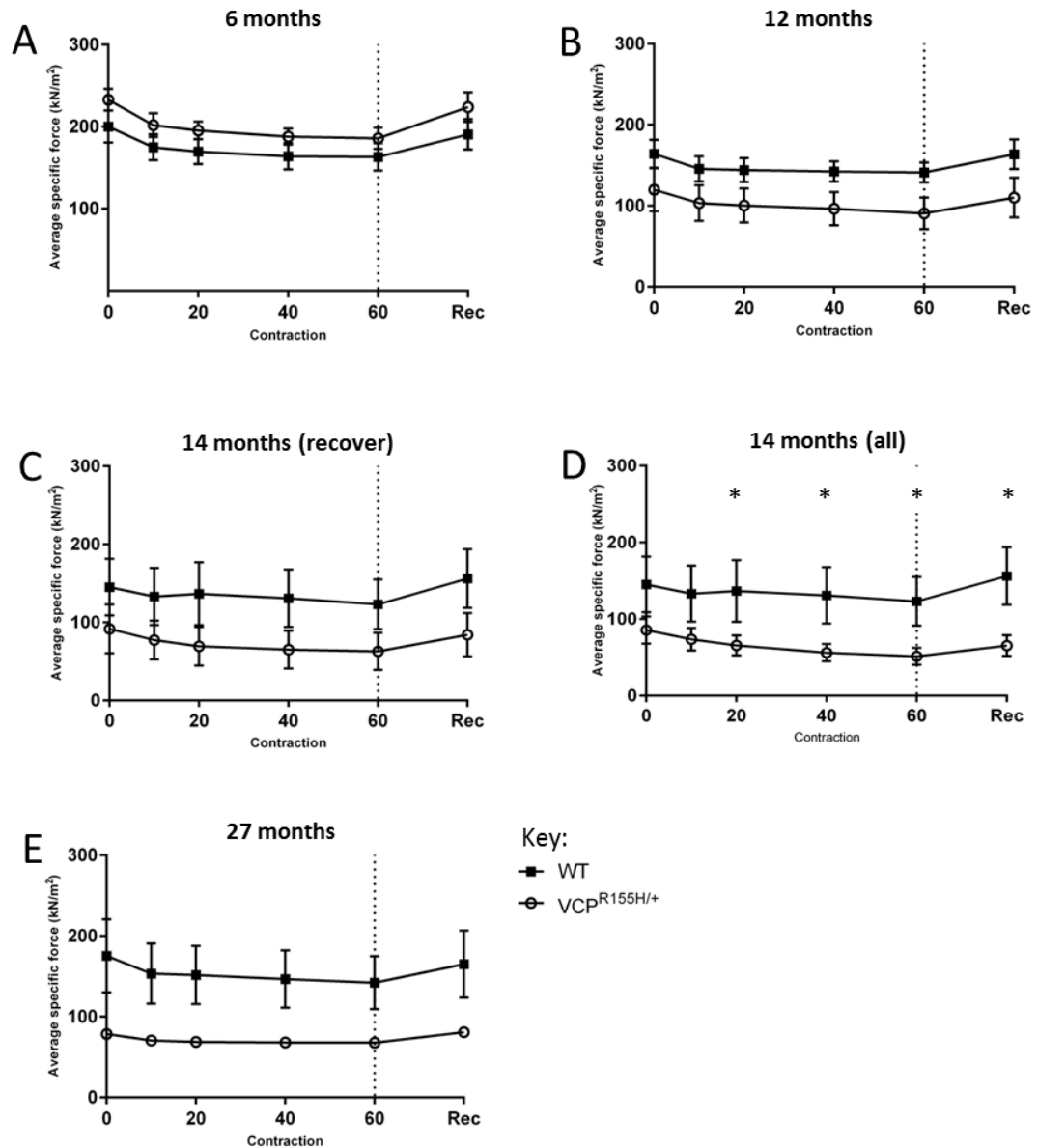
Figure 3.1 Comparison of rate and degree of fatigue of fast-twitch muscle fibre bundles from age-matched WT and VCP$^{R155H/+}$ mice. Averaged specific force generated by age-matched WT and VCP$^{R155H/+}$ fast-twitch muscle fibre bundles isolated from EDL. Contraction number is indicated on the x-axis. The vertical dashed line at contraction 60 indicates the end of the fatigue protocol and the beginning of the recovery period, where the stimulation frequency was returned to the pre-FP rate of 1/90sec. Note, in 14 months (Group 3), only 25% of VCP$^{R155H/+}$ fast-twitch fibre bundles used recovered to produce a contraction force of ≥90% of P0 following the fatigue protocol (the inclusion criteria for healthy, live fibre bundles), therefore C represents the FP force data from the VCP$^{R155H/+}$ fast-twitch fibres which recovered post-FP and D represents the pooled FP data from all VCP$^{R155H/+}$ fibres tested in this group including those which did not recover post-FP (n=12 in total). Solid squares represent WT and open circles represent VCP$^{R155H/+}$ data ±SEM. (Note: graphs represent data from at least 3 different mice for each condition; n≥3 fibre bundles for each condition). Asterisk indicates significance of $p<0.05$.
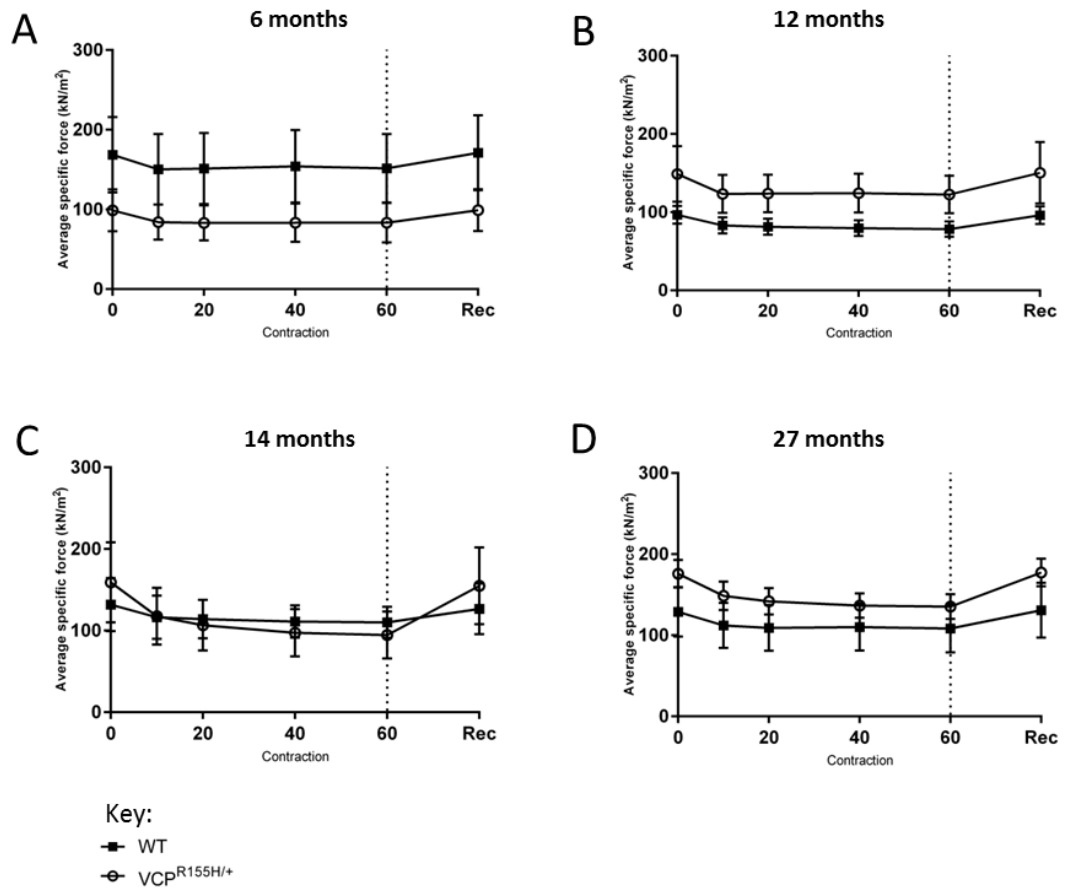
Figure 3.2 No significant differences observed in fatigue profiles of slow-twitch fibre bundles from WT and VCP$^{R155H/+}$ in any age group. Graphic representation of the rates of decrease in actual specific force in kN/m^2 of age-matched WT and VCP$^{R155H/+}$ slow-twitch fibre bundles during the fatigue protocol. Interestingly, at 12 months (Group 2) and 27months (Group 4) the slow-twitch fibre bundles produced greater specific force than age-matched WT fibre bundles. Values represent averaged specific force at the indicated contractions of the fatigue protocol ±SEM. Solid squares represent WT and open circles represent VCP$^{R155H/+}$ data (Note: graphs represent data from at least 3 different mice for each condition; n≥3 fibre bundles for each condition).

3.2.2. Effects of VCP$^{R155H/+}$ mutation on normalised specific force are age- and fibre type-specific

Due to the relatively high variation in standard error in actual specific force, we normalised specific force to the initial contraction of the FP, P_0. Significant differences in the rate and degree of fatigue between WT and VCP$^{R155H/+}$ muscle were revealed when absolute specific force was normalised to P_0. Fast-twitch fibres from 12 month old (Group 2) VCP$^{R155H/+}$ EDL fatigued to a greater extent than WT controls, with significantly lower normalised force produced by these fibres from contraction 40 onwards (Figure 3.3, B). A dramatic functional change in fatigue characteristics of 14 months old VCP$^{R155H/+}$ fast-twitch fibres was observed (Figure 3.3, C and D). Here, 75% of VCP$^{R155H/+}$ fast-twitch fibres tested did not recover to ≥90% of P_0 within the given post-FP recovery period of 15 minutes. Usually, any fibres that did not recover at least 90% of their initial contraction force would not be included in the analysis, but due to the high number of 'non-recovering' fibres in this group, these data points were included. A significant loss of fatigue resistance, from tetanus 40 onward, was seen in this age group (Figure 3.3, C). This high rate of attrition was not observed in any other age group, suggesting that this high proportion of non-recovering fibres and the loss of fatigue tolerance are due to a functional effect of VCP$^{R155H/+}$ mutation rather than possible fibre injury during isolation and subsequent death in the chamber. If the values of these non-recovering fibres are removed from the analysis, the only significant difference between WT and VCP$^{R155H/+}$ fast-twitch fibres is in the post-FP recovery rate. The fatigue resistance is unaffected (Figure 3.3, C).

In Group 5 (Figure 3.3, E), comprising the oldest mice used in these experiments (27 months of age), no significant differences were observed between the fatigue characteristics of VCP$^{R155H/+}$ mutant and control fast-twitch fibre bundles. Although not statistically significant, at 27 months of age the VCP$^{R155H/+}$ fast-twitch fibres appeared to recover slightly better than WT control fibres (Figure 3.3, E). The fatigue tolerance of slow-twitch fibres was not significantly different between WT control and VCP$^{R155H/+}$ mutant fibres in any age group (Figure 3.4, A-D). At 14 months of age, the VCP$^{R155H/+}$ slow-twitch fibres appeared to fatigue to a greater extent than WT controls, however this was not statistically significant (Figure 3.4, C). These results are summarised in Figures 3.5A and B, showing the average peak force produced by the last contraction (C60) in the fatigue protocol for all age groups.
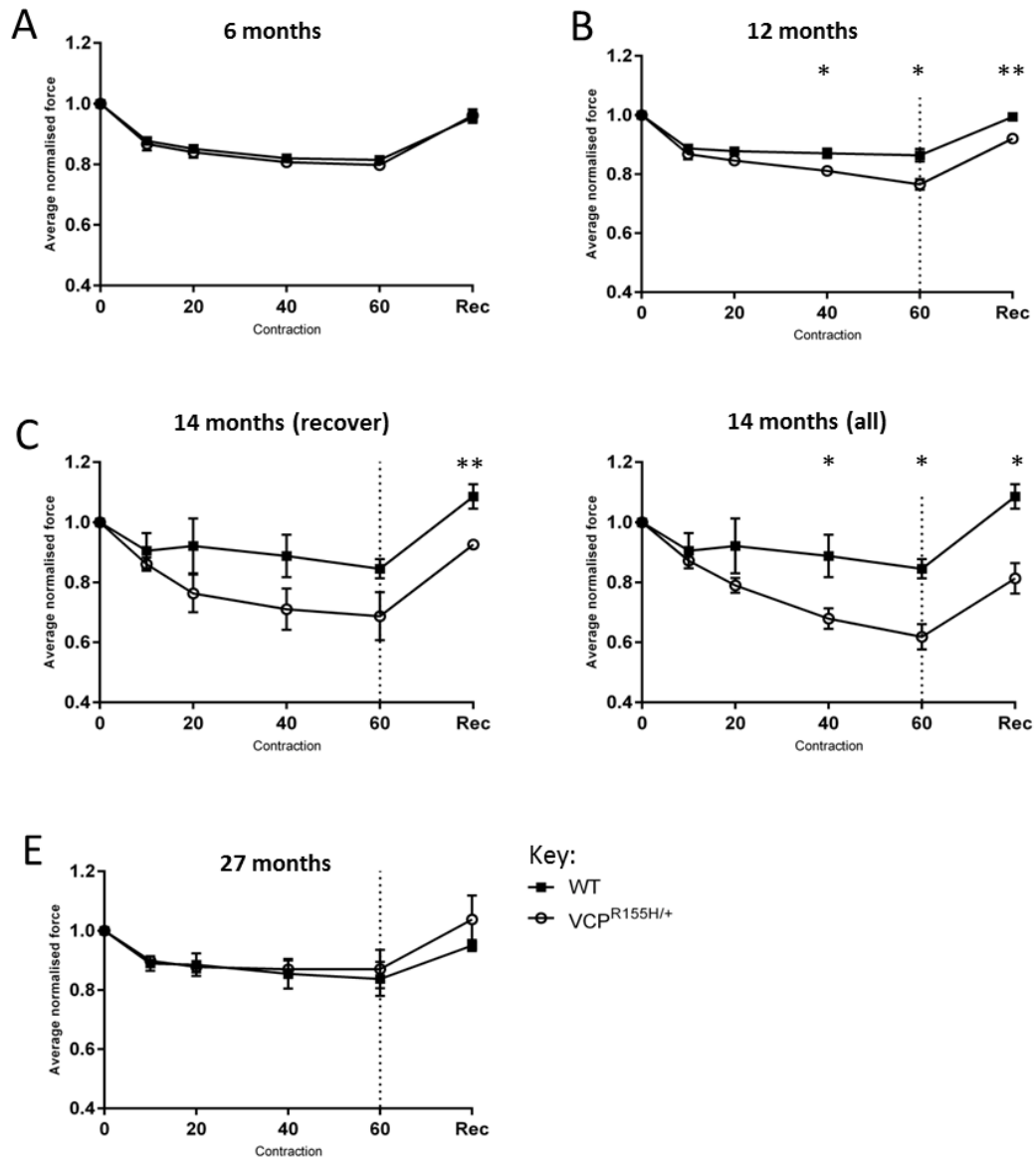
Figure 3.3 VCP$^{R155H/+}$ mutation results in an age-specific decrease in fatigue tolerance in fast-twitch VCP$^{R155H/+}$ fibres when compared with wild type controls. Averaged normalised specific force (P/P$_0$) was plotted at specified points during the fatigue protocol (FP) for each age group. The dashed line represents contraction 60, the final contraction of the FP and the beginning of the 12-15minute post-FP recovery period. At 6 months (Group 1), both WT and VCP$^{R155H/+}$ fast-twitch fibre bundles fatigue similarly and recover to the same degree following the FP. However, at 12 months (B, Group 2), VCP$^{R155H/+}$ fast-twitch fibres exhibit fatigue intolerance, evidenced by a significant reduction in normalised specific force compared with WT controls from contraction 40 onwards. As before, at 14 months (Group 3; C and D), only 25% of VCP$^{R155H/+}$ fast-twitch fibre bundles recovered to produce contraction force of ≥90% of P0 following the fatigue protocol (the inclusion criteria for healthy, live fibre bundles), therefore C represents the fatigue data from the VCP$^{R155H/+}$ fast-twitch fibres which recovered post-FP and D represents the pooled fatigue data from all VCP$^{R155H/+}$ fibres tested in this group including those which did not recover post-FP (n=12 in total). Solid squares represent WT and open circles represent VCP$^{R155H/+}$ data ±SEM. Asterisk (*) indicates significance of $p<0.05$, ** indicates $p<0.005$. (Note: graphs represent data from at least 3 different mice for each condition; n≥3 fibre bundles for each condition).

60
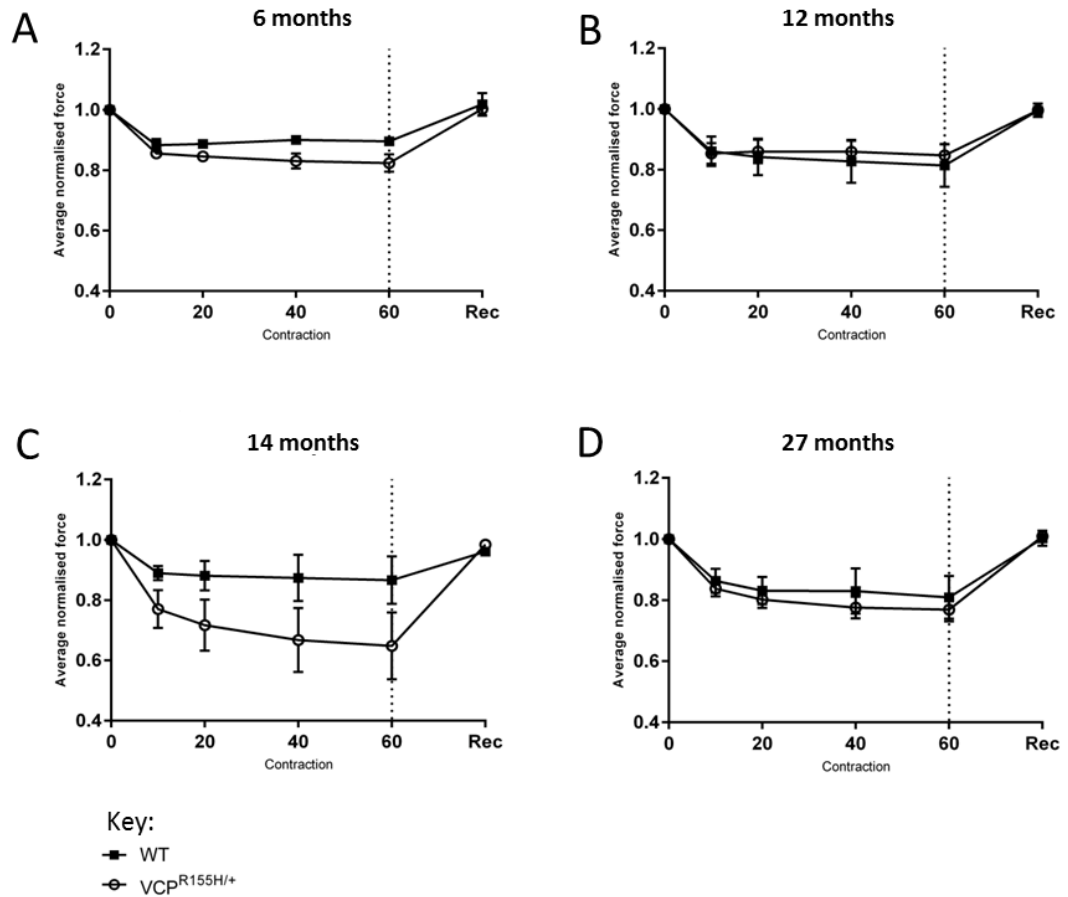
Figure 3.4 No significant differences found between WT and VCP$^{R155H/+}$ normalised slow-twitch fibre bundle specific force data in any age group. Specific force data from slow-twitch fibre bundles isolated from solei of age-matched WT and VCP$^{R155H/+}$ mice and subjected to the fatigue protocol was normalised (P/P$_0$). Statistical analyses did not reveal any significant differences between WT and VCP$^{R155H/+}$ slow-twitch fibre bundles in terms of rate of fatigue or recovery time post-FP in any age group (Note: graphs represent data from at least 3 different mice for each condition; n≥3 fibre bundles for each condition).
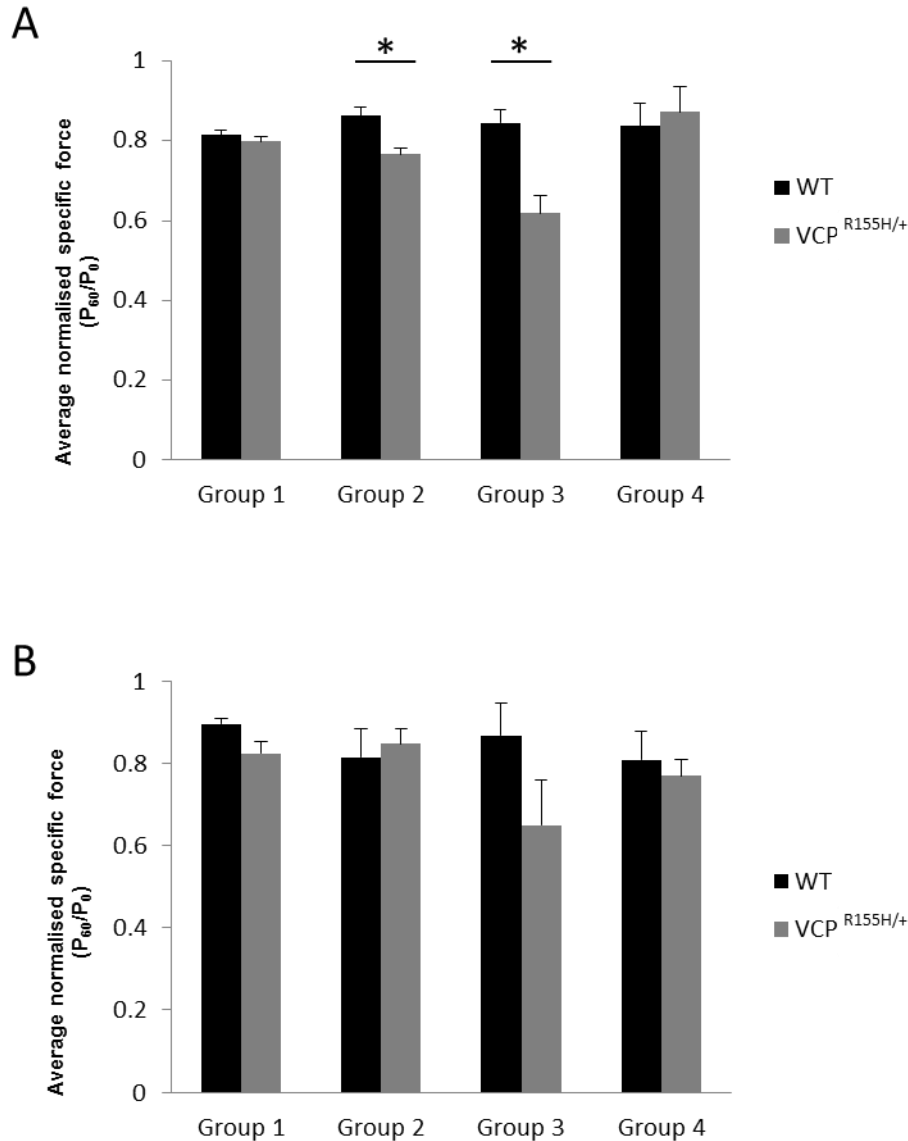
Figure 3.5 Significant decline in force production by fast-twitch fibre bundles from 12 and 14month old (Groups 2 and 3) VCP$^{R155H/+}$ mice during fatigue protocol. Graphs represent the decrease in force produced by fast-twitch (A) and slow-twitch (B) fibre bundles across all age groups at the final contraction of the fatigue protocol (P_{60}/P_0). (A) Averaged normalised specific force data at contraction 60 (end-FP) shows the significant decrease in force produced by VCP$^{R155H/+}$ fast-twitch fibre bundles at 12 and 14 months when compared with WT controls. (B) Slow-twitch fibre bundles from VCP$^{R155H/+}$ performed similarly to WT age-matched controls in all groups, suggesting that the fatigue intolerance observed is unique to fast-twitch muscles.

3.2.3. Post-FP recovery to P_0 is significantly longer in fast-twitch muscle fibre bundles from VCP[R155H/+] at specific ages

After the end of the fatigue protocol, the stimulation rate was returned to the pre-FP rate of 1 every 90 seconds and the fibres were allowed to recover until their peak force reached ≥90% of P_0. At 6 months of age (Group 1), there were no significant differences in the peak force (Figure 3.1, A) or the post-FP recovery time (Figure 3.6, A) of wild-type and VCP[R155H/+] fast-twitch fibres. This was to be expected as there were no significant differences in the rate or degree of fatigue of these fibres either (Figure 3.1, A). At 14 months (Group 3), there was a loss of fatigue resistance (Figure 3.3, C and D) and the peak tetanic contraction force generated during the recovery period remained significantly lower than WT for most of the recovery period (Figure 3.6, C). This shift towards a lengthening of the average recovery time for VCP[R155H/+] fast-twitch fibre bundles at this age is shown in Figure 3.6 E. Again, it should be noted that for Group 3, the VCP[R155H/+] data represent only the fibres that recovered to ≥90% of P_0 post-FP.

At 27 months of age (Group 4), in a manner similar to the fatigue protocol results, there was no significant difference between WT and VCP[R155H/+] in terms of the rate of recovery to ≥90% P_0 (Figure 3.6D) or average recovery time (Figure 3.6E). Slow-twitch fibre bundles from the soleus did not show any differences in average specific force (Figure 3.2, A-D), average normalised force (Figure 3.4, A-D) or post-FP recovery time (Figure 3.7, A-D).
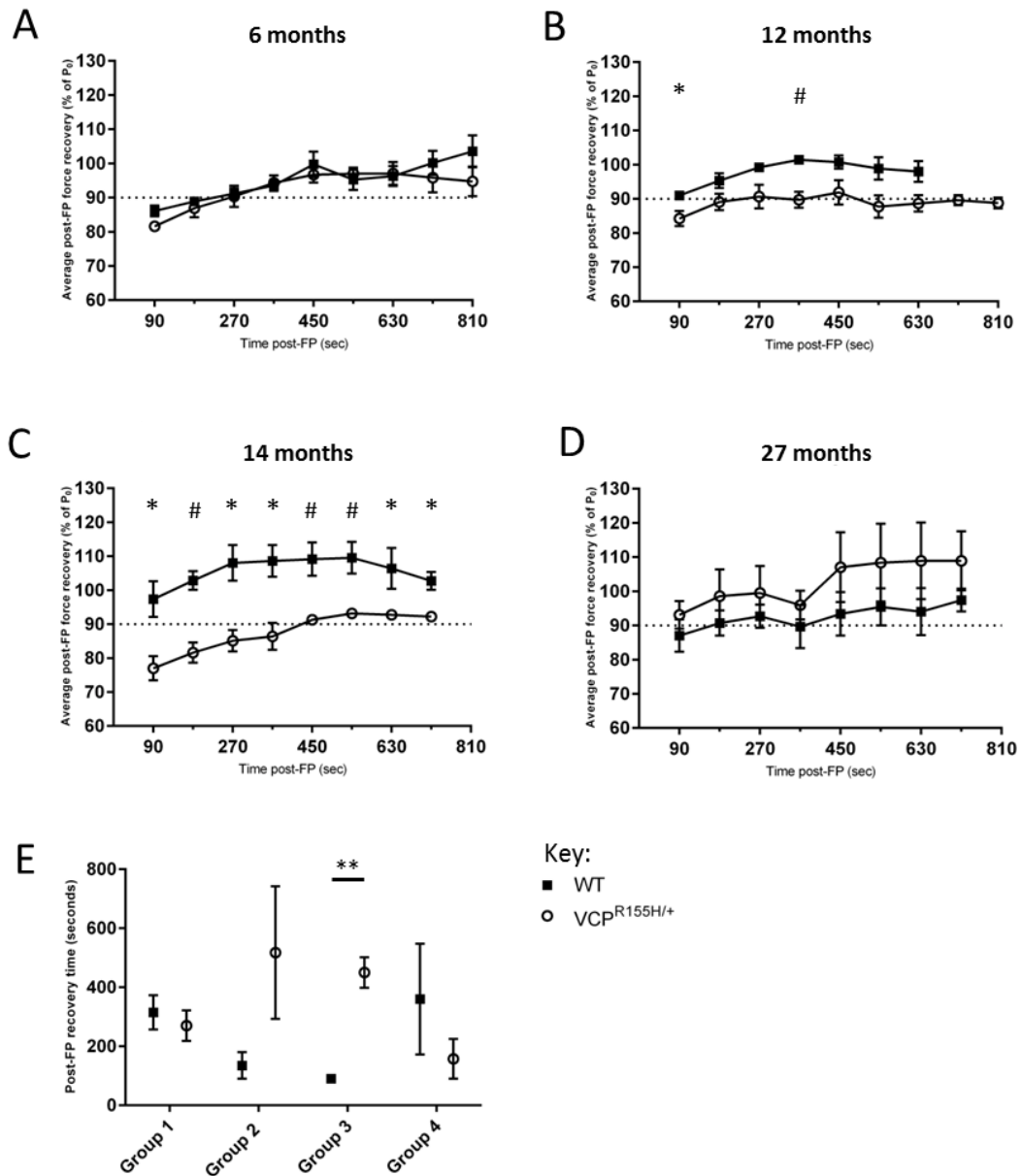
Figure 3.6 Fast-twitch fibre recovery from fatigue was significantly delayed in aged mutant mouse. Average normalised force (P/P$_0$) following fatigue protocol. Simulation rate was returned to the pre-FP non-fatiguing rate of once every 90 seconds and fibres were given 12-15 minutes to recover force. At 6 months (Group 1) WT and VCP$^{R155H/+}$ fast-twitch fibre bundles recover at the same rate post-FP. At 1 year, there is a small but significant delay in VCP$^{R155H/+}$ fibre recovery compared with WT (B). This effect becomes more pronounced at 14 months (C), with recovery to ≥90% P0 significantly delayed and normalised force significantly lower than WT. Interestingly, this pathology was not observed in fast-twitch fibre bundles from very aged mice (27 months; Group 4); WT and VCP$^{R155H/+}$ fast-twitch fibres recover from the FP similarly, with a higher average normalised force produced by VCP$^{R155H/+}$ fast-twitch fibre bundles at this age (D). The averaged fast-twitch fibre post-FP recovery times for each group are collated in E, with VCP$^{R155H/+}$ fibres taking significantly longer to recover force post-FP at 14 months when compared with WT controls (* indicates p <0.05, # indicates p<0.01, ** indicates p<0.001) (Note: graphs represent data from at least 3 different mice for each condition; n≥3 fibre bundles for each condition).
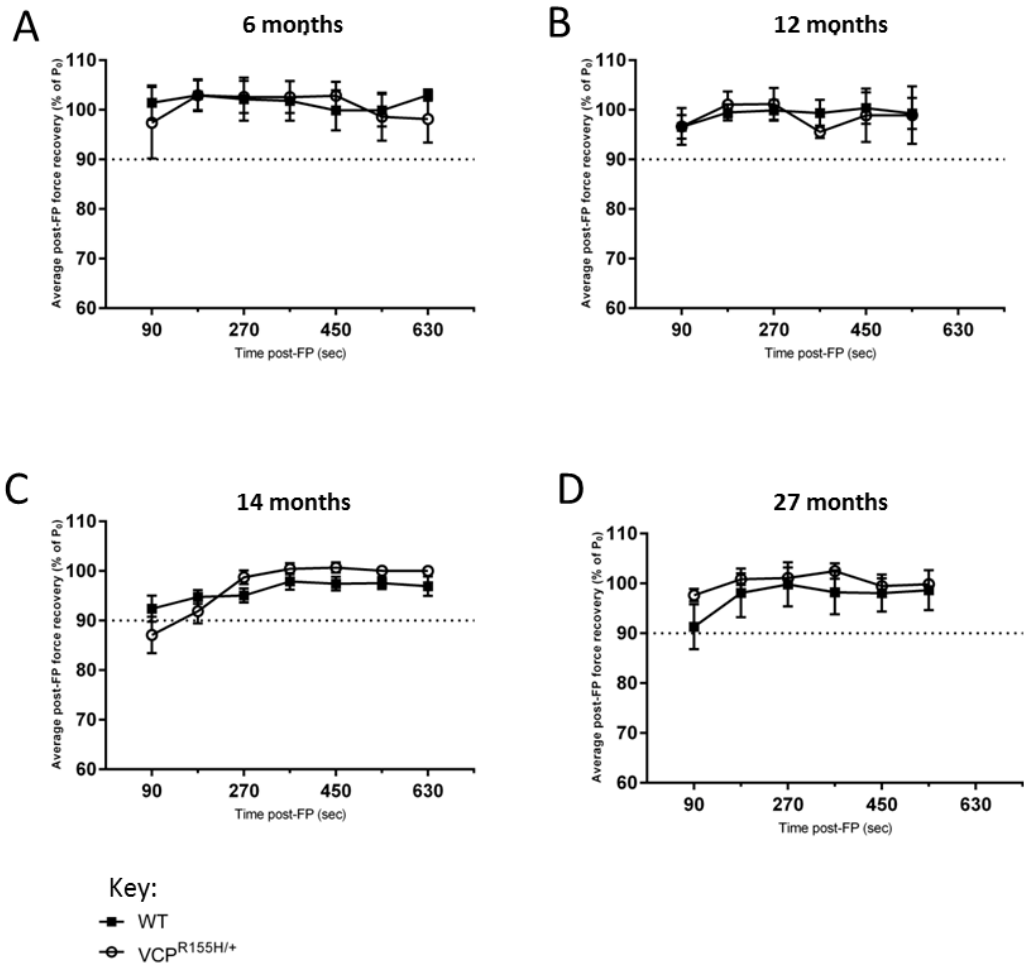
Figure 3.7 No difference in rate of post-FP recovery of slow-twitch fibre bundles from VCP[R155H/+] mice in any age group. Average normalised force (P/P$_0$) produced by age-matched WT and VCP[R155H/+] slow-twitch fibre bundles following the fatigue protocol. Simulation rate was returned to the pre-FP non-fatiguing rate of 1/90seconds and fibres were stimulated at this rate for 12-15 minutes to allow force recovery as for fast-twitch fibre bundles. No significant differences were observed in the average rate of recovery between WT and VCP[R155H/+] slow-twitch fibre bundles in any age group, suggesting that the impaired post-FP recovery is an age-specific characteristic of fast-twitch fibres from VCP[R155H/+] mice.

3.2.4. Analysis of fibre type distribution in fast-twitch muscles from 12 and 14 month old WT and VCP$^{R155H/+}$ mice

As previously outlined, the EDL muscle is categorised as a fast-twitch muscle capable of short contractile bursts before exhibiting fatigue. This categorisation is largely due to the primary energy metabolism of fast-twitch skeletal muscle (Allen *et al.*, 2008). Large differences exist between skeletal muscle fibre types regarding their glycolytic versus oxidative capacity, such as resistance to fatigue or speed of contraction.

With this in mind, it was important for us to determine the oxidative versus glycolytic fibre ratio in fast-twitch muscles from age-matched WT and VCP$^{R155H/+}$ mice, based on our observations of fibre type-specific age-dependent fatigue intolerance. We chose to examine the fibre type composition of fast-twitch muscles of mice aged 12 and 14 months, deemed the 'critical ages' for the onset of VCP-related myopathic dysfunction. To do this, we sectioned cryopreserved mouse hind limbs into 10μm thick slices using a microtome. These sections were immunostained, using either a monoclonal antibody raised against MHC-IIB, to identify fast glycolytic fibres, or a rabbit polyclonal antibody against cytochrome c oxidase subunit IV (COX-IV), to identify fast oxidative fibres. COX-IV is one of the 13 subunits of cytochrome c oxidase, which is the terminal complex in the electron transport chain (ETC) in mitochondria (Li *et al.*, 2006).

In order to demarcate the basement membrane for analysis of the fibre area, we used a rabbit anti-Nidogen-1 antibody in conjunction with the mouse anti-MHC-IIB antibody. We proceeded to image the entire EDL muscle and used ImageJ software to assign a unique number to each fibre based on the red channel (Nidogen-1 stain). Fibres were visually recorded as MHC-IIB-positive when strong staining was observed. In some sections, where part of the tissue had been damaged by the blade or the slice had partially folded back on itself, only fully visible fibres were included in the analysis. In order to identify fast-oxidative fibres, the corresponding fibres on COX-IV-immunostained serial sections were found and categorised as fast-oxidative when strong COX-IV staining was seen. Fibres were classified as intermediate (fast-oxidative glycolytic) when faint COX-IV and MHC-IIB staining was observed in the same fibre in serial sections. The relative abundance of fibre types in EDL from 12 and 14 month old WT and VCP$^{R155H/+}$ mice was determined and expressed as a ratio of the total number of fibres analysed per EDL (Figure 3.8 B and 3.9 B, respectively).

No significant differences were found in the relative frequency of each fibre type between WT and VCP$^{R155H/+}$ at 12 or 14 months of age (Figures 3.8 B and 3.9 B, respectively). At 14 months of age, VCP$^{R155H/+}$ EDL was comprised of 57.6±4.2% fast-glycolytic fibres compared with 49.2±1.8% in WT EDL. This difference in fibre type distribution however was not statistically significant. Based on COX-IV immunostaining, VCP$^{R155H/+}$ EDL contained 35.2±8.3% fast-oxidative fibres, with WT EDL containing 45.3±3.4%. Intermediate fibres, which co-stained for both COX-IV and MHC-IIB, made up 5.5±1.9% of total EDL muscle area in WT and 7.3±4.1% in VCP$^{R155H/+}$. A slight shift towards a more glycolytic fibre type in VCP$^{R155H/+}$ mice is seen at 14 months of age when compared with WT, however this is not significant when compared statistically.
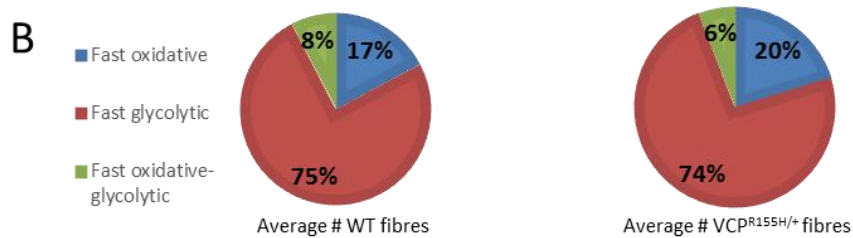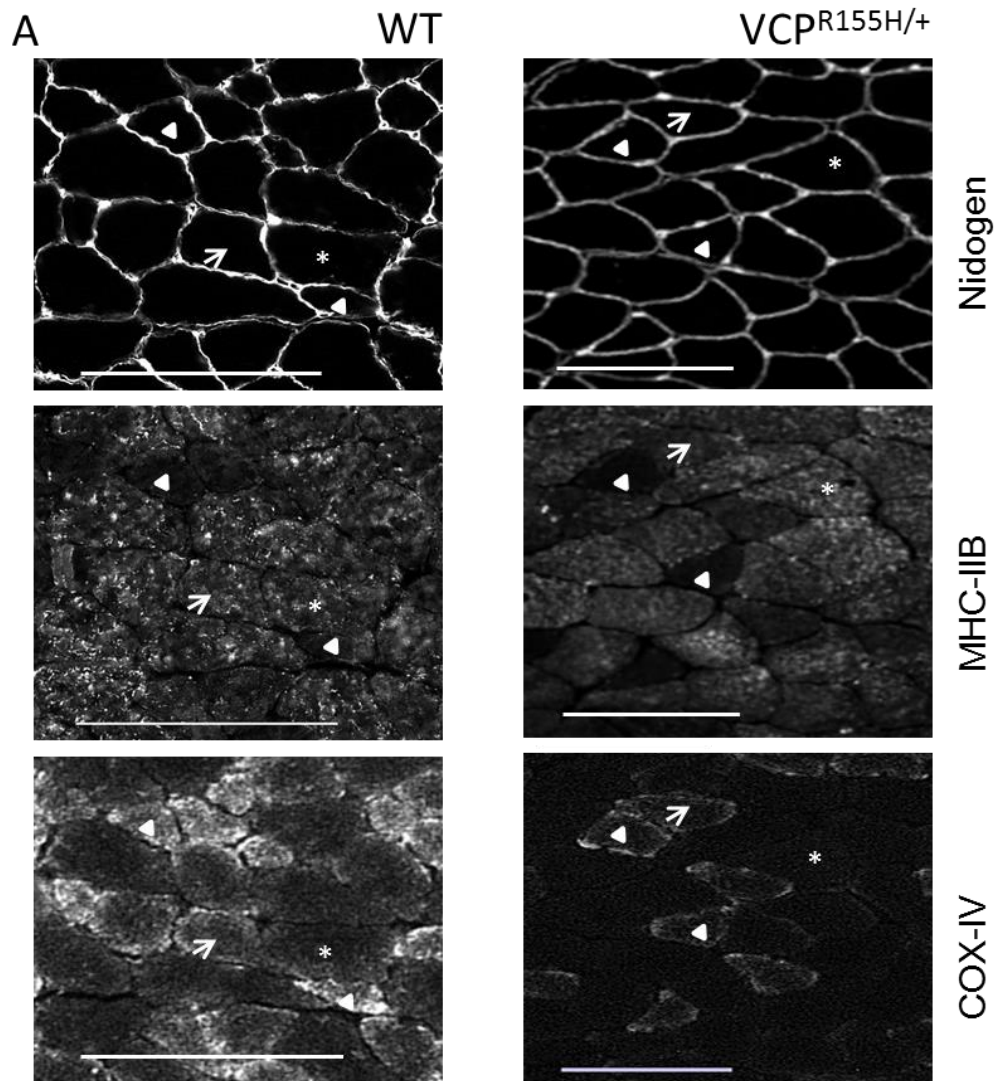
Figure 3.8 Fibre type distribution in EDL in WT and VCP^R155H/+ mice is not significantly different at 12 months of age. (A) Fast glycolytic, fast oxidative and intermediate fast oxidative-glycolytic fibres were identified by immunostaining 10μm thick cryosections of whole hind limbs from Group 2 WT (left) and VCP^R155H/+ (right) mice with antibodies against MHC-IIB and the mitochondria-specific protein COX-IV (A; scale bar = 100um). Fibres were classified as fast glycolytic when strong MHC-IIB staining was observed (asterisk); fast oxidative when strong COX-IV staining was seen (white arrow) and intermediate when both stains were observed in the same fibre (white arrow head) (B) ImageJ software was used to analyse the area of EDL fibres (average fibres counted per EDL: 684) and no significant differences were found in fibre type composition between WT and VCP^R155H/+ mutant mice at 12 months of age. (Three different animals were used for both WT and VCP^R155H/+).
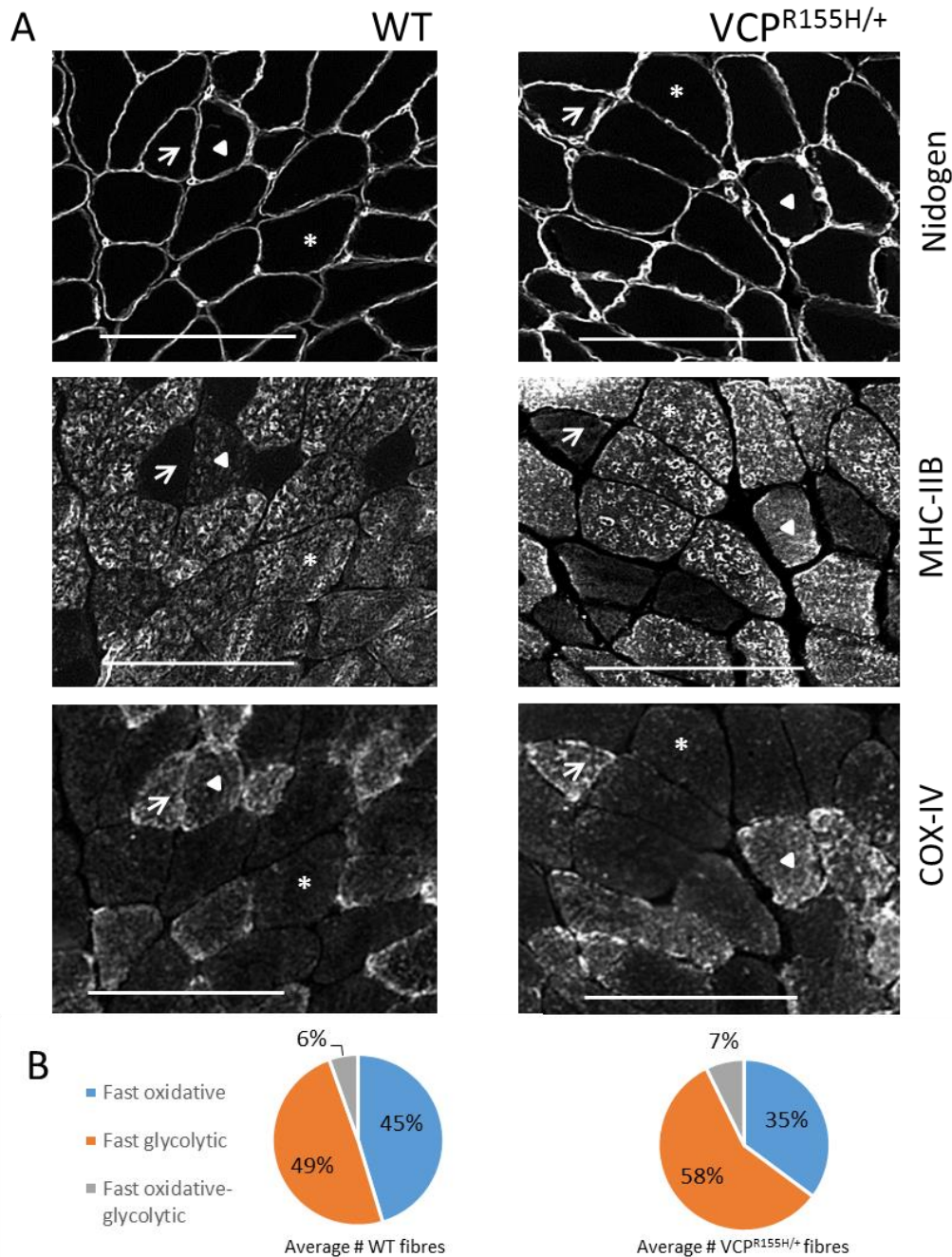
Figure 3.9 Fibre type distribution in EDL in WT and VCP^R155H/+ mutant mice is not significantly different at 14 months of age. (A) Fast glycolytic, fast oxidative and intermediate fast oxidative-glycolytic fibres were identified by immunostaining 10μm thick cryosections of whole hind limbs from Group 3 WT and VCP mice with antibodies against MHC-IIB and the mitochondria-specific protein COX-IV (A; scale bar = 100μm). An anti-nidogen antibody was used to identify the basement membrane around each fibre. Fibres were classified as fast glycolytic when strong MHC-IIB staining was observed (asterisk); fast oxidative when strong COX-IV staining was seen (white arrow) and intermediate when both stains were observed in the same fibre (white arrow head) (B) ImageJ software was used to analyse the area of EDL fibres (average fibres counted per EDL: 643) and no significant difference was found in the frequency of the three fibre types between WT and VCP mutant mice at 14 months of age.

3.2.5 Significant differences found in fibre size in 12 and 14 month old VCP$^{R155H/+}$mice when compared with WT control

After designating fibres types in EDL and finding no significant differences in the ratio of the three fibre types between WT and VCP$^{R155H/+}$ mice at 12 and 14 months, we next chose to investigate whether the sizes of each fibre type in EDL were different between the two genotypes. This would give a more comprehensive picture of the total space occupied by each fibre type in the muscle. An inverse relationship exists between fibre thickness and aerobic oxidative capacity/mitochondrial content (Schiaffino and Reggiani, 2011).

We compared the distribution of sizes of COX-IV positive fibres in WT and VCP$^{R155H/+}$ EDL from 12 (Group 2) and 14 (Group 3) month old mice and identified significant differences in the areas of specific fibre types (Figure 3.10). At 12 months, EDL muscle from VCP$^{R155H/+}$ mice contained significantly larger COX-IV/fast-oxidative fibres and MHC-IIB/fast-glycolytic fibres than those in WT controls (Mann-Whitney comparison, $p < 0.0001$). At 14 months (Group 3), the COX-IV-positive and intermediate fibres in VCP$^{R155H/+}$ were significantly larger than those in age-matched WT EDL (Mann-Whitney test, $p<0.0001$).
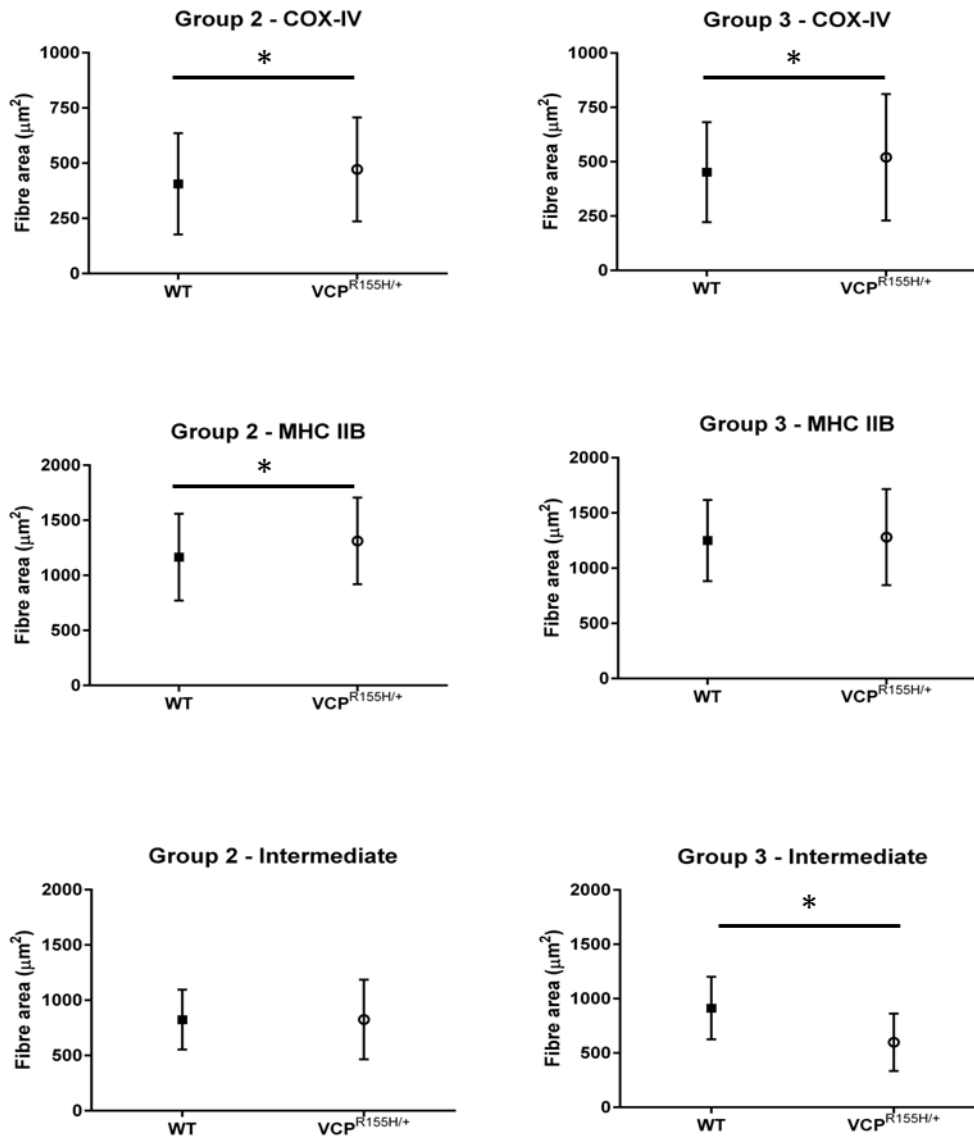
Figure 3.10 Differences between areas of specific fibre types in EDL from age-matched WT and VCP[R155H/+]. Serial cryosections of EDL were immunostained in order to determine fibre type and oxidative capacity. Fibre types were assigned manually based on immunostaining, with fibres being classified as fast glycolytic when strong MHC-IIB staining was observed ; fast oxidative when strong COX-IV staining was seen and intermediate when both stains were observed in the same fibre. An anti-Nidogen antibody stained the basement membrane and ImageJ software was used to analyse fibre area (in μm^2) based on the Nidogen stain. The range of areas from three WT and three VCP[R155H/+] EDLs was compared using a Mann-Whitney test. At 1 year (Group 2), both COX-IV-positive and MHC-IIB-positive fibres were significantly larger in VCP[R155H/+] EDL ($p < 0.0001$ in both fibre types). The range of areas of intermediate or fast-oxidative-glycolytic fibres was not significantly different at 1 year of age between WT and VCP[R155H/+] EDL. At 14 months (Group 3), the COX-IV-positive and intermediate fibres in VCP[R155H/+] were significantly larger than those in age-matched WT EDL (n=3 for both; $p < 0.0001$). Solid squares represent WT mean values ±SD and open circles represent VCP[R155H/+] ±SD.

3.2.6 Analysis of oxidative capacity and mitochondrial content of fast-twitch muscles from age-matched WT and VCP[R155H/+] mice

The next logical step in our analysis of the metabolic profiles of fast-twitch muscle from VCP[R155H/+] mice was to examine some of the biochemical properties of the tissue. Citrate synthase (CS) is a key regulatory enzyme which catalyses the primary step of the tricarboxylic acid (TCA) cycle – the condensation reaction between acetyl coenzyme A (acetyl CoA) and the four-carbon oxaloacetate (OAA) - resulting in the formation of six-carbon citric acid or citrate (Lyons *et al.*, 2002). The enzyme itself is located within the mitochondrial matrix. CS activity is routinely used as a semi-quantitative marker of oxidative and respiratory capacity and mitochondrial content (Stump *et al.*, 2003, Delp *et al.*, 1996, Lyons *et al.*, 2006), therefore we chose to investigate whether the enzyme activity of CS in fast-twitch muscles was altered as a consequence of VCP[R155H/+] expression. As with the fibre type distribution analysis, we chose to focus our investigations on the age groups in which fatigue intolerance was observed in the biomechanics experiments, i.e Group 2 (12 months) and Group 3 (14 months).

The assay is based on the CS-catalysed reaction between acetyl CoA and OAA, whereby two carbons are contributed by acetyl CoA to the four carbon OAA, resulting in a six-carbon citrate.

$$\text{Acetyl CoA} + \text{Oxaloacetate} \rightarrow \text{Citrate} + \text{CoA-SH} + H^+ + H_2O$$
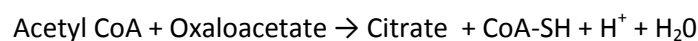
The hydrolysis of the thioester of acetyl CoA results in the addition of a thiol group to acetyl CoA (CoA-SH). This thiol group reacts with 5,5'-dithiobis-2-nitrobenzoic acid (DTNB) in the reaction mixture to form the yellow product 5-thio-2nitrobenzoic acid (TNB). The absorbance of TNB is measured spectrophotometrically at 412nm and is an indicator of CoA-SH production (Sigma Aldrich product information sheet).

$$\text{CoA-SH} + \text{DTNB} \rightarrow \text{TNB} + \text{CoA-S-S-TNB}$$

After recording endogenous thiol and deacetylase activity over an 80 second period, we initiated the reaction by adding 10μM OAA to each well simultaneously. Again, we recorded TNB absorbance at 412nm at 10 second intervals for a total of 80 seconds. The endogenous enzyme activity was subtracted from the total CS activity following the OAA

addition, giving us the net CS activity. Each condition was tested in triplicate for n=4 in Group 2 and n=3 in Group 3.

We found that at 12 months of age, the rate of conversion of DTNB to TNB by CS in fast-twitch muscle did not differ between WT and VCP$^{R155H/+}$ (Figure 3.11, C). However, at 14 months, the temporal development of TNB was slower in fast-twitch muscle from VCP$^{R155H/+}$ mice (Figure 3.11, D). We then calculated the enzyme activity, in µmoles/ml/min, and compared the averages of each condition for the two age groups using a two-tailed independent t-test. The results are represented in Figure 3.11, E.
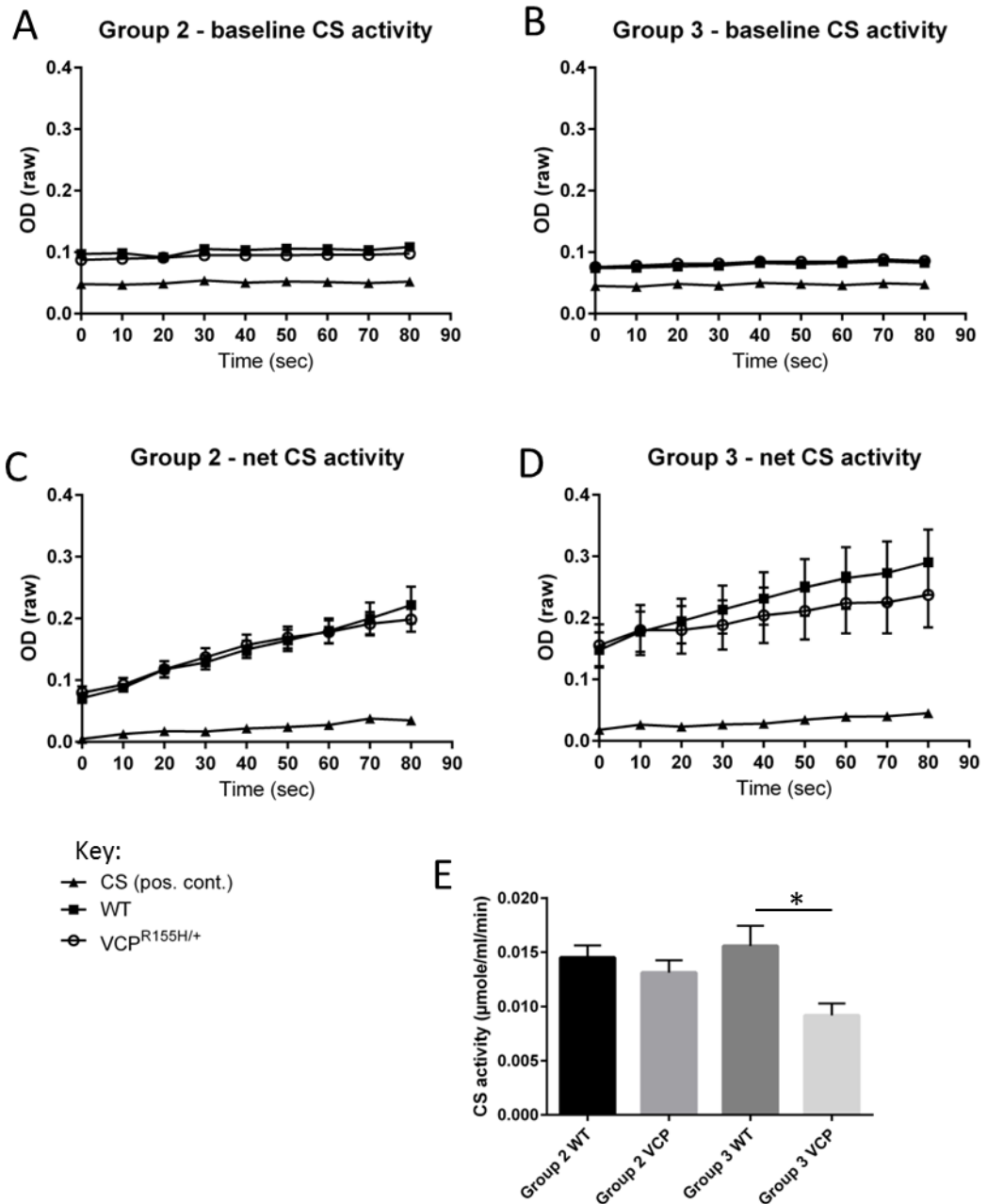
Figure 3.11 Mitochondrial respiratory complex enzyme activity in fast-twitch muscle from age-matched WT and VCP^R155H/+ mice. EDL lysates were assayed for citrate synthase (CS) activity to compare aerobic capacity of fast-twitch muscles from age-matched WT and VCP^R155H/+. Baseline CS activity was assayed in order to measure and eliminate endogenous thiol and deacetylase activity from the assay (A and B). Following the addition of the substrate 10mM oxaloacetate solution, the absorbance at 412nm was read by a plate reader every 10 seconds for 80 seconds and the baseline CS activity was subtracted from the total CS activity in order to calculate the net CS activity (C and D). At 14 months (Group 3), the CS activity (as measured in μmole/min/ml) was found to be lower in VCP^R155H/+ EDL, suggesting decreased mitochondrial function at 14 months in VCP^R155H/+ fast muscle when compared with WT control (E). This difference was not found to be statistically significant (n=4 in Group 2, n=3 in Group 3). Asterisk indicates p<0.05.

CS activity, at 14 months of age, was significantly lower in VCP$^{R155H/+}$ fast-twitch muscle when compared with WT (p=0.0418). This may indicate the presence of a defect in the oxidative pathways of fast-twitch skeletal muscle of VCP$^{R155H/+}$ mice, which presents at the previously outlined 'critical' age of 14 months. It is worth noting that, while the p-value given by the student's t-test is valid, this result cannot be overstated due to the small sample size.

To verify that the difference in CS enzyme activity was not due to lower mitochondrial content in VCP$^{R155H/+}$ fast-twitch fibres, we quantified the expression of the outer mitochondrial membrane translocase TOMM20 using Western blotting and the Odyssey Infrared Imaging system (Licor) (Figure 3.12). There were no significant differences in TOMM20 expression between WT and VCP$^{R155H/+}$ in either Group 2 or Group 3, confirming that the mitochondrial content was the same in these tissues (Figure 3.12).
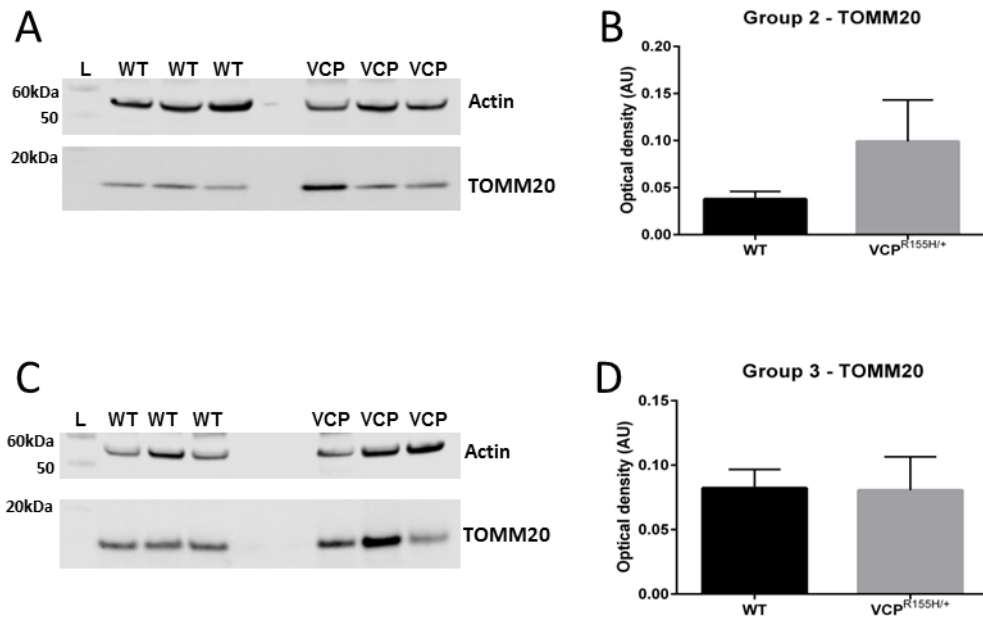
Figure 3.12 No significant difference in mitochondrial protein expression in fast-twitch muscle (EDL) between WT and VCP$^{R155H/+}$ in Groups 2 and 3. Lysates of EDL from Groups 2 (A) and 3 (C) were analysed by Western blotting to determine total mitochondrial content using an antibody against the outer mitochondrial membrane translocase TOMM20. No significant differences in TOMM20 expression were observed between WT and VCP$^{R155H/+}$ fast muscle samples from any of the three groups. Samples were run in biological triplicate.

3.3 Discussion

The predominant pathophysiological symptom of IBMPFD is late-onset progressive muscle weakness and degeneration. In order to investigate whether VCP mutation affects skeletal muscle in a fibre-specific manner, we subjected fast- and slow-twitch muscle fibre bundles to a fatigue protocol, and assessed any changes in specific force production and fatigue tolerance (Figure 3.1 and 3.3, A-E).

At 5.5 – 6.5 months of age (Group 1), there was no apparent difference between $VCP^{R155H/+}$ mutant and wild type mice with regard to the actual specific force produced by fast-twitch fibres when the values are normalised to P_0. However, as the mice approach one year of age, the normalised specific force produced by $VCP^{R155H/+}$ mutant fast-twitch fibres decreases significantly from contraction 40 onwards, and the post-FP recovery time is significantly longer than in the wild type. Interestingly, this decline becomes more pronounced at 14 months (Group 3; Figure 3.3, C and D), suggesting that fast-twitch fibres from $VCP^{R155H/+}$ mice are significantly more susceptible to fatigue-related force decline than wild type age-matched control fibres. An important point to note is that in Group 3, 75% of all $VCP^{R155H/+}$ fast-twitch muscle fibre bundles tested did not recover to $\geq 90\%$ P_0. This was the parameter used to distinguish between decreases in force production due to $VCP^{R155H/+}$ mutation and fibres that were dying during the fatigue protocol. This high proportion of 'non-recovered' fibres suggests that this is the critical age at which the functional biomechanical effects of $VCP^{R155H/+}$ mutation on fast-twitch muscle are most severe.

In contrast to the apparent functional consequences of $VCP^{R155H/+}$ expression on normalised specific force production by fast-twitch fibres, there appeared to be minimal effects of $VCP^{R155H/+}$ mutation on slow-twitch fibre fatigue characteristics. Fatigue in this case is defined as any reversible decrease in peak force resulting from the repeated tetanic stimulation of muscle. When normalised to P_0, a decrease in normalised force production and fatigue tolerance in $VCP^{R155H/+}$ mutant slow fibres can be seen from 13.2 – 14.8 months of age (Group 3) onwards, however this was not found to be significant when the $VCP^{R155H/+}$ mutant and wild type results were compared using an ANOVA (p = 0.199; Figure 3.4, C).

As previously outlined, the soleus muscle contains primarily oxidative muscle fibres. This fibre type expresses the MHC type I and IIA isoforms, utilizes the oxidative phosphorylation pathway as its main energy source and is rich in mitochondria in order to facilitate this. The MHC isoform expressed in a muscle fibre correlates directly with the speed at which the muscle contracts, as the ATP hydrolysis rate determines the speed of cross-bridge cycling and therefore sarcomere-shortening (Floeter *et al.*, 2010). Fatigue resistance is a characteristic which results from the oxidative respiration used by slow fibres; therefore sustained submaximal contractions under aerobic conditions represent a key biomechanical function of this fibre type. In contrast, type II or fast-twitch fibres contain glycolytic enzymes which produce the majority of ATP used for muscle contraction; however, the reliance on glycogen stores, which become depleted following repetitive muscle stimulation, means that these fibres are susceptible to fatigue at varying levels, depending on MHC isoform expression. Type IIA fibres are the most fatigue resistant fast fibres, type IIB are the least resistant to fatigue and type IIX are classified as intermediate.

Our results led us to examine the fibre-type composition of the fast-twitch muscles from age-matched WT and VCP$^{R155H/+}$ mice. Firstly, all fibres in EDL were found to be fast-twitch when MHC-F and MHC-S antibodies were used on sequential cryosections (Figure S.5, supplementary data). To further investigate the composition of the muscle, we used antibodies raised against the fast-glycolytic fibre subtype MHC-IIB and cytochrome c oxidase subunit IV (COX-IV), the terminal complex of the electron transfer chain in mitochondria. Fibres which immunostained positively with the MHC-IIB antibody were classified as fast-glycolytic (FG), the fibres which stained with the COX-IV antibody and therefore displayed high mitochondrial content were classified as fast-oxidative (FO) and finally fibres in which faint COX-IV staining was observed along with MHC-IIB immunoreactivity were considered intermediate or fast-oxidative-glycolytic (FOG).

The three fibre types were counted and the ratio in which they were found in EDL from age-matched WT and VCP$^{R155H/+}$ was determined and compared. This allowed us to determine any differences in the MHC isoform expression and therefore the metabolic profiles of VCP$^{R155H/+}$ fast-twitch muscles, which might explain the fatigue intolerance. Previous studies have reported a marked variation in muscle fibre size in quadriceps (mixed MHC isoform expression) from patients expressing VCP mutations (Watts *et al.*, 2007), with atrophy reported in type I fibres in several cases (Stojkovic *et al.*, 2009). It was therefore

important for us to investigate whether our VCP$^{R155H/+}$ knock-in mouse model exhibited similarities with regard to fibre size distribution and relative fibre type ratio in EDL.

No significant differences between fibre type ratio and EDL composition were revealed following visual scoring and analysis of cryosections from 12 and 14 month old WT and VCP$^{R155H/+}$ mouse hind limbs (Figures 3.8 and 3.9). The fibre type ratios in EDL from both WT and VCP$^{R155H/+}$ mice at 12 months were comparable to those in previous studies (Augusto *et al.*, 2004). At 14 months, the ratio of fast oxidative fibres (type IIA) increases in both WT and VCP$^{R155H/+}$ EDL. This trend is surprising, as the fatigue tolerance of fast-twitch fibre bundles at this age was significantly lower in VCP$^{R155H/+}$ mice. A fast-to-slow fibre type shift is associated with aging (Nilwik *et al.*, 2013), however two months would not be a long enough time period for this shift to occur. At 27 months, fast-twitch fibre bundles from VCP$^{R155H/+}$ mice performed as well as WT age-matched controls in muscle biomechanics experiments (Figure 3.3, E). Mizushima and colleagues (2004) reported a starvation-induced increase in autophagosome formation in EDL, but not in soleus, therefore fast-twitch fibres may be more susceptible to the effects of a dysfunctional autophagic pathway than slow-twitch (Mizushima *et al.*, 2004). As Ju and colleagues (2009) observed, mutations in VCP lead to the build-up of immature autophagosomes (Ju *et al.*, 2009), therefore if autophagy is activated more readily in fast-twitch fibres, autophagic dysfunction may affect fast-twitch fibres to a greater degree than slow. To that end, EDL in very aged animals (27 months) may have undergone a glycolytic-to-oxidative fibre type transition, as a result of both the aging process and a decrease in type II fibres. Analysis of EDL fibre type composition in very aged animals may provide insight into this hypothesis. Another possible explanation for the absence of muscle dysfunction in very aged mice may be that the myopathic phenotype resulted in the early death of those animals in which it was expressed, and therefore the animals that survived to 27 months may not have been as severely affected by this phenotype. Indeed, negative selection of the myopathic phenotype may have enabled some animals to survive until 27 months.

When fibre size distribution was compared statistically using a Mann-Whitney test, we found that the areas of both fast-glycolytic (MHC-IIB-positive) and fast-oxidative (COX-IV-positive) fibres were larger in EDL from 12 month old VCP$^{R155H/+}$ mice when compared with WT controls. At 14 months, the areas of VCP$^{R155H/+}$ fast-glycolytic and intermediate fibres was significantly larger than in WT EDL. Under normal conditions, increased muscle fibre size is accompanied by an increase in muscle strength (Frontera *et al.*, 1988). Piccirrilo

and colleagues (2012) demonstrated that *tibialis anterior* muscles which had been electroporated with plasmid encoding a dominant negative ATPase-deficient VCP mutant, VCP^{K524A}, were significantly larger than those treated with WT-VCP (Piccirillo *et al.*, 2012). However, in contrast to our work, the study did not find any significant differences in size between fibres electroporated with the IBMPFD mutant VCP-R155H plasmid and those treated with WT-VCP. The apparent hypertrophy of certain fibre types in our studies does not seem to accompany an increase in functional strength, as whole muscle studies of EDL reveal that even at 15 months of age, force production by whole EDL muscles from WT and $VCP^{R155H/+}$ mice did not differ in terms of specific force (manuscript, in progress).

The discovery that fast-twitch muscles isolated from aged $VCP^{R155H/+}$ mice fatigued to a greater degree than WT controls prompted us to investigate potential mechanisms by which the reduced fatigue resistance may be occurring. Baker *et al*. (2010) outlined the interactions between the three energy-providing metabolic systems in skeletal muscle during exercise. The energy provided by phosphocreatine (PCr) conversion spikes very early during a 100sec long bout of exercise (at around 5secs) and is seen to decrease sharply thereafter. ATP generated via glycolytic respiration peaks at around 40 seconds into the exercise, after which it gradually drops. However, ATP turnover from mitochondrial respiration only begins to peak after approximately 100 secs of exercise (Figure 3.13). Therefore, it would be reasonable to suggest that the fatigue-induced decrease in force we discovered in aged $VCP^{R155H/+}$ mice may result in part from compromised ability of the mitochondrial network to generate ATP optimally during exercise.
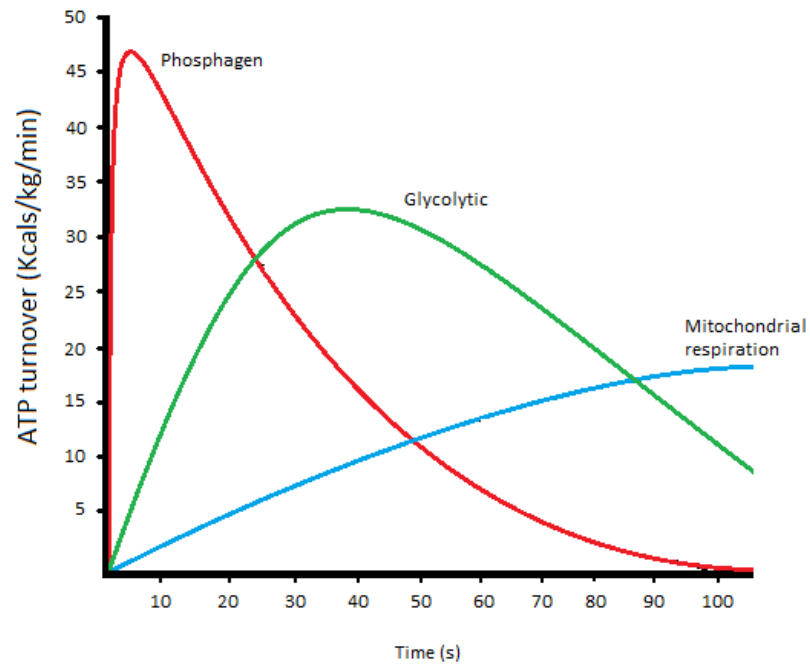
Figure 3.13 Interaction of energy systems and differences in ATP turnover rate during short-term exercise to fatigue in skeletal muscle. During the transition from rest to activity, immediate ATP regeneration is facilitated by the dephosphorylation of phosphocreatine by creatine kinase to produce ADP and P_i (red line). Longer term contractile activity is supported by ATP generation via oxidative phosphorylation in mitochondria; a process which is more effective in slow-twitch muscles due to the higher mitochondrial content (blue line). Intermediate energy requirements are met via glycolysis (green line) (Adapted from Baker, 2010 (review)).

In order to investigate this theory, we assayed mitochondrial enzyme activity in fast-twitch muscles isolated from age-matched group 2 and 3 mice, specifically that of citrate synthase. CS is described as the pace-making enzyme for the TCA cycle, in which it catalyses the condensation reaction between acetyl coenzyme A (acetyl CoA) and oxaloacetic acid (OAA) to form citric acid. Maximal CS activity is routinely used as a marker of aerobic capacity and mitochondrial density in skeletal muscle (Stump *et al.*, 2003, Delp *et al.*, 1996).

Interestingly, we found lower overall CS activity in fast-twitch muscles (EDL) from VCP$^{R155H/+}$ mice aged 14 months (Group 3). This is the age at which isolated VCP$^{R155H/+}$ mutant fast-twitch fibre bundles not only fatigue to a greater extent than their WT control counterparts, but also take significantly longer to recover isometric force to ≥90% P_0 post-FP.

From these data, we propose that there is a defect in maintaining mitochondrial network integrity in VCP$^{R155H/+}$ mutant mice, which manifests pathologically in muscle at 14 months. It has been shown that VCP is involved in shuttling oxidatively-damaged mitochondrial proteins to the proteasome, so it would be reasonable to suggest that the decreased function of the mitochondrial network (as evidenced by fatigue intolerance and diminished TCA cycle function), is due to the accumulation of damage over time. Indeed, the effects of VCP mutation on the removal of damaged mitochondrial proteins are not lethal, as the mice survive to well beyond 2 years. However, failure to adequately maintain mitochondrial quality control mechanisms, via the removal and degradation of these damaged proteins, would be detrimental to the network integrity and thus the ability of the muscle fibres to resist fatigue through longer-term ATP generation. To that end, researchers have recently discovered altered mitochondrial dynamics and bioenergetics in primary fibroblasts isolated from patients harbouring the VCP-R155H mutation (Nalbandian *et al.*, 2015). Using Seahorse XF-24 flux analysis (which measures the oxygen consumption and glycolysis rates in cells *in vitro*), it was revealed that in VCP-R155H fibroblasts, ATP content and spare respiratory capacity (a measure of the extra ATP that can be produced by oxidative phosphorylation under stressful conditions) was decreased, and increased proton leak (suggestive of a decrease in mitochondrial membrane integrity) and extracellular acidification rate (ECAR; indicative of levels of glycolysis) were increased. These results provide a possible explanation for the fatigue intolerance observed in VCP$^{R155H/+}$ fast-twitch skeletal muscle our experiments. Again, it is important to note that

the muscle mechanics data obtained from the very aged mice do not support this theory. Therefore further investigations into the mechanism by which these mice either evade age-dependent muscle dysfunction or regain fast-twitch muscle functional capacity later in life are warranted.

Chapter 4: Effect of VCP mutant expression on mitochondrial dynamics *in vitro*

4.1 Introduction

In text books, mitochondria are generally depicted as solitary organelles, but now they are understood to be continually involved in fission and fusion events with one another, leading to a dynamic interconnected filamentous network. The energy status and metabolic demands of the cell initiate and dictate these changing network configurations. While the principle function of mitochondria is to maintain cellular homeostasis, their dysfunction can prove lethal to the cell, specifically via the generation of reactive oxygen species (ROS), which damage DNA and stimulate apoptosis (Campello *et al.*, 2014). Mitochondrial quality control involves the removal of damaged mitochondria from the network in order to maintain functional integrity. The selective autophagic degradation of whole mitochondria, termed mitophagy, occurs when the organelle becomes irreparably damaged (Figure 1.5). In order to segregate the single dysfunctional mitochondrion from the network, a highly-regulated protein degradation cascade occurs (Tastuda *et al.*, 2008; Chan, 2012 (review)). It is becoming evident that the degradation of these proteins and thus the molecular control of mitochondrial dynamics is governed by a ubiquitin-protein degradation pathway (Tanaka *et al.*, 2010, Kim *et al.*, 2013, Ashrafi *et al.*, 2013).

Both the inner and outer mitochondrial membranes must be divided sequentially, to prevent the matrix contents from leaking into the cytosol. Outer mitochondrial fusion proteins, such as Mfn1 and 2, are degraded by the ubiquitin-proteasome system (UPS) (Tanaka *et al.*, 2010). Such proteins become ubiquitinated by the E3 ubiquitin ligase Parkin, thus targeting them for degradation. Under homeostatic conditions, Parkin is diffusely localised in the cytosol. Loss of mitochondrial membrane potential acts as a signal to Parkin to translocate to the mitochondrial network and facilitate the removal of dysfunctional proteins via ubiquitination. Studies have demonstrated that the expression of mutated VCP prevents the proteasomal degradation of ubiquitinated Mfn1 and 2 (Kim *et al.*, 2013,

Tanaka *et al.*, 2010). The role of VCP in Parkin-dependent mitophagy is depicted in Figure 1.5.

There are two indications that mitochondria may have a role in the pathology seen in IBMPFD:

1. Swollen mitochondria have been observed in skeletal muscle of IBMPFD disease model animals by Badadani and colleagues (Badadani *et al.*, 2010)
2. The age-dependent fatigue intolerance of fast-twitch skeletal muscle fibre bundles we observed in VCP$^{R155H/+}$ mice.

This prompted us to examine the effects of mutated VCP expression on two inexorably linked characteristics of mitochondria – morphology and function.

Initially, to investigate the possible effects of overexpressing the IBMPFD-associated VCP mutant, VCP-R155H, on mitochondrial morphology, we transiently over-expressed EGFP-tagged plasmids encoding both wild type and the clinically relevant R155H-mutated VCP in MEF cells. Mitochondria were stained using MitoTracker CMXRos - a red cell-permeant mitochondrion-selective dye which diffuses passively across the plasma membrane and accumulates in active mitochondria but not inactive/defective mitochondria. The cells were incubated in 300nM MitoTracker CMXRos dye in complete DMEM and once the mitochondria were labelled (following an incubation time of 25 minutes); the cells were fixed with 4% PFA to enable further processing and visualisation.

In a complementary approach (and to overcome the limitations of transient transfections) we also isolated and cultured primary skin-derived fibroblasts from our VCP$^{R155H/+}$ knock-in mice to investigate the effects of endogenous expression of the IBMPFD-associated VCP mutation R155H on mitochondrial dynamics under both steady state and oxidative stress conditions, induced by the addition of carbonyl cyanide m-chlorophenylhydrazone (CCCP), a reversible mitochondrial uncoupling agent. Experiments were completed in biological triplicate for each condition.

4.2 Results

4.2.1.1 Transfected EGFP-tagged VCP variants are diffusely distributed in the cytosol in MEFs under control conditions

The pathologic R155H mutation did not affect the diffuse cytoplasmic localisation of VCP under control conditions. MitoTracker CMXRos was used to stain mitochondria with intact membrane potential and the filamentous networks could be clearly seen in non-transfected cells, and EGFP-tagged WT- and R155H-VCP transfected cells (Figure 4.1).

4.2.1.2 Dissipation of the mitochondrial membrane potential does not affect the cellular localisation of VCP in transfected MEF cells

Transfected MEF cells were treated for 3 hours with 50uM CCCP 24hrs post-transfection. Live mitochondria were stained using MitoTracker CMXRos. Diffuse VCP staining was observed both in cells transfected with plasmids encoding EGFP-tagged WT-VCP and VCP-R155H. No translocation of VCP to the mitochondrial network upon membrane depolarisation by CCCP was observed (Figure 4.1). Overexpression of EGFP-VCP-R155H did not affect the ability of the mitochondrial network to fragment upon CCCP treatment, as rounded MitoTracker CMXRos-positive organelles could be seen clearly in both these cells and those transfected with EGFP-tagged WT-VCP. Tanaka and colleagues (2010) reported on the CCCP-induced accumulation of endogenous wild type VCP on mitochondria in HeLa cells transiently expressing YFP-Parkin. Therefore, the failure of EGFP-tagged VCP variants to localise with uncoupled mitochondria in MEF cells in our experiments was to be expected, as MEF cells lack Parkin expression (Matsuda *et al.*, 2010, Tanaka *et al.*, 2010). These preliminary experiments confirmed the findings of previous publications (Tanaka et al., 2010). Next, we chose to further examine in detail the effects of endogenous levels of VCP-R155H on mitochondrial dynamics under homeostatic conditions and in response to oxidative stress.
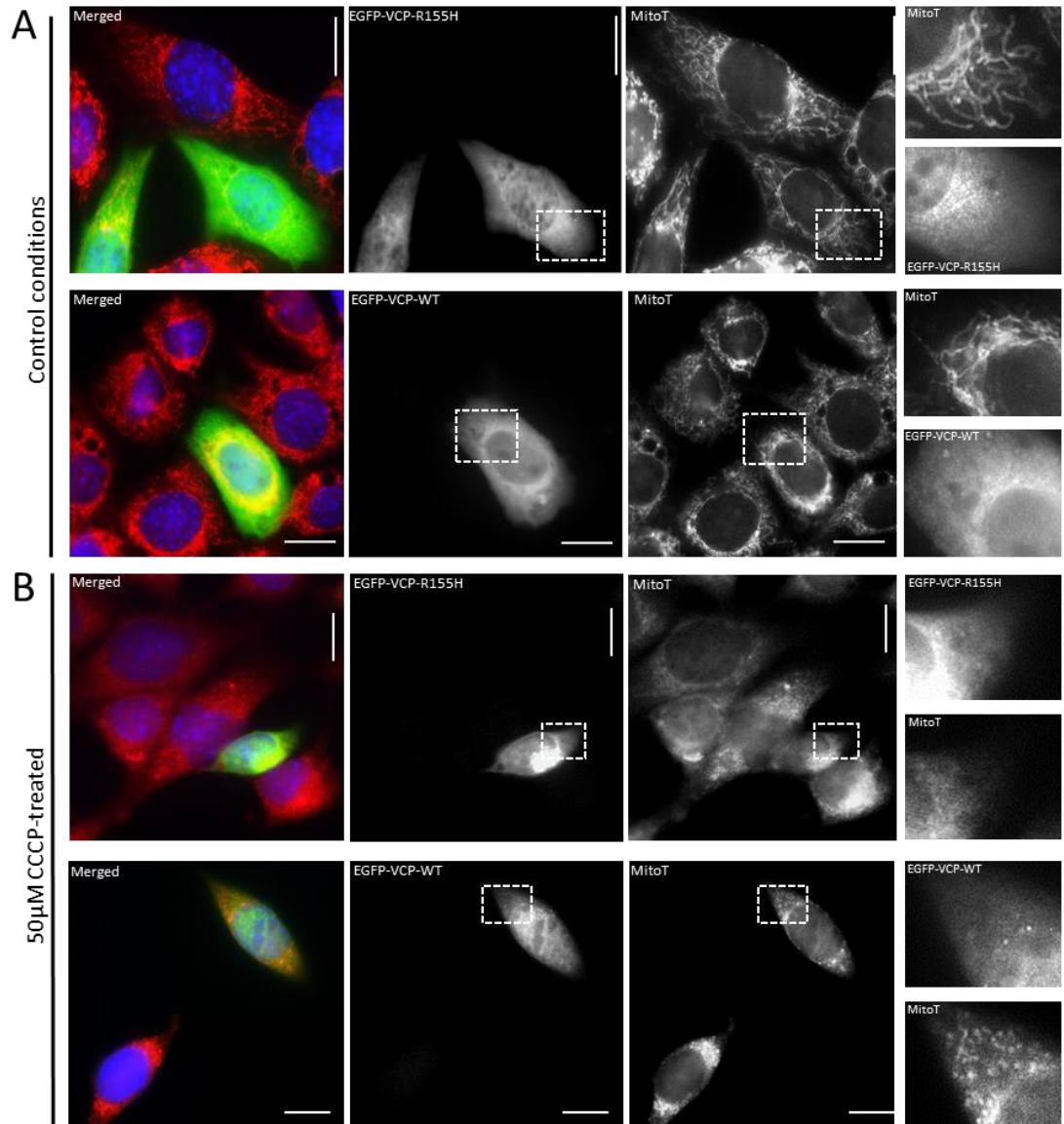
Figure 4.1 Transfected EGFP-tagged VCP variants do not colocalise with mitochondria in MEF cells under control conditions (A) nor when exposed to oxidative stress (B). (A) The pathogenic R155H mutation did not affect the diffuse cytoplasmic localisation of VCP under control conditions. MitoTracker CMXRos was used to stain mitochondria with intact membrane potential and the filamentous networks can be clearly seen in both WT and R155H-VCP transfected cells. (B) CCCP treatment did not affect the cellular localisation of VCP in MEF cells. Transfected MEF cells were treated for 3 hours with 50μM CCCP 24hrs post-transfection. Live mitochondria were stained using MitoTracker CMXRos. Diffuse VCP staining is observed both in cells transfected with EGFP-tagged WT-VCP and R155H-VCP. No translocation of VCP to the mitochondrial network upon membrane depolarisation by CCCP is seen (Scale bar = 20μm).

4.2.2.1. Similar cytosolic distribution of endogenous WT- and R155H-mutant VCP in primary skin-derived fibroblasts under steady state conditions

We next sought to investigate whether the expression of physiological levels of VCPR155H had any effect on:

(i)   The morphology of the mitochondrial network under control conditions.

(ii)   The ability of the mitochondrial network to fragment under conditions of oxidative stress.

Our knock-in animal model of IBMPFD was integral to this work – we isolated and cultured primary fibroblasts from skin biopsies of young (<3 months of age) WT and VCP$^{R155H/+}$ mice and performed immunofluorescence microscopy on the cells by immunostaining endogenous VCP with rabbit monoclonal anti-VCP antibody. As with the MEF cell transfections, MitoTracker CMXRos was used to stain mitochondria. As shown in Figure 4.2, diffuse staining of VCP was seen in the cytosol, with nuclear staining also observed in fibroblasts derived from both WT-VCP and VCP$^{R155H/+}$ mutant mice. VCP is known to play a role in piecemeal microautophagic degradation of the nucleus in yeast; therefore this localisation was not considered unusual (Krick *et al.*, 2010).

Initially, we visually scored the fibroblast cell images and classified the VCP distribution patterns in three categories – (i) diffuse, (ii) diffuse with some puncta and (iii) punctate. We also scored the mitochondrial morphology in cells as (i) tubular, (ii) fragmented (small rounded mitochondria seen) or (iii) intermediate (swollen sections within tubular mitochondria). Images were numbered randomly by a colleague and scored blindly to avoid bias. We found that both wild type VCP and VCP$^{R155H/+}$ remained diffusely distributed in the cytosol and no colocalisation of VCP with mitochondria was observed under control conditions (Figure 4.2 (A)).
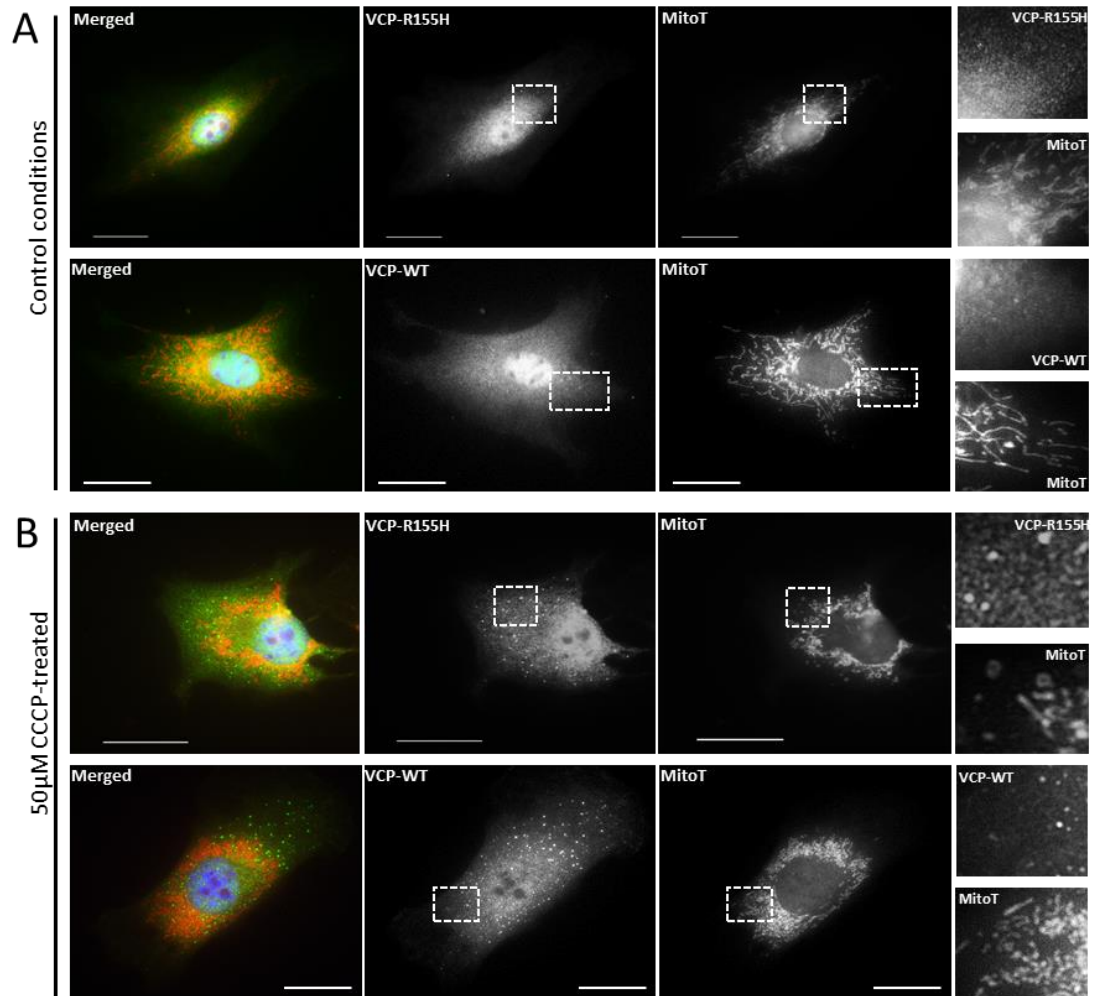
Figure 4.2 Cytoplasmic distribution of endogenous VCP in primary fibroblasts isolated from WT and VCP^R155H/+ mice under (A) control and (B) oxidative stress conditions. Endogenous VCP in primary murine fibroblasts was stained using a rabbit monoclonal anti-VCP antibody. Mitochondria were stained with MitoTracker CMXRos and nuclei stained with DAPI. (A) Note the filamentous mitochondrial network and diffuse cellular VCP staining under control conditions. (B) Following CCCP treatment, punctate VCP aggregates were observed throughout the cytoplasm, while the fragmented mitochondria clustered in the perinuclear region. VCP does not appear to colocalise with mitochondria under control nor stress conditions (insets) (Scale bar = 20μm).

4.2.2.2. Endogenous expression of pathogenic VCPR155H does not affect mitochondrial fragmentation upon CCCP treatment on visual scoring

Following CCCP treatment, the mitochondrial network fragmented in both WT-VCP and VCP$^{R155H/+}$ expressing cells (Figure 4.2(B)). Interestingly, both WT- and R155H-mutant VCP formed punctate aggregates when exposed to oxidative stress; however these puncta did not colocalise with the fragmented mitochondria (Figure 4.2 (B) insets).

Western blotting using lysates of these cells revealed low yet comparable expression of endogenous Parkin in both WT and VCP$^{R155H/+}$ primary fibroblasts (when compared with a lysate of brain from a WT mouse), again emphasising the necessity of Parkin in the translocation of VCP to mitochondria under conditions of oxidative stress (Figure 4.3). In summary, the presence of the R155H mutation in VCP neither impeded nor enhanced its colocalisation with the mitochondrial network, and the dissipation of the mitochondrial membrane potential and fragmentation of the network by CCCP treatment did not induce the translocation of VCP to mitochondria in cells with low Parkin expression (Matsuda *et al.*, 2010). Under control conditions, VCP was mainly diffusely distributed throughout the cytoplasm in both WT and VCP$^{R155H/+}$ fibroblasts (average scoring of 75% of WT cells and 68% VCP$^{R155H/+}$ cells displayed diffuse VCP staining). Following a 3 hour incubation with 50µM CCCP to induce mitochondrial uncoupling, VCP puncta were observed in both WT and VCP$^{R155H/+}$ cells (Figure 4.4). Figure 4.5 represents visual scoring of mitochondrial morphology in primary WT and VCP$^{R155H/+}$ fibroblasts under control conditions and under conditions of oxidative stress.
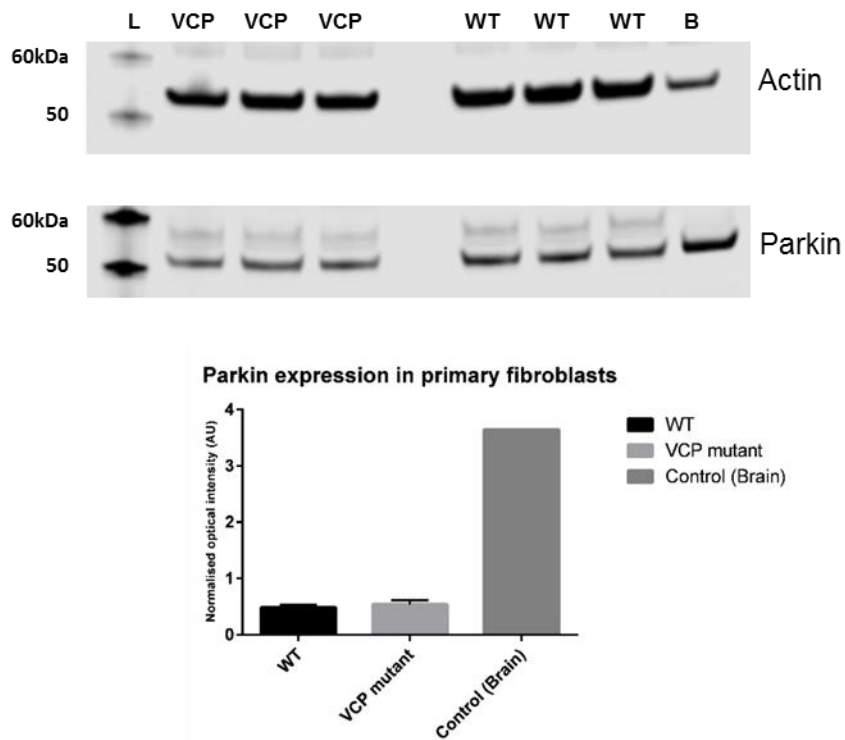
Figure 4.3 Expression of endogenous Parkin in primary WT and VCP$^{R155H/+}$ fibroblasts. Lysates of cultured primary fibroblasts from WT and VCP$^{R155H/+}$ mice were run on a 4-12% Bis-Tris precast gel (Novex) for 1hour at 120V. MagicMark XP ladder was used to determine band size. Mouse anti-actin and rabbit anti-Parkin were used to immunolabel the blot. Signal intensity was measured using LiCor Odyssey analysis software and graphed. Parkin expression was found to be lower in both WT and VCP$^{R155H/+}$ fibroblasts than in brain lysate from WT mouse (B; approximately 8-fold difference in endogenous Parkin expression) with comparable expression observed between WT and VCP$^{R155H/+}$ fibroblasts.
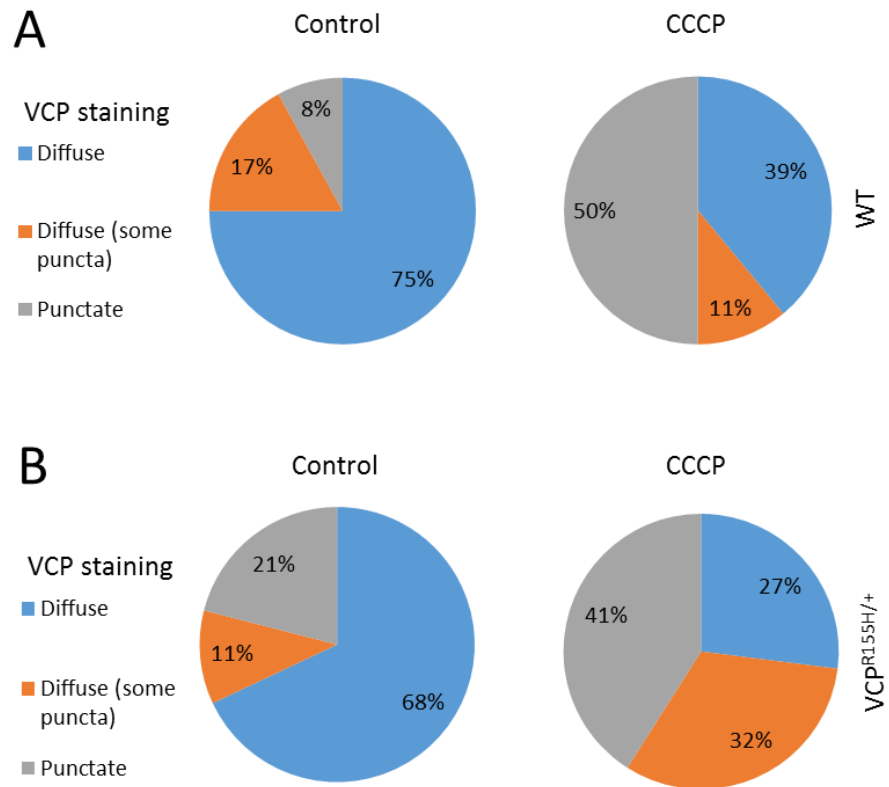
Figure 4.4 Visual scoring of endogenous cytoplasmic VCP distribution in primary (A) WT and (B) VCP$^{R155H/+}$ fibroblasts under control conditions and following exposure to oxidative stress. Under control conditions, VCP was mainly diffusely distributed throughout the cytoplasm in both WT and VCP$^{R155H/+}$ cells (average scoring of 75% of WT cells and 68% VCP$^{R155H/+}$ cells displayed diffuse VCP staining). Following 3 hour incubation with 50µM CCCP to induce mitochondrial uncoupling, VCP puncta were observed in both WT and VCP$^{R155H/+}$ cells (average number of cells scored per condition = 23).

A

Control | **CCCP**

- ■ Tubular
- ■ Fragmented
- ■ Intermediate

WT

B

Control | **CCCP**

- ■ Tubular
- ■ Fragmented
- ■ Intermediate
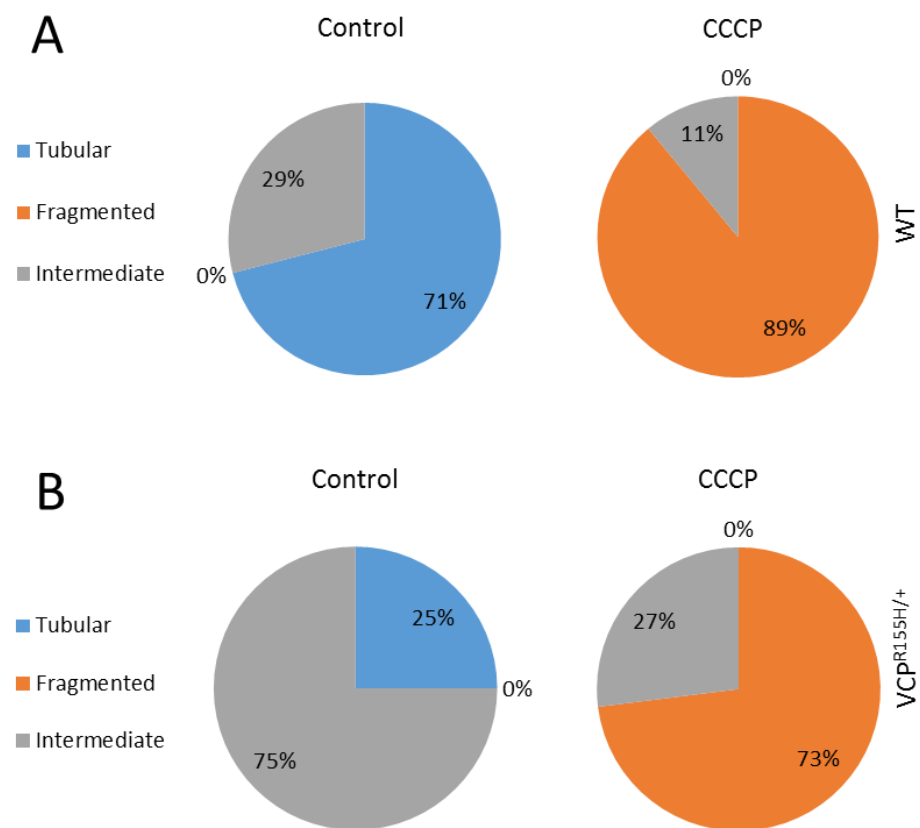
VCP$^{R155H/+}$

Figure 4.5 Expression of VCP^{R155H} does not hinder the ability of the mitochondrial network to fragment following uncoupling. Graphic representation of mitochondrial morphological conformation under control conditions and when exposed to oxidative stress. Morphology was scored visually in each cell and classified as tubular, fragmented (small rounded mitochondria) or intermediate (swollen parts within tubular mitochondria). Interestingly, while 71% of WT fibroblasts displayed a tubular network of mitochondria, the mitochondria in VCP$^{R155H/+}$ fibroblasts were classified as mainly intermediate (75% of cells scored showed intermediate mitochondrial morphology). Scoring was performed blind. (Average number of cells scored per condition = 23).

These results are in line with the observations of Tanaka and colleagues (2010), showing that in HeLa cells lacking Parkin, VCP failed to translocate to depolarised mitochondria. Interestingly, both WT-VCP and a catalytically dead VCP mutant, VCP$^{E305Q/E578Q}$, colocalised with mitochondria following CCCP treatment, indicating that ATPase activity is not required for this colocalisation. It has been demonstrated that the R155H mutant has normal ATPase activity (Weihl *et al.*, 2006), therefore we wanted to investigate, in a more quantitative way, how the expression of the R155H mutant might affect mitochondrial dynamics. We decided that spatial three-dimensional analysis of the mitochondrial networks, under both homeostatic and oxidatively stressful conditions, would be a good method of revealing any such effects.

4.2.3.1 Three dimensional analysis of mitochondrial dynamics in primary fibroblasts

In order to examine mitochondrial dynamics in the context of mutant VCP expression in the native cellular environment, we successfully isolated primary skin-derived fibroblasts from WT and VCP$^{R155H/+}$ mice. Analysis of mitochondrial morphology in a three dimensional way involved acquiring high resolution z-stacked microscope images across the depth of fixed fibroblasts in which the mitochondria were again labelled using MitoTracker CMXRos.

These images were then processed using Imaris analysis software (Bitplane), which delivers a numerical summary describing several mitochondrial characteristics of a given cell – surface area (in μm^2), volume (in μm^3) and sphericity (value between 0.0001 and 1, with the sphericity of a perfect sphere being equal to 1). A single cell was demarcated using the Region of Interest function. Intensity thresholding was used in order to accurately differentiate between true mitochondria pixels and background fluorescence (Westrate *et al.*, 2014). The thresholding of each image ensured that each image was analysed in a consistent way – enabling the standardised selection of mitochondrial objects in the cells. The software then generated a 3D rendering, or 'isosurface', of the networks, and from this rendering the characteristics of the mitochondria were deduced and exported into an Excel spreadsheet for analysis. The mitochondria were categorised into bins based on their volumes, (1-10μm^3, 11-100μm^3 and 101-1000μm^3; with mitochondrial objects smaller than 1μm^3 not considered to be true mitochondria and excluded from the analysis) and the volumes of the mitochondrial objects of 5 cells from three WT and three VCP$^{R155H/+}$ animals were compared using an ANOVA on ranks with Tukey post-hoc analysis (Figure 4.6). The analysis was blinded by denoting each cell with the identification number of the mouse from which it was derived, while the genotyping of these animals was carried out separately by another member of the lab.
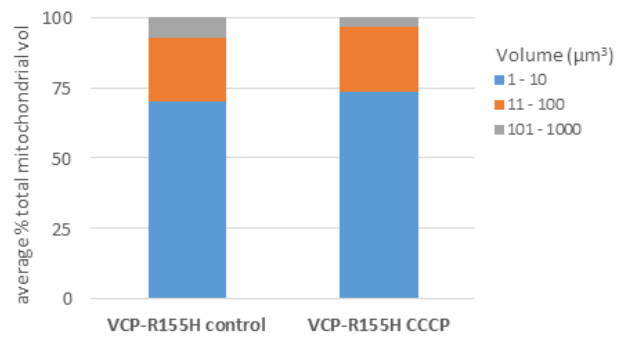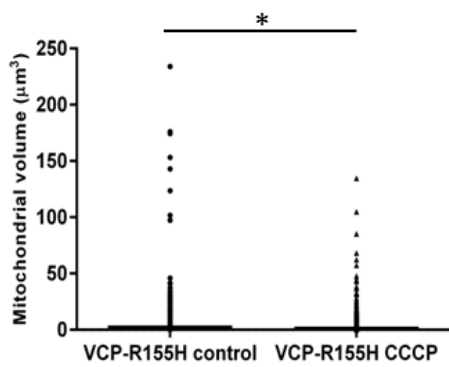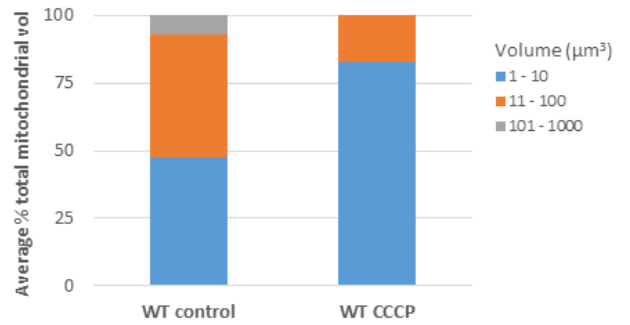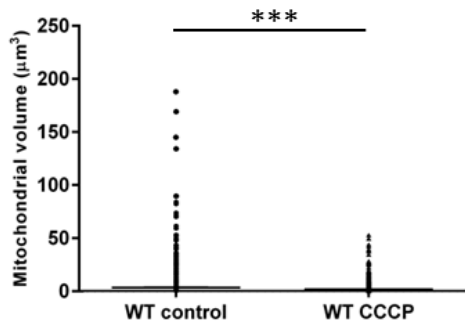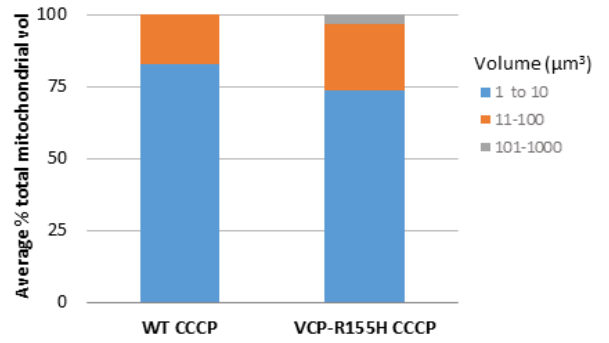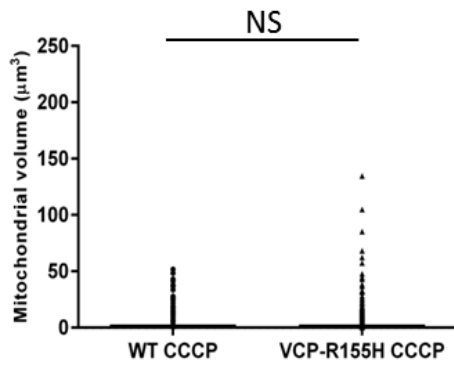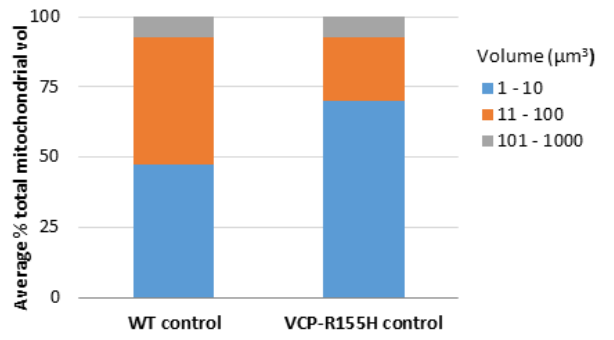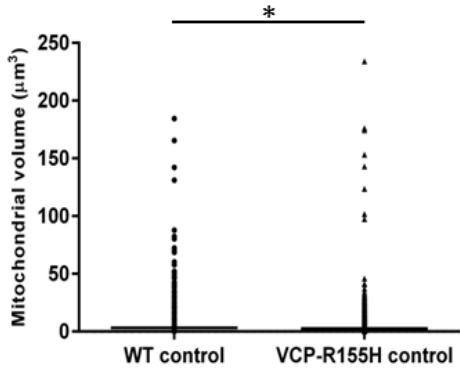
Figure 4.6 Quantitative analysis of mitochondrial volumes in primary WT and VCP$^{R155H/+}$ fibroblasts under control conditions and following 3 hour 50µM CCCP treatment. Under control conditions, the mitochondrial volumes in both WT and VCP$^{R155H/+}$ cells span a range from 1-184.4µm^3 in WT and 1-234.05µm^3 in VCP$^{R155H/+}$ cells, indicative of the continuous fission and fusion events occurring to maintain mitochondrial network quality control under steady state conditions. These volumes were found to be significantly different, even under control conditions (p=0.125; WT median volume = 1.092; VCP VCP$^{R155H/+}$ median volume = 0.9321). As expected, in WT cells a significant decrease of the mitochondrial volume range is observed following CCCP treatment (median WT control volume = 1.092µm^3 compared with 0.6434µm^3 following CCCP incubation; p<0.0001). While in VCP$^{R155H/+}$ cells, the mitochondrial network did fragment significantly following CCCP incubation (median VCP$^{R155H/+}$ control volume = 0.9321µm^3 decreased to 0.5125µm^3 after CCCP treatment; p<0.0001), several large components of the network remained, with the largest of these measuring 134.73µm^3. The significant difference in mitochondrial fragmentation is seen when comparing CCCP-treated WT and VCP fibroblasts (p<0.0001).

4.2.3.2 Comparison of mitochondrial volumes in WT and VCP[R155H+] fibroblasts under control conditions

A two-way ANOVA comparing mitochondrial volumes across the four conditions (WT, VCP[R155H/+], control and CCCP-treated) showed significant differences between genotypes and treatments. Tukey post-hoc analysis revealed significant differences in mitochondrial volumes between primary WT and VCP[R155H/+] fibroblasts under control conditions (p = 0.00125). Under control conditions, the mitochondrial volumes in WT and VCP[R155H/+] cells span a range from 1-184.4μm^3 and 1-234.05μm^3 respectively, indicative of the continuous fission and fusion events occurring to maintain mitochondrial network quality control under steady state conditions. Interestingly, statistical analysis showed these volume ranges to be significantly different (p=0.00125), with the median volume in WT fibroblasts measuring 1.092μm^3 (n = 3725) and 0.9321 μm^3 in VCP[R155H/+] fibroblasts (n = 4011).

4.2.3.3 CCCP treatment induced fragmentation of the mitochondrial networks to a greater extent in primary WT fibroblasts when compared with VCP[R155H/+] cells

As expected, in WT-VCP expressing fibroblasts, the mitochondrial network fragmented following dissipation of the membrane potential by CCCP incubation, as indicated by the significant decrease of the mitochondrial volume range (median WT control volume = 1.092μm^3 compared with 0.6434μm^3 following CCCP incubation; p<0.0001). While the mitochondrial network did fragment significantly in VCP[R155H/+] cells following CCCP incubation (median VCP[R155H/+] control volume of 0.9321μm^3 decreased to 0.5125μm^3 after CCCP treatment; p=0.0118); several large components of the mitochondrial network remained, with the largest of these measuring 134.73μm^3. This may suggest that VCP-R155H mutation hinders the ability of the mitochondrial network to fragment completely following exposure to conditions of oxidative stress (Figure 4.6).

4.2.4 Comparison of total mitochondrial content in primary WT and VCP[R155H/+] fibroblasts

In order to investigate whether the differences in mitochondrial volumes were due to either inefficient degradation of the mitochondrial fusion proteins resulting from the expression of the IBMPFD mutant VCPR155H or possible differences in the total mitochondrial content, we utilised a Western blot in which mitochondrial content was measured by probing for TOMM20, an outer mitochondrial membrane translocase protein of 16kDa. We found that TOMM20 expression levels were similar in WT and VCP[R155H/+] cells (Figure 4.7). This provides evidence that the differences observed in CCCP-induced mitochondrial fragmentation may be due to the expression of the VCP mutation in these cells. Cells with continuously high metabolic demands, such as those found in brain, would be expected to have high capacity for oxidative phosphorylation for energy production and therefore high mitochondrial content. This can be seen in the TOMM20 band of brain lysate from WT mouse, where normalised TOMM20 expression is increased 5-fold in comparison with TOMM20 expression in primary fibroblasts (Figure 4.7).
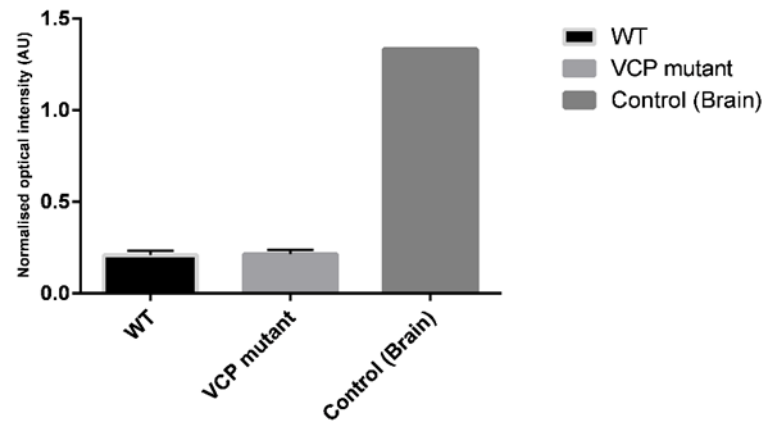
Figure 4.7 No significant differences in total mitochondrial content between primary WT and VCP$^{R155H/+}$ fibroblasts. TOMM20 is routinely used as a marker for total mitochondrial content. Western blotting of WT and VCP$^{R155H/+}$ fibroblast lysates showed low yet comparable expression of TOMM20, indicating similar mitochondrial content. WT brain lysate is used as a control of tissue with high metabolic demand therefore high mitochondrial content. (n=3 biological replicates for WT and VCP$^{R155H/+}$).

4.3. Discussion

Mitochondria are dynamic structures possessing great plasticity with regard to morphological remodelling. Various stimuli can induce drastic structural transformation of the mitochondrial network which can in turn impact upon the activity of mitochondrial enzyme complexes and thus on overall bioenergetic capacity (Brustovetsky *et al.*, 2009). Numerous studies have provided evidence of the tightly regulated relationship between mitochondrial network conformation and ATP generation (Benard *et al.*, 2006). Considerable structural remodelling of the networks was observed in HeLa cells cultured in a glucose-free, galactose- and glutamine-rich medium when compared with those growing in glucose-rich growth conditions, indicative of a profound morphological effect of switching from glycolysis to oxidative phosphorylation for ATP generation (Rossignol *et al.*, 2004). Under conditions in which glucose was freely available, the mitochondrial network was shown to cluster in the perinuclear region. However, when oxidative phosphorylation was stimulated, the network adopted a more reticular conformation, with the looped structures extending into the cytoplasm, possibly to facilitate provision of ATP to all parts of the cell (Rossignol *et al.*, 2004).

It follows from this that under- or overexpression of mitochondrial fusion and fission proteins would affect network conformation and subsequent bioenergetics. Indeed, antisense adenoviral-mediated Mfn2 knock-down in muscle cells resulted in decreased substrate oxidation, decreased mitochondrial membrane potential and down-regulation of subunits of oxidative phosphorylation complexes I, II, III and IV (Pich *et al.*, 2005). The opposite pattern was observed in Mfn2-overexpressing cells, with increased OXPHOS subunit expression reported (Pich *et al.*, 2005). Moreover, siRNA targeting of the mitochondrial fission protein Drp1 in HeLa cells resulted in abnormal branching and budding of the network concurrent with a reduction in mitochondrial ATP synthesis rate (Benard *et al.*, 2006). These studies underscore the importance of the morphological plasticity of the mitochondrial network in the context of fulfilling the fluctuating metabolic demands of the cell.

Therefore, it was important to investigate the possible impact of VCP mutation on the remodelling potential of mitochondrial networks, particularly in light of our discovery of fast-twitch muscle fibre-specific fatigue intolerance. Initial examination of fluorescently tagged EGFP-VCP transfected MEF cells revealed similar diffuse cytoplasmic distribution of both WT-VCP and VCP-R155H. Mitochondrial network structure did not seem to differ in MEF cells overexpressing WT and the R155H mutant VCP, with tubular mitochondrial

conformation observed in both under control growth conditions. In order to induce OXPHOS uncoupling and fragmentation of the mitochondrial network, we used the reversible protonophore CCCP, which causes proton leak from mitochondria, resulting in the dissipation of the mitochondrial membrane potential. We found that EGFP-tagged WT and VCPR155H remained diffusely located throughout the cytoplasm of CCCP-treated cells. The mitochondrial network fragmented following 3 hours of CCCP incubation, and neither WT-VCP nor VCPR155H colocalised with the fragmented mitochondria (Figure 4.1). Interestingly, CCCP incubation appeared to induce nuclear localisation of transfected EGFP-VCP-WT in some cells (Figure 4.1). This effect was also occasionally observed in primary fibroblasts from both WT and VCPR155H mutant mice, but was not consistent for any one condition, therefore cannot be considered an effect of oxidative stress on the localisation of VCP. However, CDC48 in yeast and VCP in humans have both been shown to relocalise throughout the course of the cell cycle, with VCP accumulating at the centrosomes during mitosis (Madeo *et al.*, 1998), therefore it may indicate the stage of the cell cycle the particular cell is in. In addition, a fraction of cellular VCP is contained in the nucleus where it is involved in chromatin-associated events and quality control of nuclear proteins (Xia *et al.*, 2016).

After optimising the conditions for mitochondrial staining using MitoTracker CMX Ros, we decided to examine in detail a system in which endogenous levels of either WT-VCP or VCPR155H were expressed. In order to do this, we isolated and cultured primary fibroblasts from our VCP$^{R155H/+}$ mouse model of IBMPFD, which has been shown by others to phenocopy the disease in humans (Badadani *et al.*, 2010). It is important to note that the fibroblasts we used to visualise mitochondrial dynamics were isolated from young mice (up to 3 months of age). This was due to a lack of older mice in our breeding colony when these experiments were carried out. The results of these experiments therefore did not exactly represent mitochondrial dynamics in a very aged animal, but do reveal the acute effects of oxidative stress on the mitochondrial networks in these cells.

Initially, antibodies for endogenous VCP immunodetection proved to be insufficiently sensitive, however after optimising several different antibodies, we found an anti-VCP antibody which yielded vastly better immunofluorescence staining. The primary fibroblasts from WT and VCPR155H mice were incubated with 50um CCCP for three hours – a period shown to induce mitochondrial fragmentation but not total cellular apoptosis (Yang *et al.*, 2001) – followed by removal of CCCP by rinsing in DMEM and subsequent mitochondrial labelling using 300nM MitoTracker CMXRos for 25 minutes. Interestingly,

despite the CCCP-induced depolarisation of the mitochondrial membrane potential, the individual fragmented mitochondria regained their proton gradient to take in the membrane potential-dependent dye, indicating the reconstitution of the proton gradient and demonstrating the reversibility of protonophore and the rapid adaptation of mitochondria to the removal of an external oxidative stressor. We found that, while the mitochondria in both WT-VCP and VCPR155H fibroblasts fragmented following OXPHOS uncoupling, VCP distribution became more punctate, however these aggregates did not colocalise with the fragmented mitochondria (Figure 4.2).

The dynamic nature of mitochondria in the cellular environment and the limitations of 2D analysis in terms of accurately deciphering morphological changes in the network necessitated a more in-depth examination of the structures in order to determine the effects of VCP mutation on the ability of the network to fragment when exposed to environmental stresses. Our initial visual analysis led towards investigating the oxidative stress-induced morphological changes in the mitochondrial networks of primary fibroblasts in a more quantitative manner, as morphological changes in the network impact upon its energy-generating capacity (Benard *et al.*, 2006). Continued ATP generation via oxidative phosphorylation is necessary to meet the changing metabolic demands of the cell, therefore mitochondrial quality control mechanisms must be tightly regulated in order to preserve mitochondrial network integrity. Fission and fusion processes allow damaged mitochondria to be readily removed from the network and recruited to critical subcellular compartments. When these events are compromised, whether through dysfunction/inhibited degradation of the fusion proteins or dysregulation of the associated proteins involved in the targeting of dysfunctional mitochondrial proteins, catastrophic cellular dysfunction ensues (Ashrafi *et al.*, 2013; Tait *et al.*, 2010; Hagen *et al.*, 1997). Indeed, mice lacking mitofusin proteins Mfn1 and Mfn2 do not survive beyond mid-gestation, with homozygous Mfn1 mutation proving to be embryonically lethal (Chen *et al.*, 2003). Also, disruption of mitochondrial fission through RNA interference or expression of a dominant negative variants of Drp1 results in elongated mitochondria that become entangled and subsequently collapse into the perinuclear region (Smirnov *et al.*, 2001), again underscoring the vital nature of these dynamic mitochondrial characteristics.

As previously outlined, the process of mitophagy is essential in the removal of aberrant mitochondria from the network. The successful removal of dysfunctional Mfn1 and Mfn2 from the mitochondrial membrane requires intact VCP and the subsequent proteasomal degradation of these proteins prevents re-fusion of damaged mitochondria

with the network. Ubiquitination of Mfn1 was found to be increased in Parkin-expressing HeLa cells overexpressing the dominant negative ATPase deficient E305Q/E578Q VCP mutant (Tanaka *et al.*, 2010). Proteasomal degradation of ubiquitinated Mfn1 was inhibited by this expression, indicating that the ATPase function of VCP is required for the retrotranslocation of these tagged proteins for degradation. The clinically relevant disease-associated R155H missense mutation still displays ATPase function (Weihl *et al.*, 2006), therefore we wanted to investigate the impact of this mutation in relation to mitochondrial fragmentation.

Using Imaris analysis software, we converted high magnification Z-stacked microscope images into a 3D reconstruction or rendering which could be analysed topologically by the software. We were able to quantify, in μm^3, the changes occurring in network volume in WT-VCP and VCP-R155H under control growth conditions and following exposure to oxidative stress. Notably, the volumes of mitochondrial objects were significantly smaller in VCPR155H-expressing fibroblasts when compared to WT cells under control conditions. The reasons behind this are unclear; one would expect that, if the degradation of mitochondrial fusion proteins were affected by the expression of VCPR155H, the mitochondrial networks in these cells would be longer, owing to disrupted fission. However, it has been demonstrated that intact VCP is required for PINK1/Parkin-mediated mitochondrial quality control (Kim *et al.*, 2013); therefore it is possible that the final degradation of the smaller mitochondria that have been removed from the network may be impeded by the expression of dysfunctional VCP.

We compared mitochondrial object volumes statistically using an ANOVA on ranks with a Tukey post-hoc analysis and, in both WT-VCP and VCPR155H-expressing fibroblasts, a significant reduction in mitochondrial volumes following CCCP treatment was observed (Figure 4.6). Notably however, several mitochondrial objects with volumes exceeding 100 μm^3 were recorded in VCPR155H-expressing cells (compared with the largest mitochondrial object measuring 51.7 μm^3 in WT-VCP cells), possibly indicating incomplete fragmentation of the network in these cells.

Chapter 5

Discussion

As described in chapter 1, the AAA+ ATPase, VCP, is involved in a plethora of cellular activities, and missense mutations in the encoding gene result in the development of IBMPFD, a complex, multisystem disorder, resulting in death of patients. Much research has investigated the role of VCP in numerous physiologic and pathologic processes, and the availability of disease models of VCP mutation has greatly enhanced our knowledge of the aberrant processes in IBMPFD pathological development.

The most common presenting symptom in IBMPFD is progressive proximal and distal muscle weakness and wasting, evident in patients at approximately 45 years of age. Histological analysis of affected muscle reveals variable features of myopathy. The heterozygous VCP-R155H mutation in mice results in age-dependent loss of force in skeletal muscle, delayed force recovery post-FP and diminished grip strength and Rotarod performance. In order to further elucidate the functional impact of VCP mutation on skeletal muscle, we used a knock-in VCP mutant mouse model, allowing us to tease out the processes involved in the age-related myopathic degeneration and examine the functional consequences of VCP mutation within a system. Studies on the knock-in mouse model of the disease, in which the R155H mutation is constitutively introduced into one VCP allele, have shown abnormal swollen mitochondria, prompting investigation into the effects of the mutation on the energy generating capacity of the tissue in response to contractile stimulation. Our work was initially directed towards determining whether VCP mutation affected force production and prolonged contractile capability, in the context of a potentially dysfunctional mitochondrial network. We found that, following a fatigue protocol, in which maximal isometric contractions were stimulated in fibre bundles isolated from EDL and soleus, fast-twitch fibre bundles from the $VCP^{R155H/+}$ mouse exhibited reduced fatigue tolerance and delayed post-fatigue recovery. This effect of VCP mutation was evident only in fast-twitch fibre bundles from aged mice, similar to the age-dependent nature of the disease in humans, and reinforcing the phenotypic similarities of the mouse model and the human disease. It is important to note that, unlike in humans, the

heterozygous expression of VCPR155H in mice did not result in early death for all animals harbouring the mutation, as evidenced by the very aged (27 month old) group of mice included in our experiments. It would be of great interest to examine the fibre composition of these animals to develop a clearer picture of why and how these animals recover from the muscle dysfunction seen in their younger counter parts.

Our findings indicate that the ability of fast-twitch muscle in VCP$^{R155H/+}$ mice to generate ATP for prolonged contractile activity is diminished. This may result from the reported presence of abnormal mitochondria in VCP$^{R155H/+}$ mice and IBMPFD patient skeletal muscle tissue. As discussed before, ATP is required for contractile cross-bridge cycling, and the rate of cross-bridge formation is determined by the levels of ATP in the sarcoplasm. Numerous biochemical processes generate ATP, including glycogen and glucose metabolism, oxidative phosphorylation, lipid metabolism and creatine kinase-induced cleavage of phosphocreatine (Milone and Wong, 2013). Glycolysis, in the short term, and mitochondrial oxidative phosphorylation, in the longer term, generate ATP for contraction in muscle. Maintenance of mitochondrial function is essential for the successful generation of energy, therefore, if the mitochondrial network is dysfunctional, and ATP generation is compromised, short term contraction will be maintained, but prolonged activity may be compromised, as seen in our findings. This theory is supported by the observations of Bartolome and colleagues, in which ATP levels were reduced in primary fibroblasts isolated from patients harbouring VCP mutations (Bartolome *et al.*, 2013). The reduction in ATP generation may also support, and partially explain, the significantly prolonged recovery time of VCP$^{R155H/+}$ fast-twitch fibre bundles after the fatigue protocol. Indeed, mitochondrial myopathy commonly manifests as intolerance to exercise and premature fatigue (Milone and Wong, 2013). While the EDL is categorised as a fast-twitch muscle, experiments on single fibre preparations could further characterise the effects of VCP mutation on specific fibre subtypes, based on MHC expression.

Earlier studies which characterised myopathic changes in the VCP$^{R155H/+}$ mouse model showed an age-dependent reduction in grip strength and Rotarod performance (Badadani *et al.*, 2010; Nalbandian *et al.*, 2012). Interestingly, the researchers found that a chronic exercise protocol, involving 30 minutes treadmill running three times per week for 6 weeks, improved performance in both grip strength and Rotarod (Nalbandian *et al.*, 2013). Histological analysis of quadriceps muscle tissue from the chronic exercise VCP$^{R155H/+}$ model showed marked improvement in the myopathy, revealing reduced atrophy and

fewer centrally located nuclei (indicating a reduction in myofibre degeneration). In addition, an increase in succinate dehydrogenase staining in quadriceps muscle was observed in the exercised animals, suggestive of an increase in oxidative potential (Nalbandian *et al.*, 2013).

Skeletal muscle is a highly adaptive tissue, which changes in response to variable environmental stimuli. Research has highlighted the benefits of exercise training in the context of muscular dystrophy conditions. Exercise is known to play a role in numerous processes, such as activation of molecular signalling pathways which stimulate myofibrillar protein synthesis and muscle hypertrophy, intracellular calcium handling and increased oxidative capacity (Mallinson *et al.*, 2013). The exercise-induced increase in muscle strength in $VCP^{R155H/+}$ mice observed by Nalbandian and colleagues (2015) was accompanied by an increase in oxidative potential of the tissue, emphasizing the retained ability of this tissue to adapt to external stimuli. As the analysis was conducted on quadriceps muscle biopsies, future investigations could include determining whether the oxidative capacity of fast- and slow-twitch muscle improves in a similar manner following prescription of a chronic exercise regimen. The application of an exercise protocol in early-stage IBMPFD patients could prove beneficial, however rigorous studies must be undertaken to fully assess the impacts of such a protocol on the overall health of individuals with muscle dysfunction, as injury propensity, due to myopathic instability and loss of strength, is increased. Measurement of mitochondrial enzyme activity showed a reduction in fast-twitch muscle from $VCP^{R155H/+}$ mice at 14 months, concomitant with reduced fatigue tolerance and delayed post-fatigue recovery.

The process of aging is accompanied by a gradual loss of muscle mass and subsequently functional capacity, known as sarcopenia (Rosenberg, 1997). However, many cellular and molecular changes occur in muscle fibres as individuals age. A decrease in muscle fibre number and size (predominantly type II fibres), reduced myosin protein content and function, calcium release deficits and disrupted excitation-contraction coupling all contribute to the overall loss of skeletal muscle integrity and function that is seen during the aging process (Lexell, 1995; D'Antona *et al.*, 2003; Russ *et al.*, 2011; Miljkovic *et al.*, 2015). Interestingly, the reduction in fibre size is fibre type-specific, with type II fibres 10-40% smaller in elderly individuals compared with young controls (Lexell, 1995). In contrast, type I fibre size remains largely unchanged. This age-dependent change can be explained by age-associated remodelling of the motor unit structure, whereby type II fibres become

denervated and type I fibres are re-innervated. Conversely, our research has demonstrated an increase in fast-oxidative and fast-glycolytic fibre size in 12 month old VCP$^{R155H/+}$ EDL when compared with wild-type controls (Figure 3.11). However, at 14 months, intermediate (fast-oxidative-glycolytic) fibres are significantly smaller in the VCP$^{R155H/+}$ EDL. No clear pattern in fast-twitch fibre size alteration was observed in analysis using cryosections, an observation also made by Hübbers and colleagues (2006). One possible explanation for the increased fibre size may be the presence of rimmed vacuoles in muscle fibres, as seen in a skeletal muscle biopsy taken from a patient harbouring the VCP-R93C mutation (Hübbers *et al.*, 2006). While these rimmed vacuoles and inclusion bodies have been observed in the muscle of VCP mutant mice by other groups (Figure S.6.; Badadani *et al.*, 2010; Custer *et al.*, 2010; Nalbandian *et al.*, 2013), we did not encounter this phenomenon in our animals.

An interesting finding of our work was the apparent absence of fatigue-intolerance in very aged (27 month old) VCP$^{R155H/+}$ mice when compared with WT controls. One potential explanation for this may lie in the reported protective effects of chronic low level mitochondrial stress in skeletal muscle. Chronic oxidative stress, and the resulting production of reactive oxygen species (ROS), has long been purported to be the underlying cause of aging (Harman, 1956). However, reports have presented conflicting evidence of the effect of chronic oxidative stress on cells. In fact, it is now generally accepted that treatment aimed at reducing the levels of free radicals in cells, namely antioxidant therapy, is ineffective, and may be harmful to the overall population (Miller, 2005). Studies have attempted to elucidate the mechanisms by which low levels of stress, particularly oxidative stress in the mitochondrion, induce adaptive cryoprotective signalling responses (Owusu-Ansah *et al.*, 2013). Mitochondrial perturbation and dysfunction results in the production of ROS, therefore it may be possible that the very aged mice in our study were subjected to low level chronic oxidative stress over their lifespan, and as such, developed adaptive mechanisms to counteract this stress, thus promoting longevity in these animals. If this was the case, the skeletal muscle fatigue-tolerance of these animals may be preserved, however this theory requires much further investigation.

The dynamic nature of the mitochondrial network dictated that several methods of examination were required to uncover possible effects of VCP mutation on mitochondrial fusion and fission events. Immunofluorescent labelling of endogenous VCP in primary cells from VCP$^{R155H/+}$ mice in conjunction with live staining of the mitochondrial networks

enabled us to visualise localisation of VCP in relation to the networks under both steady-state and stressful conditions. The translocation of VCP to mitochondria upon uncoupling has been shown in HeLa cells (Tanaka *et al.*, 2010), however this process was shown to be dependent on the transient expression of the E3-ub ligase Parkin, which is expressed at varying levels in different cell types with high expression observed in neuronal cells and negligible amounts seen in others (Matsuda *et al.*, 2010). Endogenous Parkin expression was determined in WT and VCP-R155H primary fibroblasts, showing significantly lower expression when compared with a WT brain lysate (Figure 4.3). Neither wild type nor mutated VCP was shown to colocalise with uncoupled mitochondria in primary fibroblasts from WT and VCP$^{R155H/+}$ mice (Figure 4.2), further emphasising the Parkin-dependence of this translocation. Indeed, Kimura *et al.* demonstrated the colocalisation of WT-VCP with the mitochondria in Parkin-expressing HeLa cells upon CCCP-induced uncoupling of the mitochondrial membrane potential. However, pathogenic EGFP-VCP-R155H, transfected into MEF cells, remained diffusely distributed throughout the cytoplasm of these cells in response to the uncoupling agent. We have shown that in fibroblast cells, which lack high Parkin expression, neither WT nor pathogenic R155H-mutated VCP respond to disruption of mitochondrial membrane potential and subsequent fragmentation of the network. It is important to note that in skeletal muscle, *parkin* gene (Kitada *et al.*, 1998) and protein expression (Van Humbeek *et al.*, 2008) are similar to that in brain tissue, therefore this may impact upon the localisation of VCP in relation to the mitochondrial network in skeletal muscle tissue.

Recently, Nalbandian and colleagues have studied the mitochondrial bioenergetics of primary myoblasts, isolated from both IBMPFD patients and the VCP$^{R155H/+}$ mouse disease model. Basal respiration, proton leak, ATP turnover and both spare and maximal respiratory capacity were measured, using the Seahorse Metabolic Flux Analyser. The experiments revealed decreased ATP levels, spare respiratory capacity and increased proton leak in VCP-deficient cells, indicating a loss of mitochondrial membrane integrity. Again, future studies might utilise this technique to assess how mitochondrial bioenergetics in VCP-mutant mice are affected following the application of a chronic exercise protocol. This would clearly demonstrate the specific components of the mitochondrial respiratory chain that are adapting and improving skeletal muscle performance in these animals (Nalbandian *et al.*, 2013).

Mitochondria are a major source of free radicals, or reactive oxygen species (ROS) within the cell. It is estimated that between 0.4-4.0% of the oxygen used during ATP generation in the cell is converted to superoxide radicals by mitochondria (Pieczenik and Neustadt, 2007). Mitochondrial dysfunction has been implicated in a melange of acquired conditions and pathologies, such as diabetes, cancer, Huntington's disease, Alzheimer's disease, Parkinson's disease, aging and cardiovascular disease (Stavrovskaya and Kristal, 2005; Fosslien *et al.*, 2001; Wallace *et al.*, 2005). Our work has uncovered mitochondrial fission deficits in the $VCP^{R155H/+}$ mouse model, which may lead to impaired mitochondrial dynamics and subsequent cellular dysfunction and death. Interestingly, symptoms of mitochondria-related disorders typically develop over years, and it is uncommon for these disorders to be diagnosed when symptoms first present (Cohen and Gold, 2001), as is generally the case with IBMPFD patients. Mitochondrial dysfunction may affect any tissue in the body, therefore the pathologic consequences in each tissue type may appear very distinct, again, as observed in the variety of pathological penetrance in IBMPFD patients.

This work served to underscore the hypothesis that VCP mutant-induced mitochondrial dysfunction results in decreased contractile activity in skeletal muscle, the primary tissue affected by mutations in the VCP gene. Further investigations have implicated dysfunctional VCP in mitochondrial deficits in neuronal cells types (Fang *et al.*, 2015), as failure to maintain mitochondrial health is central to neurodegeneration (Karbowski and Neutzner, 2012). Quality control of membrane-bound proteins involves their extraction from the membrane and retrotranslocation into the cytosol for degradation. VCP is a key player in this process, as has been evidenced by its role in ERAD (Wolf and Stolz, 2012). Our research has added to the ever-growing cellular repertoire of VCP.

Despite significant progress in delineating the numerous cellular functions of VCP and characterising the pathological consequences of VCP mutation, there are currently no therapeutic strategies for IBMPFD patients (Nalbandian *et al.*, 2013). Several studies have provided evidence of the beneficial effects of exercise training in muscular dystrophy conditions, due to its critical role in cellular processes such as signalling pathway activation, intracellular calcium movements and increased antioxidant capacity. Chronic exercise training was shown to improve the myopathy in the $VCP^{R155H/+}$ mouse model (Nalbandian *et al.*, 2013). The authors demonstrated that autophagy was intact in the exercised animals, as evidenced by a decrease in typical autophagy marker proteins, such as ubiquitin, p62

and LC3-II, which accumulate in the VCP$^{R155H/+}$ mouse model under homeostatic conditions. Following the exercise regimen, a decrease in the ubiquitin- and TDP-43-positive inclusions has been observed, which suggests the cytotoxic proteinaceous aggregates are being broken down. The authors suggest that the exercise-induced depletion of ATP and the resulting upregulation of the AMP-activated protein kinase (AMPK) pathway increases autophagic proteolysis via inhibition of the mTOR pathway, thus clearing, at least in part, the accumulated cellular debris. Application of a long-term exercise protocol may therefore help to delay IBMPFD myopathic degeneration by both improving mitochondrial function and increasing AMPK-mediated aggregate clearance.

It is important to recognise some of the limitations with the present work. Caution is required when extrapolating data obtained from studies of genetically modified animals in order to investigate the effects of a disease on muscle function in humans. For example, there are large differences in phenotypic expression and biomechanical properties of the dystrophic disease in humans and the mdx mouse, therefore translational gaps exist in this model (Duan, 2015). Mice, unlike humans, are quadrapedal, therefore the stresses and force exerted on skeletal muscles in mice differ from that in humans. Nonetheless, smaller animal models, such as mice, provide an extremely useful tool for the initial investigation into and analysis of the molecular basis of a disease in humans. Our work was also limited by the small n numbers used in the muscle mechanics experiments. Ideally, a higher n number would have strengthened the statistical power, reduced the standard error and decreased the likelihood of incurring a type I error in our results.

In summary, our research into the biomechanical and physiological consequences of VCP mutation in an animal model of the clinically relevant disorder IBMPFD supports the emerging theory that VCP plays an integral role in mitochondrial maintenance, and heterozygous expression of the IBMPFD mutant, VCP-R155H, results in mitochondrial deficits which present symptomatically as fatigue intolerance and delayed recovery in fast-twitch skeletal muscle.

Supplementary data
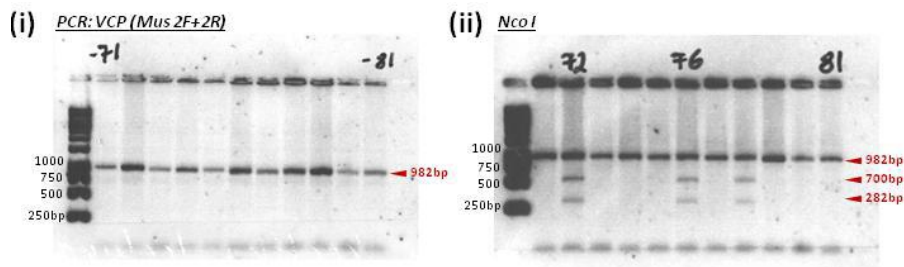
Figure S.1 Analysis of VCP$^{R155H/+}$ knock-in mouse genotype. (i) PCR protocol resulted in the generation of DNA fragments of 982bp in size. (ii) Restriction enzyme digestion of PCR products with Nco1 resulted in three DNA fragments (982bp, 700bp and 282bp) in the heterozygous VCP$^{R155H/+}$ mouse extracts only
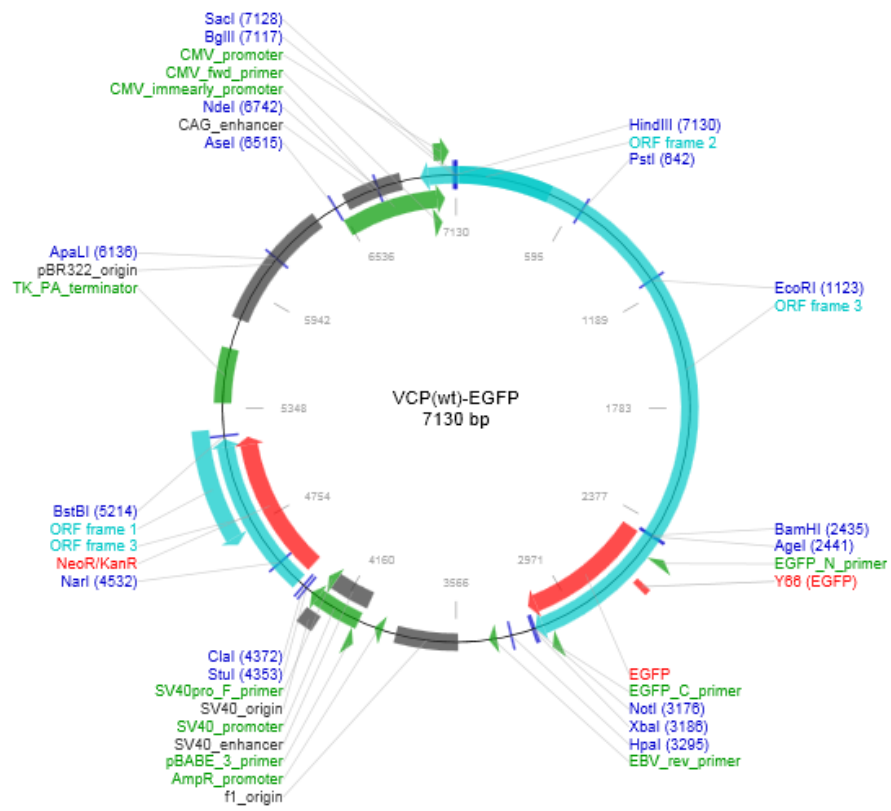
Figure S.2. Plasmid map of EGFP-tagged WT-VCP including restriction sites.
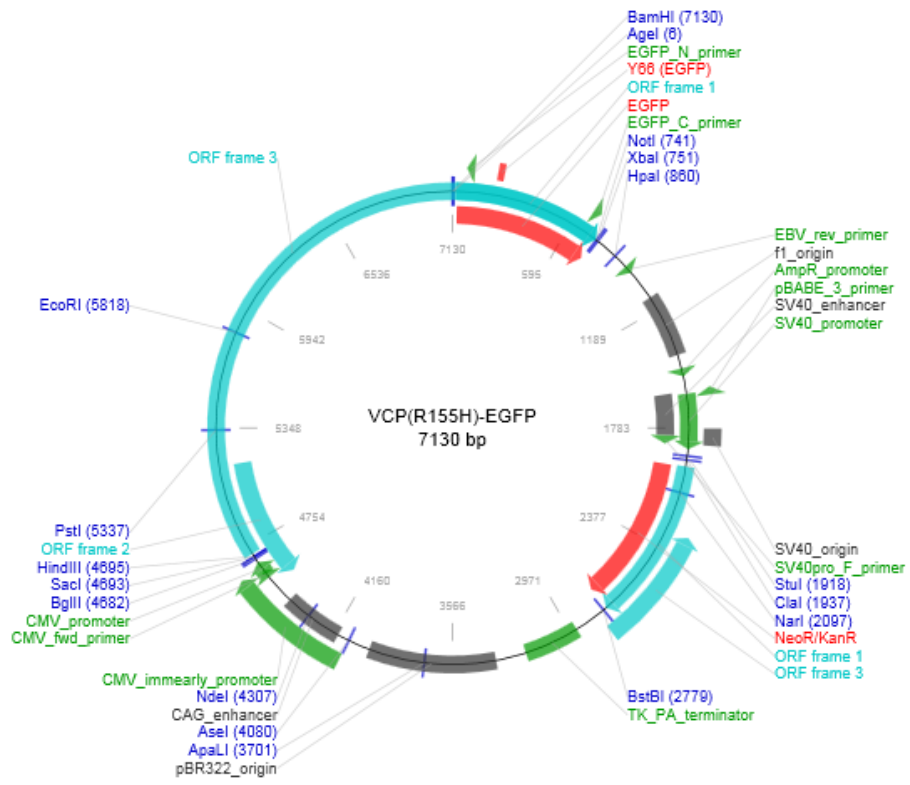
Figure S.3. Plasmid map of EGFP-tagged VCP^{R155H} with restriction sites.
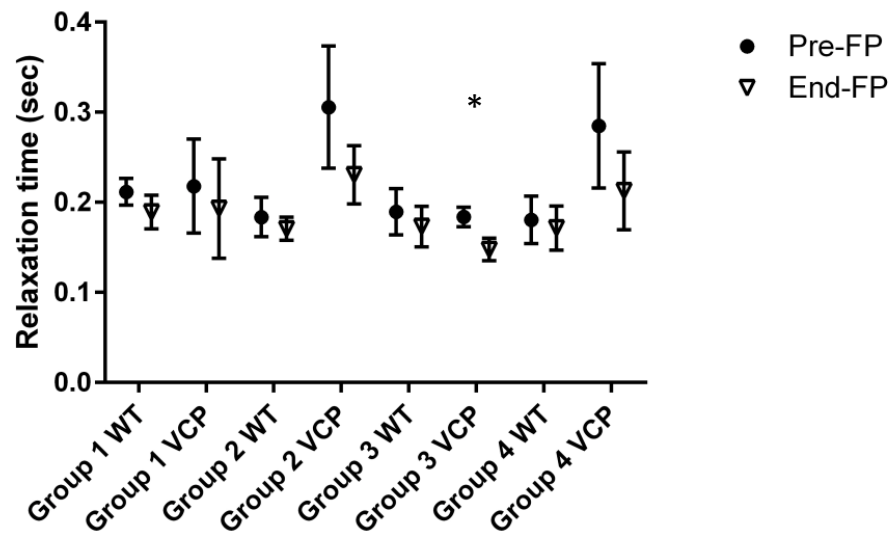
Figure S.4. Fatigue-induced changes in tetanic contraction characteristics in aged VCP$^{R155H/+}$ fast-twitch fibre bundles. Average tetanic relaxation time of age-matched WT and VCP$^{R155H/+}$ fast-twitch fibre bundles prior to fatigue protocol (Pre-FP; closed circles) and at the end of the fatigue protocol (End-FP; open triangles). Graph represents the average of three tetanic contractions pre-FP and the final three contractions of the FP ±SEM. At 14 months (Group 3), VCP$^{R155H/+}$ fast-twitch fibre terminal-FP tetanic relaxation times were significantly faster than pre-FP tetanic relaxation times (0.143±0.013 sec compared to 0.186±0.012 sec respectively, P<0.05).

A

MHC-F
Nidogen-1

MHC-S
Nidogen-1
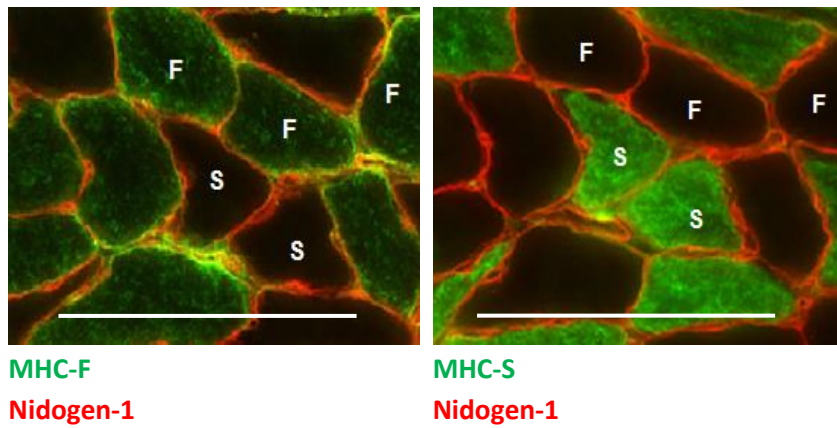
B
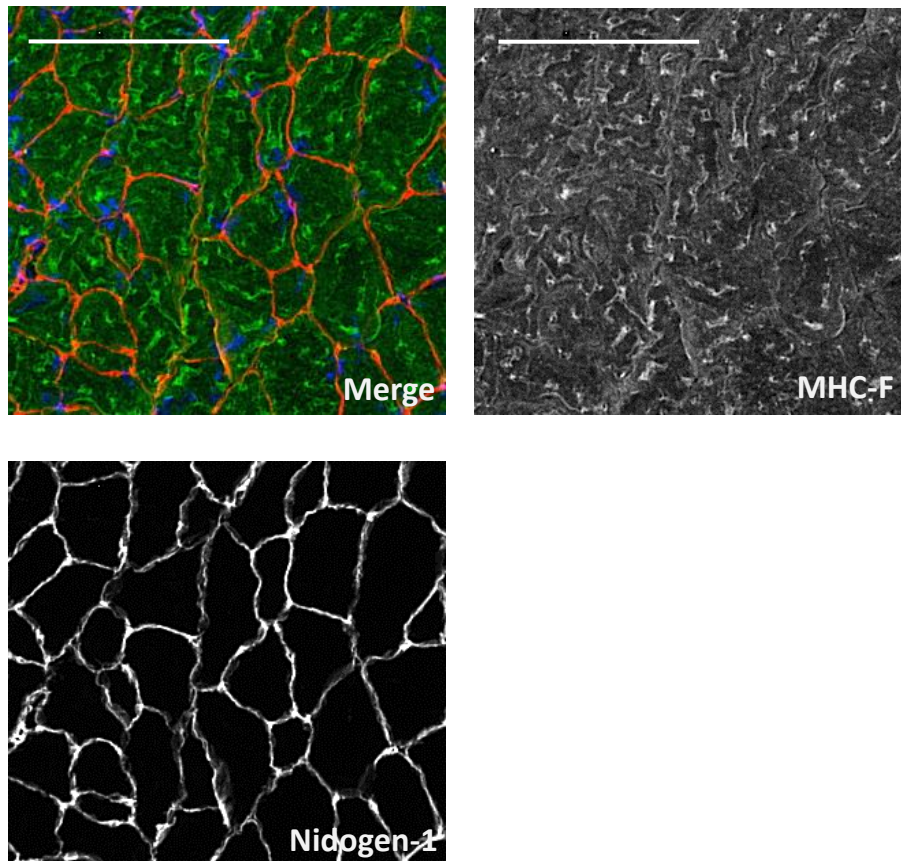
Figure S.5 Immunostained cryosections of (A) soleus and (B) EDL. Antibodies raised against MHC type I and all isoforms of MHC type II were used to confirm that all fibres in EDL were MHC type II. Note, as all fibres in EDL were found to be type II, a cryosection of soleus is used to show the contrast between MHC-F- and MHC-S-positive fibres. Nidogen-1(red) antibody was used to stain the basement membrane. (Scale bars: 100μm).
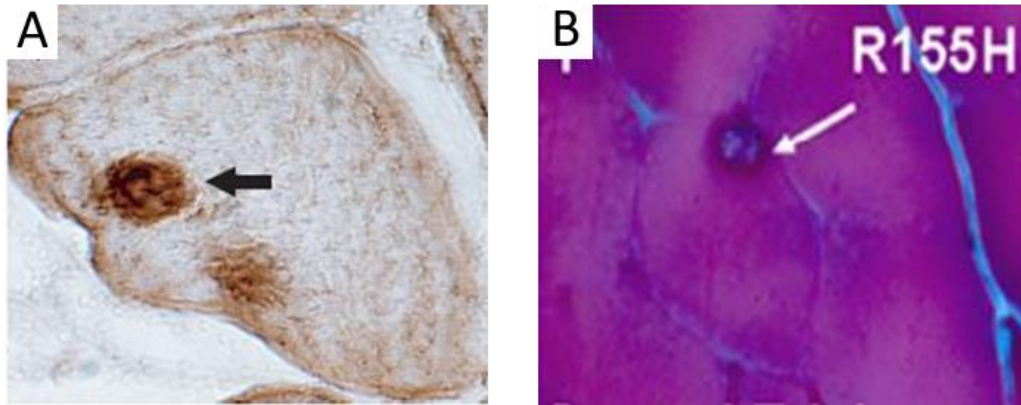
Figure S.6 Comparison of skeletal muscle pathology in (A) IBMPFD patient biopsy and (B) VCPR155H-mutant mouse. (A) Biopsy of muscle taken from IBMPDF patient which has been stained using a polyclonal VCP antibody. Large focal inclusion (arrow) in the muscle fibre contains VCP. (B) Modified Gomori Trichrome staining of quadricep section from VCPR155H/+ knock-in mouse shows the presence of rimmed vacuoles (indicated by black arrow) (images taken from Watts *et al.*, 2004 (A) and Badadani *et al.*, 2010 (B)).

References

Allen, D.G., Lamb, G.D and Westerblad, H. (2008) Skeletal muscle fatigue: cellular mechanisms. *Physiol. Rev.* 88: 287-332

Alzayady, K.J., Panning, M.M., Kelley, G.G. and Wojcikiewicz, R.J.H. (2005) Involvement of the p97-Ufd1-Npl4 complex in the Regulated Endoplasmic Reticulum-associated Degradation of Inositol 1,4,5-Triphosphate Receptors. *J. Biol. Chem.* 280(41): 34530-37

Ashrafi, G. and Schwarz, T.L. (2013) The pathways of mitophagy for quality control and clearance of mitochondria. *Cell Death Differ*. 20(1): 31-42

Badadani, M., Nalbandian, A., Watts, G.D., Vesa, J., Kitazawa, M., Su, H., Tanaja, J., Dec, E., Wallace, D.C., Mukherjee, J., Caiozzo, V., Warman, M. and Kimonis, V.E. (2010) VCP associated inclusion body myopathy and Paget disease of bone knock-in mouse model exhibits tissue pathology typical of human disease. *PLoS One* 5(10): e13183

Baker, J.S., McCormick, M.C. and Robergs, R.A. (2010) Interaction among skeletal muscle metabolic energy systems during intense exercise. *Review*, *J. Nutr. Metab.* 905612

Bartolome, F., Wu, H.C., Burchell, V.S., Preza, E., Wray, S., Mahoney, C.J., Fox, N.C., Calvo, A., Canosa, A., Moglia, C., Mandrioli, J., Chiò, A., Orrell, R.W., Houlden, H., Hardy, J., Abramov, A.Y. and Plun-Favreau, H. (2013) Pathogenic VCP mutations induce mitochondrial uncoupling and reduced ATP levels. *Neuron* 78(1): 57-64

Benard, G., Bellance, N., James, D., Parrone, P., Fernandez, H., Letellier, T. and Rossignol, R. (2007) Mitochondrial bioenergetics and structural network organization. *J. Cell Sci.* 120: 838-48

Böhm, S., Lamberti, G., Fernández-Sáiz, V., Stapf, C. and Buchberger, A. (2011) Cellular functions of Ufd2 and Ufd3 in proteasomal protein degradation depend on Cdc48 binding. *Mol. Cell. Biol.* 31(7): 1528-39

Braun, R.J., Zischka, H., Madeo, F., Eisenberg, T., Wissing, S., Büttner, S., Engelhardt, M., Büringer, D. and Ueffing, M. (2006) Crucial mitochondrial impairment upon *CDC48* mutation in apoptotic yeast. *J. Biol. Chem.* 281(35): 25757-67

Bug, M. and Meyer, H.H. (2012) Expanding into new markets – VCP/p97 in endocytosis and autophagy. *J. Struct. Biol.* 179: 78–82

Burkholder, T.J., Fingado, B., Baron, S. and Lieber, R.L. (1994) Relationship between muscle fiber types and sizes and muscle architectural properties in the mouse hindlimb. *J. Morphol.* 221(2): 177-90

Brustovetsky, T., Li, V. and Brustovetsky, N. (2009) Stimulation of glutamate receptors in cultured hippocampal neurons causes Ca^{2+}-dependent mitochondrial contraction. *Cell Calcium* 46(1): 18-29

Cairns, S.P., Taberner, A.J. and Loiselle, D.S. (2009) Changes of surface and t-tubular membrane excitability during fatigue with repeated tetani in isolated mouse fast- and slow-twitch muscle. *J. Appl. Physiol.* 106(1): 101-12

Campello, S., Strappazzon, F. and Cecconi, F. (2014) Mitochondrial dismissal in mammals, from protein degradation to mitophagy. *Biochim. Biophys. Acta.* 1837(4): 451-60

Caughey, J.E., Gwynne, J.F. and Jefferson N.R. (1957) Dystrophia myotonica associated with familial Paget's disease (osteitis deformans) with sarcomata. *J. Bone Joint Surg.* 39-B(2):316-25

Chan, H.T., Lee, T.R., Huang, S.H., Lee, H.Y., Sang, T.K., Chan, H.L. and Lyu, P.C. (2012) Proteomic analysis of a drosophila IBMPFD model reveals potential pathogenic mechanisms. *Mol. Biosyst.* 6: 1730-41

Chen, H., Detmer, S.A., Ewald, A.J., Griffin, E.E., Fraser, S.E. and Chan, D.C. (2003) Mitofusins Mfn1 and Mfn2 co-ordinately regulate mitochondrial fusion and are essential for embryonic development. *J. Cell Biol.* 160(2): 189-200

Chen, H., Chomyn, A. and Chan, D.C. (2005) Disruption of fusion results in mitochondrial heterogeneity and dysfunction. *J. Biol. Chem.* 280(28): 26185-92

Chen, H., McCaffery, J.M. and Chan, D.C. (2007) Mitochondrial Fusion Protects against Neurodegeneration in the Cerebellum. *Cell* 130: 548–62

Codogno, P., Mehrpour, M. and Proikas-Cezanne, T. (2011) Canonical and non-canonical autophagy: variations on a common theme of self-eating? *Nat. Rev. Mol. Cell. Biol.* 13(1):7–12

Cohen, B. H. and Gold, D. R. (2001) Mitochondrial cytopathy in adults: what we know so far. *Cleve. Clin. J. Med.* 68(7):625-6, 629–42

Custer, S.K., Neumann, M., Lu, H., Wright, AC., Taylor, JP. (2010) Transgenic mice expressing mutant forms VCP/p97 recapitulate the full spectrum of IBMPFD including degeneration in muscle, brain and bone. *Hum. Mol. Genet.* 19:1741–1755

Dalal, S., Rosser, M.F., Cyr, D.M. and Hanson, P.I. (2004) Distinct roles for the AAA ATPases NSF and p97 in the secretory pathway. *Mol. Biol. Cell.* 15(2): 637–48

D'Antona, G., Pellegrino, M.A., Adami, R., Rossi, R., Carlizzi, C.N., Canepari, M., Saltin, B. and Bottinelli, R. (2003) The effect of ageing and immobilization on structure and function of human skeletal muscle fibres. *J. Physiol.* 552(Pt 2): 499–511.

Davies, V.J., Hollins, A.J., Piechota, M.J., Yip, W., Davies, J.R., White, K.E., Nicols, P.P., Boulton, M.E. and Votruba, M. (2007) Opa1 deficiency in a mouse model of autosomal dominant optic atrophy impairs mitochondrial morphology, optic nerve structure and visual function. *Hum. Mol. Genet.* 16(11): 1307-18

Dec, E., Ferguson, D., Nalbandian, A., Gargus, M., Katheria, V., Rana, P., Ibrahim, A., Hatch, M., Lan, M., Llewellyn, K.J., Keirstead, H. and Kimonis, V.E. (2014) Disease-specific induced pluripotent stem cell modelling: insights into the pathophysiology of Valosin containing protein disease. *J Stem Cell Res Ther* 4:2

DeLaBarre, B. and Brunger, A.T. (2003) Complete structure of p97/valosin-containing protein reveals communication between nucleotide domains. *Nat. Struct. Biol.* 10(10): 856-63

Delp, M.D. and Duan, C. (1996) Composition and size of type I, IIA, IID/X, and IIB fibers and citrate synthase activity of rat muscle. *J.Appl. Physiol.* 80(1): 261-70

de Winter, J.C.F. (2013) Using the Student's t-test with extremely small sample sizes. *Pract. Assess. Res. Eval.* 18:1–12

Ding, W.X., Guo, F., Ni, H.M., Bockus, A., Manley, S., Stolz, D.B., Eskelinen, E.L., Jaeschke, H. and Yin, X.M. (2012) Parkin and mitofusins reciprocally regulate mitophagy and mitochondrial spheroid formation. *J. Biol. Chem.* 287(50): 42379-88

Dreveny, I., Kondo, H., Uchiyama, K., Shaw, A., Zhang, X. and Freemont, P.S. (2004) Structural basis of the interaction between the AAA ATPase p97/VCP and its adaptor protein p47. *EMBO J.* 23(5): 1030-9

Duan, D. (2015) Duchenne muscular dystrophy gene therapy in the canine model. *Hum. Gene Ther. Clin. Dev.* 26(1):57-69

Escobar-Henriques, M. and Anton, F. (2013) Mechanistic perspective of mitochondrial fusion: Tubulation vs. fragmentation. *Biochim. Biophys. Acta* 1833: 162–175

Fang, L., Hemion, C., Pinho Ferreira Bento, A.C., Bippes, C.C., Flammer, J. and Neutzner, A. (2015) Mitochondrial function in neuronal cells depends on p97/VCP/Cdc48-mediated quality control. *Front. Cell. Neurosci.* 2: 9-16

Floeter, M.K. (2010) Structure and function of muscle fibres and motor units. *Disorders of Voluntary Muscle, 8th Edition, Camb. Univ. Press* 1-10

Forman, M.S., Mackenzie, I.R., Cairns, N.J., Swanson, E., Boyer, P.J., Drachman, D.A., Jhaveri, B.S., Karlawish, J.H., Pestronk, A., Smith, T.W., Tu, P.H., Watts, G.D., Markesbery, W.R., Smith, C.D. and Kimonis, V.E. (2006) Novel ubiquitin neuropathology in frontotemporal dementia with valosin-containing protein gene mutations. *J Neuropathol Exp Neurol.* Jun;65(6):571-81

Fosslien, E. (2001) Mitochondrial medicine-molecular pathology of defective oxidative phosphorylation. *Ann. Clin. Lab. Sci.* 31(1): 25-67

Fröhlich, K.U., Fries, H.W., Rüdiger, M., Erdmann, R., Botstein, D. and Mecke, D. (1991) Yeast Cell Cycle Protein CDC48p Shows Full-length Homology to the mammalian Protein VCP and Is a Member of a Protein Family Involved in Secretion, Peroxisome Formation and Gene Expression. *J. Cell. Biol.* 114(3): 443-53

Frontera, W.R., Meredith, C.N., O'Reilly, K.P., Knuttgen, H.G. and Evans, W.J. (1988) Strength conditioning in older men: skeletal muscle hypertrophy and improved function. *J. Appl. Physiol.* 64(3): 1038-44.

Geisler, S., Holmström, K.M., Skujat, D., Fiesel, F.C., Rothfuss, O.C., Kahle, P.J. and Springer, W. (2010) PINK1/Parkin-mediated mitophagy is dependent on VDAC1 and p62/SQSTM1. *Nat Cell Biol.* 12(2): 119-31

Goodrick, C.L. (1975) Life-span and the inheritance of longevity of inbred mice. *J. Gerontol.* 30(3): 257-63

Hagen, T.M., Yowe, D.L., Bartholomew, J.C., Wehr, C.M., Do, K.L., Park, J.Y. and Ames, B.N. (1997) Mitochondrial decay in hepatocytes from old rats: membrane potential declines, heterogeneity and oxidants increase. *Proc. Natl. Acad. Sci. USA.* 94(7): 3064-9

Halawani, D., LeBlanc, A.C., Rouiller, I., Michnick, S.W., Servant, M.J. and Latterich, M. (2009) Hereditary Inclusion Body Myopathy-Linked p97/VCP Mutations in the NH2 Domain and the D1 Ring Modulate p97/VCP ATPase Activity and D2 Ring Conformation. *Mol. Cell. Biol.* 29(16): 4484-94

Harman, D. (1956) Aging: a theory based on free radical and radiation chemistry. J. Gerontol. 11(3): 298-300

Heath-Engel, H.M. and Shore, G.C. (2006) Mitochondrial membrane dynamics, cristae remodelling and apoptosis. *Biochimica et Biophysica Acta* 1763: 549–560

Homsher, E. (1987) Muscle enthalpy production and its relationship to actomyosin ATPase. *Annu. Rev. Physiol.* 49:673-90.

Hübbers, C.U. et al. (2007) Pathological consequences of VCP mutations on human striated muscle. *Brain* 130(2): 381-393

Johansen, T. and Lamark, T. (2011) Selective autophagy mediated by autophagic adapter proteins. *Autophagy* 7(3): 279-96

Johnson, J.O *et al.* (2010) Exome sequencing reveals VCP mutation as a cause of familial ALS. *Neuron* 9; 68(5): 857–864

Ju, J.S., Fuentealba, R.A., Miller, S.E., Jackson, E., Piwnica-Worms, D., Baloh, R.H. and Weihl, C.C. (2009) Valosin-containing protein (VCP) is required for autophagy and is disrupted in VCP disease. *J. Cell Biol.* 187(6): 875-88

Ju, J.S. and Weihl, C.C. (2010) Inclusion body myopathy, Paget's disease of the bone and fronto-temporal dementia: a disorder of autophagy. *Hum. Mol. Genet.* (Review Issue) 19(1): 38-45

Karbowski, M. and Neutzner, A. (2012) Neurodegeneration as a consequence of failed mitochondrial maintenance. *Acta. Neuropathol.* 123(2): 157-71

Kim, N.C., Tresse, E., Kolaitis, R-M, Molliex, A., Thomas, R.E., Alami, N.E., Wang, B., Joshi, A., Smith, R.B., Ritson, G.P., Winborn, B.J., Moore, J., Lee, J-Y, Yao, T-P, Pallanck, L., Kundu, M. and Taylor, J.P. (2013) VCP is essential for mitochondrial quality control by PINK1/Parkin and this function is impaired by VCP mutations. *Neuron* 78: 65-80

Kimonis, V.E., Kovach, M.J., Waggoner, B., Leal, S., Salam, A., Rimer, L., Davis, K., Khardori, R. and Gelber, D. (2000) Clinical and molecular studies in a unique family with autosomal

dominant limb-girdle muscular dystrophy and Paget disease of bone. *Genet Med.* 2(4): 232-41

Kimonis, V.E., Fulchiero, E., Vesa, J. and Watts, G.D. (2008) VCP disease associated with myopathy, Paget disease of bone and frontotemporal dementia: review of a unique disorder. *Biochim. Biophys. Acta.* 1782(12): 744-8

Kimura, Y., Fukushi, J., Hori, S., Matsuda, N., Okatsu, K., Kakiyama, Y., Kawawaki, J., Kakizuka, A. and Tanaka, K. (2013) Different dynamic movements of wild-type and pathogenic VCPs and their cofactors to damaged mitochondria in a Parkin-mediated mitochondrial quality control system. *Genes Cells* 18(12): 1131-43

Kitada, T., Asakawa, S., Hattori, N., Matsumine, H., Yamamura, Y., Minoshima, S., Yokochi, M., Mizuno, Y., Shimizu, N. (1998) Mutations in the parkin gene cause autosomal recessive juvenile parkinsonism. *Nature* 1998 9;392(6676):605-8

Koller, K. J. and Brownstein, M. J. (1987) Use of a cDNA clone to identify a supposed precursor protein containing valosin. *Letters to Nature.* Feb; 325(6104):542-5

Kovach, M.J., Waggoner, B., Leal, S.M., Gelber, D., Khardori, R., Levenstien, M.A., Shanks, C.A., Gregg, G., Al-Lozi, M.T., Miller, T., Rakowicz, W., Lopate, G., Florence, J., Glosser, G., Simmons, Z., Morris, J.C., Whyte, M.P., Pestronk, A. and Kimonis, V.E. (2001) Clinical delineation and localization to chromosome 9p13.3-p12 of a unique dominant disorder in four families: hereditary inclusion body myopathy, Paget disease of bone, and frontotemporal dementia. *Mol. Genet. Metab.* 74(4): 458-75

Krick, R., Bremer, S., Welter, E., Schlotterhose, P., Muehe, Y., Eskelinen, E.L. and Thumm, M. (2010) Cdc48/p97 and Shp1/p47 regulate autophagosome biogenesis in concert with ubiquitin-like Atg8. *J. Cell Biol.* 190(6): 965-73

Lexell, J. (1995) Human aging, muscle mass, and fiber type composition. *J. Gerontol. A Biol. Sci. Med. Sci.* 50 Spec No: 11-6.

Li, Y., Park, J.S., Deng, J.H. and Bai, Y. (2006) Cytochrome c oxidase subunit IV is essential for assembly and respiratory function of the enzyme complex. *J. Bioenerg. Biomembr.* 38(5-6): 283-91

Lyons, C.N., Mathieu-Costello, O. and Moyes, C.D. (2006) Regulation of skeletal muscle mitochondrial content during aging. *J. Gerontol. A Biol. Sci. Med. Sci.* 61(1): 3-13

Madeo, F., Schlauer, J., Zischka, H., Mecke, D., Fröhlich, K.U. (1998) Tyrosine phosphorylation regulates cell cycle-dependent nuclear localization of Cdc48p. *Mol. Biol. Cell.* 9(1):131-41

Mallinson, J.E. and Murton, A.J. (2013) Mechanisms responsible for disuse muscle atrophy: potential role of protein provision and exercise as countermeasures. *Nutrition* 29(1): 22-8

Matsuda, N., Sato, S., Shiba, K., Okatsu, K., Saisho, K., Gautier, C.A., Sou, Y.S., Saiki, S., Kawajiri, S., Sato, F., Kimura, M., Komatsu, M., Hattori, N. and Tanaka, K. (2010) PINK1 stabilized by mitochondrial depolarization recruits Parkin to damaged mitochondria and activates latent Parkin for mitophagy. *J. Cell Biol.* 189(2): 211-21

Mehta, S.G., Khare, M., Ramani, R., Watts, G.D., Simon, M., Osann, K.E., Donkervoort, S., Dec, E., Nalbandian, A., Platt, J., Pasquali, M., Wang, A., Mozaffar, T., Smith, C.D. and Kimonis, V.E. (2013) Genotype-phenotype studies of VCP-associated inclusion body myopathy with Paget disease of bone and/or frontotemporal dementia. *Clin. Genet.* 83(5): 422-31

Meyer, H.H. and Weihl, C.C. (2014) The VCP/p97 system at a glance: connecting cellular function to disease pathogenesis. *Jour. Cell Sci.* 127: 3877–3883

Miljkovic, N., Lim, J.Y., Miljkovic, I. and Frontera, W.R. (2015) Aging of skeletal muscle fibers. *Ann. Rehabil. Med.* 39(2): 155-62

Miller, E.R., Pastor-Barriuso, R., Dalal, D., Riemersma, R.A., Appel, L.J. and Guallar, E. (2005) Meta-analysis: high-dosage vitamin E supplementation may increase all-cause mortality. *Ann. Intern. Med.* 142(1): 37-46

Milone, M. and Wong, L.J. (2013) Diagnosis of mitochondrial myopathies. *Mol. Genet. Metab.* 110(1-2): 35-41

Mizushima, N., Yamamoto, A., Matsui, M., Yoshimori, T. and Ohsumi, Y. (2004) *In Vivo* Analysis of Autophagy in Response to Nutrient Starvation Using Transgenic Mice Expressing a Fluorescent Autophagosome Marker. *Mol. Biol. Cell.* 15(3): 1101–1111

Mizushima, N. and Levine, B. (2010) Autophagy in mammalian development and differentiation. *Nat. Cell. Biol.* 12(9): 823-30

Mori-Konya, C., Kato, N., Maeda, R., Yasuda, K., Higashimae, N., Noguchi, M., Koike, M., Kimura, Y., Ohizumi, H., Hori, S. and Kakizuka, A. (2009) p97/valosin-containing protein (VCP) is highly modulated by phosphorylation and acetylation. *Genes Cells* 14(4): 483-97

Müller, J.M.M., Meyer, H.H., Ruhrbergi, C., Stamp, G.W., Warren, G. and Shima, D.T. (1999) The Mouse p97 (CDC48) Gene - Genomic Structure, Definition of Transcriptional Regulatory Sequences, Gene Expression, and Characterization of a Pseudogene. *J. Biol. Chem.* 274: 10154–62

Narendra, D., Tanaka, A., Suen, D-F and Youle, R.J. (2008) Parkin is recruited selectively to impaired mitochondria and promotes their autophagy. *J. Cell. Biol.* 183(5): 795-803

Nalbandian, A., Donkervoort, S., Dec, E., Badadani, M., Katheria, V., Rana, P., Nguyen, C., Mukherjee, J., Caiozzo, V., Martin, B., Watts, G.D., Vesa, J., Smith, C. and Kimonis, V.E. (2011) The multiple faces of valosin-containing protein-associated diseases: inclusion body myopathy with Paget's disease of bone, frontotemporal dementia, and amyotrophic lateral sclerosis. *J Mol Neurosci.* 45(3): 522-31

Nalbandian, A., Llewellyn, K.J., Kitazawa, M., Yin, H.Z., Badadani, M., Khanlou, N., Edwards, R., Nguyen, C., Mukherjee, J., Mozaffar, T., Watts, G.D., Weiss, J. and Kimonis, V.E. (2012) The Homozygote VCP($^{R155H/R155H}$) mouse exhibits accelerated human VCP-associated disease pathology. *PLoS One* 7(9): e46308

Nalbandian, A., Llewellyn, K.J., Badadani, M., Yin, H.Z., Nguyen, C., Katheria, V., Watts, G.D., Mukherjee, J., Vesa, J., Caiozzo, V., Mozaffar, T., Weiss, J.H. and Kimonis, V.E. (2013a) A progressive translational mouse model of human valosin-containing protein disease: the VCP($^{R155H/+}$) mouse. *Muscle Nerve* 47(2): 260-70

Nalbandian, A., Nguyen, C., Katheria, V., Llewellyn, K.J., Badadani, M., Caiozzo, V. and Kimonis, V.E. (2013b) Exercise training reverses skeletal muscle atrophy in an experimental model of VCP disease. *PLoS One* 8(10):e76187

Nalbandian, A., Llewellyn, K.J., Gomez, A., Walker, N., Su, H., Dunnigan, A., Chwa, M., Vesa, J., Kenney, M.C. and Kimonis, V.E. (2015) *In vitro* studies in VCP-associated multisystem proteinopathy suggest altered mitochondrial bioenergetics. *Mitochondrion* 22: 1-8

Narendra, D., Kane, L.A., Hauser, D.N., Fearnley, I.M. and Youle, R.J. (2010) p62/SQSTM1 is required for Parkin-induced mitochondrial clustering but not mitophagy; VDAC1 is dispensable for both. *Autophagy* 6(8):1090-106

Nilwik, R., Snijders, T., Leenders, M., Groen, B.B., van Kranenburg, J., Verdijk, L.B. and van Loon, L.J. (2013) The decline in skeletal muscle mass with aging is mainly attributed to a reduction in type II muscle fiber size. *Exp. Gerontol.* 48(5): 492-8

Niwa, H., Ewens, C.A., Tsang, C., Yeung, H.O., Zhang, X. and Freemont, P.S. (2012) The Role of the N-Domain in the ATPase Activity of the Mammalian AAA ATPase p97/VCP. *J. Biol. Chem.* 287(11): 8561-70

Owusu-Ansah, E., Song, W. and Perrimon, N. (2013) Muscle mitohormesis promotes longevity via systemic repression of insulin signalling. *Cell* 155(3): 699-712

Pagon, R.A., Bird, T.D. and Dolan, C.R. (2011) Inclusion Body Myopathy with Paget Disease of Bone and/or Frontotemporal Dementia. *GeneReviews* (http://www.ncbi.nlm.nih.gov/books/NBK1476/?report=printable)

Perry, S.W., Norman, J.P., Barbieri, J., Brown, E.B. and Gelbard, H.A. (2011) Mitochondrial membrane potential probes and the proton gradient: a practical usage guide. *Biotechniques* 50(2): 98-115

Pette, D. (1985) Metabolic heterogeneity of muscle fibres. *J. Exp. Biol.* 115:179-89

Piccirrilo, R. and Goldberg, A.L. (2012) The p97/VCP ATPase is critical in muscle atrophy and the accelerated degradation of muscle proteins. *EMBO J.* 31(15): 3334-50

Pich, S., Bach, D., Briones, P., Liesa, M., Camps, M., Testar, X., Palacín, M. and Zorzano, A. (2005) The Charcot-Marie-Tooth type 2A gene product, Mfn2, up-regulates fuel oxidation through expression of OXPHOS system. *Hum. Mol. Genet.* 14(11): 1405-15

Pieczenik, S.R. and Neustadt, J. (2007) Mitochondrial dysfunction and molecular pathways of disease. *Exp. Mol. Pathol.* 83(1):84-92

Pye, V.E., Dreveny, I., Briggs, L.C., Sands, C., Beuron, F., Zhang, X. and Freemont, P.S. (2006) Going through the motions: the ATPase cycle of p97. *J. Struct. Biol.* 156(1): 12-28

Pye, V.E., Beuron, F., Keetch, C.A., McKeown, C., Robinson, C.V., Meyer, H.H., Zhang, X., and Freemont, P.S. (2007) Structural insights into the p97-Ufd1-Npl4 complex. *PNAS* 104(2): 467–72

Rabinovich, E., Kerem, A., Fröhlich, K.U., Diamant, N. and Bar-Nun, S. (2002) AAA-ATPase p97/Cdc48, a Cytosolic Chaperone Required for Endoplasmic Reticulum-Associated Protein Degradation. *Mol. Cell. Biol.* 22(2): 626-34

Rabouille, C., Kondo, H., Newman, R., Hui, N., Freemont, P.and Warren, G. (1998) Syntaxin-5 is a common component of the NSF- and p97-mediated reassembly pathways of Golgi cisternae from mitotic Golgi fragments in vitro. *Cell.* 92(5): 603-10

Rosenberg, I.H. (1997) Sarcopenia: origins and clinical relevance. *J. Nutr.* 127(5 Suppl): 990S-991S

Rossignol, R., Gilkerson, R., Aggeler, R., Yamagata, K., Remington, S.J. and Capaldi, R.A. (2004) Energy substrate modulates mitochondrial structure and oxidative capacity in cancer cells. *Cancer Res.* 63(3): 985-93

Russ, D.W., Grandy, J.S., Toma, K. and Ward, C.W. (2011) Ageing, but not yet senescent, rats exhibit reduced muscle quality and sarcoplasmic reticulum function. *Acta. Physiol. (Oxf)* 201(3): 391-403

Schiaffino, S. and Reggiani, C. (2011) Fiber types in mammalian skeletal muscle. *Physiol. Rev.* 91(4): 1447-531

Selva-O'Callaghan, A., Sanchez-Sitjes, L., Muñoz-Gall, X., Mijares-Boeckh-Behrens, T., Solans-Laque, R., Angel Bosch-Gil, J., Morell-Brotad, F. and Vilardell-Tarrés, M. (2000) Respiratory failure due to muscle weakness in inflammatory myopathies: maintenance therapy with home mechanical ventilation. *Rheumatology (Oxford).* 39(8): 914-6.

Smerdu V, Karsch-Mizrachi I, Campione M, Leinwand L, Schiaffino S. (1994) Type IIx myosin heavy chain transcripts are expressed in type IIb fibers of human skeletal muscle. *Am. J. Physiol.* 267(6 Pt 1): C1723-8

Smirnova, E., Griparic, L., Shurland, D.L. and van der Bliek, A.M. (2001) Dynamin-related protein Drp1 is required for mitochondrial division in mammalian cells. *Mol. Biol. Cell.* 12(8): 2245-56

Srere, P.A. (1969) Citrate Synthase. *Methods Enzym*. 13: 3-11

Stavrovskaya, I.G and Kristal, B.S. (2005) The powerhouse takes control of the cell: is the mitochondrial permeability transition a viable therapeutic target against neuronal dysfunction and death? *Free Radic. Biol. Med.* 38(6): 687-97

Stojkovic, T., Hammouda, el H., Richard, P., López de Munain, A., Ruiz-Martinez, J., Camaño, P., Laforêt, P., Pénisson-Besnier, I., Ferrer, X., Lacour, A., Lacomblez, L., Claeys, K.G., Maurage, C.A., Fardeau, M. and Eymard, B. (2009) Clinical outcome in 19 French and

Spanish patients with valosin-containing protein myopathy associated with Paget's disease of bone and frontotemporal dementia. *Neuromuscul. Disord*. 19(5):316-23

Storer, J.B. (1966) Longevity and gross pathology at death in 22 inbred mouse strains. *J. Gerontol*. 21(3): 404-9

Stump, C.S., Short, K.R., Bigelow, M.L., Schimke, J.M. and Nair, K.S. (2003) Effect of insulin on human skeletal muscle mitochondrial ATP production, protein synthesis, and mRNA transcripts. *Proc. Natl. Acad. Sci. USA.* 100(13): 7996-8001

Tait, S.W., Parsons, M.J., Llambi, F., Bouchier-Hayes, L., Connell, S., Muñoz-Pinedo, C. and Green, D.R. (2010) Resistance to caspase-independent cell death requires persistence of intact mitochondria. *Dev. Cell.* 18(5): 802-13

Tanaka, A., Cleland, M.M., Xu, S., Narendra, D.P., Suen, D-F, Karbowski, M. and Youle, R.J. (2010) Proteasome and p97 mediate mitophagy and degradation of mitofusins induced by Parkin. *J. Cell. Biol.* 191(7): 1367-80

Tastuta, T. and Langer, T. (2008) Quality control of mitochondria: protection against neurodegeneration and ageing. *EMBO J.* 27: 306-14

Tresse, E., Salomons, F.A., Vesa, J., Bott, L.C., Kimonis, V.E., Yao, T.P., Dantuma, N.P. and Taylor, J.P. (2010) VCP/p97 is essential for maturation of ubiquitin-containing autophagosomes and this function is impaired by mutations that cause IBMPFD. *Autophagy* 6(2): 217-27

Truett, G.E., Heeger, P., Mynatt, R.L., Truett, A.A., Walker, J.A. and Warman, M.L. (2000) Preparation of PCR-quality mouse genomic DNA with hot sodium hydroxide and tris (HotSHOT) *Biotechniques* 29(1): 52, 54

Van Humbeeck, C., Waelkens, E., Corti, O., Brice, A., Vandenberghe, W. (2008) Parkin occurs in a stable, non-covalent, approximately 110-kDa complex in brain. *Eur J Neurosci.* 27(2):284-93

Vesa, J., Sua, H., Watts, G.D., Krausec, S., Walter, M.C., Wallace, D.C. and Kimonis, V.E. (2009) Valosin containing protein associated inclusion body myopathy: abnormal vacuolization, autophagy and cell fusion in myoblasts *Neuromuscul. Disord*. 19(11): 766–72.

Waggoner, B., Kovach, M.J., Winkelman, M., Cai, D., Khardori, R., Gelber, D., Kimonis, V.E. (2002) Heterogeneity in familial dominant Paget disease of bone and muscular dystrophy. *Am. J. Med. Genet.* 108(3):187-91

Wallace, D. C. (2005) A mitochondrial paradigm of metabolic and degenerative diseases, aging, and cancer: a dawn for evolutionary medicine. *Annu. Rev. Genet.* 39: 359-407

Wang, Q., Song, C. and Chou-Chi, H. (2004) Molecular perspectives on p97–VCP: progress in understanding its structure and diverse biological functions. *Jour. Struct. Biol.* 146: 44–57

Watts, G.D., Wymer, J., Kovach, M.J., Mehta, S.G., Mumm, S., Darvish, D., Pestronk, A., Whyte, M.P. and Kimonis, V.E. (2004) Inclusion body myopathy associated with Paget disease of bone and frontotemporal dementia is caused by mutant valosin-containing protein. *Nat Genet.* 36(4): 377-81

Watts, G.D., Thomasova, D., Ramdeen, S.K., Fulchiero, E.C., Mehta, S.G., Drachman, D.A., Weihl, C.C., Jamrozik, Z., Kwiecinski, H., Kaminska, A. and Kimonis, V.E. (2007) Novel VCP mutations in inclusion body myopathy associated with Paget disease of bone and frontotemporal dementia. *Clin. Genet.* 72(5): 420-6

Weidberg, H., Shvets, E. and Elazar, Z. (2011) Biogenesis and Cargo Selectivity of Autophagosomes. *Annu. Rev. Biochem.* 80: 125–56

Weihl, C.C., Dalal, S., Pestronk, A. and Hanson, P.I. (2006) Inclusion body myopathy-associated mutations in p97/VCP impair endoplasmic reticulum-associated degradation. *Hum. Mol. Genet.* 15(2): 189-99

Weihl, C.C, Miller, S.E., Hanson, P.I. and Pestronk, A. (2007) Transgenic expression of inclusion body myopathy associated mutant p97/VCP causes weakness and ubiquitinated protein inclusions in mice. *Hum. Mol. Genet.* 16(8): 919-28

Weihl, C.C., Temiz, P., Miller, S.E., Watts, G.D., Smith, C., Forman, M., Hanson, P.I., Kimonis, V.E. and Pestronk, A. (2008) TDP-43 accumulation in inclusion body myopathy muscle suggests a common pathogenic mechanism with frontotemporal dementia. *J. Neurol. Neurosurg. Psychiatry*. 79(10): 1186–1189

Weihl, C.C., Pestronk, A. and Kimonis, V.E. (2009) Valosin-containing protein disease: inclusion body myopathy with Paget's disease of the bone and fronto-temporal dementia. *Neuromuscul. Disord.* 19(5): 308-15

Westerblad, H., Bruton, J.D. and Katz, A. (2010) Skeletal muscle: energy metabolism, fibre types, fatigue and adaptability. *Exp. Cell Res*. 316: 3093-9

Westrate, L.M., Drocco, J.A., Martin, K.R., Hlavacek, W.S. and MacKeigan, J.P. (2014) Mitochondrial morphological features are associated with fission and fusion events. *PLoS One* 9(4): e95265

Wolf, D.H. and Stolz, A. (2012) The Cdc48 machine in endoplasmic reticulum-associated protein degradation. *Biochim. Biophys. Acta*. 1823(1): 117-24

Xia, D., Tang W.K., Ye, Y. Structure and function of the AAA+ ATPASE p97/Cdc48p. *Gene.* Mar 3. pii: S0378-1119(16)30125-1

Xu, S., Peng, G., Wang, Y., Fang, S. and Karbowski, M. (2011) The AAA-ATPase p97 is essential for outer mitochondrial membrane protein turnover. *Mol. Biol. Cell* 22: 291-300

Yamanaka, K., Sasagawa, Y. and Ogura, T. (2012) Recent advances in p97/VCP/Cdc48 cellular functions. *Biochim. Biophys. Acta.* 1823(1): 130-7

Yang, J.H., Gross, R.L., Basinger, S.F. and Wu, S.M. (2001) Apoptotic cell death of cultured salamander photoreceptors induced by CCCP: CsA-insensitive mitochondrial permeability transition. *J. Cell. Sci.* 114(Pt 9): 1655-64

Ye, Y., Meyer, H.H., and Rapoport, T.A. (2001) The AAA ATPase Cdc48/p97 and its partners transport proteins from the ER into the cytosol. *Letters to Nature,* 414: 652–56

Yeung, H.O., Kloppsteck, P., Niwa, H., Isaacson, R.L., Matthews, S., Zhang, X. and Freemont, P.S. (2008) Insights into adaptor binding to the AAA protein p97. *Biochem. Soc. Trans.* 36: 62–67

Yeung, H.O., Förster, A., Bebeacua, C., Niwa, H., Ewens, C., McKeown, C., Zhang, X., Freemont, P.S. (2014) Inter-ring rotations of AAA ATPase p97 revealed by electron cryomicroscopy. *Open Biol.* 5(4): 130142

Youle, R.J., van der Bliek, A.M. (2012) Mitochondrial fission, fusion and stress. *Science* 337(6098): 1062-5